UNIVERSITÀ
DEGLI STUDI
FIRENZE

DOTTORATO DI RICERCA IN FISICA E ASTRONOMIA

CICLO XXIX

COORDINATORE Prof. Massimo Gurioli

Single particle dynamics in liquid systems

Settore Scientifico Disciplinare FIS/03

Dottorando

Dott. Bellissima Stefano

Tutore

Prof. Guarini Eleonora

Coordinatore

Prof. Gurioli Massimo

Anni 2013/2016

Alla mia famiglia

e a Marta

Contents

Chapter 1

Introduction to the work

Fluid dynamics is a very rich and fascinating research field that in the last decades has gone through considerable progresses thanks to the always increasing performance of neutron and X-ray scattering techniques and to the great developments in computing science. Here, when referring to fluid dynamics, we mean the fluid behavior at a microscopic, atomic level, where the ~ps and ~nm time and length scales, respectively, are involved.

Thermal neutrons are an ideal probe to investigate the microscopic dynamics of fluids, because their de Broglie wavelengths and their energies closely match the typical interatomic separations ($\sim$ 1 Å) and excitation energies ($\sim$ 1 meV) of such systems. X-ray photons also have the appropriate wavelengths but much larger energies, of the order of $\sim$ 1 keV, and are equally employed for such studies thanks to the high energy resolution reached by X-ray spectrometers.

Scattering experiments do not probe the dynamics of the system in the direct position-time $(\mathbf{r}, t)$ space, but rather in its reciprocal wavevector-frequency $(\mathbf{Q}, \omega)$ space, where $\hbar\mathbf{Q}$ and $\hbar\omega$ are identified, respectively, with the momentum and the energy the neutron (or the photon) exchanges with the sample. Generally speaking, a scattering experiment gives access to the so-called dynamic structure factor $S(\mathbf{Q}, \omega)$, which represents the ($\mathbf{Q}$, ω)-spectrum of the autocorrelation function of density fluctuations occurring in the system. In particular, the study of the dynamics is typically carried out by analyzing the shape of the frequency spectra $S(\mathbf{Q}, \omega)$ at fixed $\mathbf{Q}$, whose modulus Q is the only relevant parameter in fluid systems and sets the length scale under investigation.

A peculiarity of neutron scattering, which exploits the existence of an incoherent cross sec-

tion, is the possibility of measuring the *self* dynamic structure factor $S_{\text{self}}(\mathbf{Q}, \omega)$, thus focusing on the motion of a single particle rather than on the collective behavior of all particles.

The object of this PhD thesis is precisely the study of the self dynamics of various liquid systems based on simulation data-sets appositely prepared during the PhD work, except in one case (see Ch. 7). The link with neutron measurements is clarified in the last chapter of this thesis, although use is not made here of neutron data. The interest in this topic has originated from our intention to reach a better understanding of self dynamic properties by applying a substantially new method, not attempted so far, for the description of self functions, and based on a recently presented general theory of time autocorrelation functions in many-body Hamiltonian systems.

Both empirical and, more recently, ab initio molecular dynamics simulations have played a crucial role in the liquid dynamics research field. Thanks to the progresses made in computing power, simulation results are nowadays far more reliable than in the past and, moreover, they offer some advantages with respect to experimental data. First, simulations can cover extremely wide ranges of Q and ω, being not limited, as in neutron experiments, by kinematic restrictions. Second, simulations allow to directly compute the exact quantity of interest. For example, in a neutron scattering experiment on a monatomic fluid system, besides various background contributions, one measures two signals simultaneously: the first, weighted by the coherent cross section, is related to $S(Q, \omega)$ and the second, weighted by the incoherent cross section, is related to $S_{\text{self}}(Q, \omega)$. Therefore, unless the incoherent cross section is much larger than the coherent one, the extraction of the self part necessarily requires the subtraction of the coherent signal. Third, simulations give access to whatever dynamical function of interest for the system, including the ones that are difficult or impossible to obtain experimentally. For example, the velocity autocorrelation function (VAF), which can be straightforwardly calculated from a simulation, requires quite a difficult extrapolation to $Q = 0$ of $S_{\text{self}}(Q, \omega)$.

It is important to stress, however, that the use of simulated data does not alter in any way the general validity of the new results presented here, which we think would be of great help also for the interpretation of experimental data in future research.

Apart from an initial introductive part (Chs. 2 and 3), the chapters of this thesis (from Ch. 4 to Ch. 7) deal with the application of the aforementioned general theory to various cases, which differ for the type of fluid and/or the self property under investigation. In the first part of this

work we exploited the collaboration with Prof. M. Neumann (Faculty of Physics, University of Vienna) to perform very accurate molecular dynamics calculations of the VAF of a slightly supercritical Lennard-Jones fluid at various densities. Indeed, the velocity autocorrelation function is a key quantity in the atomic-scale dynamics of fluids and, moreover, has provided the first paradigmatic example of a long-time tail phenomenon, this thesis will also deal with. There is, however, much more to the VAF than simply the evidence of its long-time dynamics as clearly shown in this work (Chs. 4 and 5). Nonetheless, a unified description of this function from very short to long times, and of the way it changes with varying density, was missing until present.

In Chs. 4 and 5 we show that a very general approach based on multi-exponential expansions allows for a full account and understanding of the basic dynamical processes encompassed by the VAF. In particular, we evidenced the presence of fast and slow decay channels on the time scale set by the collision rate and, with growing density, it was possible to relate these processes to specific dynamic mechanisms occurring in the system, like the longitudinal and transverse wave propagation, that suggested the interpretation of the VAF frequency spectrum as a global density of states, generalizing to fluids a well-known solid-state concept. Moreover, the identification of a dynamical transition at an intermediate density of the LJ fluid considered clearly contributes to the recent debates about the presence of dynamical crossover boundaries in the supercritical region, like the Widom and the Frenkel line.

The interesting results that emerged from the analysis of the VAF of the LJ supercritical fluid prompted us to investigate also the VAF of a semi-quantum system in similar thermodynamic conditions, in order to explore quantum-mechanical effects on the behavior of this function. For this study, reported in Ch. 6, a more realistic system was chosen, that is para-hydrogen (p-H_2) molecules interacting via the Silvera-Goldman pair potential, and the Ring-Polymer Molecular Dynamics technique was used to carry out the quantum simulation. Again, the collaboration with Prof. M. Neumann was crucial in transferring to us the skills to perform reliable, and not at all standard, simulations of the dynamics of a non-classical fluid. This work gives evidence of the similarities between the classical LJ and the semi-quantum p-H_2 systems but, at the same time, it identifies in a clear way which are the differences and where they originate from.

To encompass all different aspects of self dynamics, we also studied the $S_{\mathrm{self}}(Q,\omega)$ of a liquid metal like gold, for which accurate ab initio simulations were available. Indeed, a combined

analysis of neutron scattering and simulation data was used in a previous work to investigate the collective dynamics of this system. In this respect, it was interesting to move further in the dynamical characterization of this liquid and to successfully exploit the mentioned multi-Lorentzian approach to better understand its self dynamics. This part of the work, reported in Ch. 7, not only has opened a possible way of interpreting the physics behind $S_{\mathrm{self}}(Q,\omega)$ spectra in a wide (Q,ω) range, but also has deepened considerably the link between $S_{\mathrm{self}}(Q,\omega)$ and the VAF spectrum $Z(\omega)$, providing, for example, an innovative procedure to perform the $Q \to 0$ extrapolation required to determine $Z(\omega)$ from $S_{\mathrm{self}}(Q,\omega)$ data. Moreover, we tried to probe the link between the collective (longitudinal and transverse) modes and the shape of $Z(\omega)$, extending to a liquid metal near the triple point the observations previously gathered in Ch. 5 for the LJ fluid. This analysis had also the merit to provide, in a natural way, a beautiful explanation of the role assumed by the hydrodynamic Fick's Lorentzian mode both in $S_{\mathrm{self}}(Q,\omega)$ and in $Z(\omega)$, and of the microscopic non-hydrodynamic mechanisms that build up the self diffusion coefficient.

Given the great potential of a novel interpretation method of self spectra, we were tempted to apply such concepts also to more complex systems as, for example, molecular liquids, and more interestingly hydrogen-bonded (HB) liquids. In water, experimental and simulation studies in fact revealed a richer dynamical behavior with respect to noble-gas or metallic liquids, and suggested a more complex picture of fluids, with longitudinal and transverse vibratory components able to mix up, each projected and visible in nominally "pure" longitudinal and transverse quantities. For long the peculiar dynamics of water has been explained in terms of the clearly most striking difference from other simple fluids: hydrogen bond. Therefore, its role, the onset of shear waves and the possible presence of other HB-driven excitations are worth deeper investigations in similar fluids. In particular, we focused on liquid methanol, for which simulations were already performed in the past, thanks to the collaboration with dr. M. González (Institute Laue-Langevin, Grenoble) and dr. F. Formisano (CNR-IOM, Grenoble), and successively exploited to carry out a detailed study of its collective dynamics. The results of the calculation of $Z(\omega)$ and $S_{\mathrm{self}}(Q,\omega)$ spectra, reported in par. 7.5, are quite intriguing and clearly display a close relation with collective propagating modes. However, an analysis similar to that proposed here for liquid gold is outside the scope of this PhD work, and left to future research.

This thesis is mainly based on the theoretical works reported in Refs. [1, 2, 3] and on the

experimental work about liquid gold of Ref. [4], and has been the object of various publications [5, 6, 7], whose contents are reported in Chs. 4, 5 and 7. Other references, specific of each topic, will be given later in the text.

Chapter 2

Theoretical background

2.1 Introduction

A detailed study of fluids dynamics at a microscopic level is intrinsically a very hard task. The reason for that becomes evident when comparing fluids to other states of matter, like crystals and dilute gases. Indeed, in the case of crystals there is a relatively simple model, the harmonic crystal, which represents a good zero-order approximation for setting up more refined theories. In the opposite case, for a gas, a good starting model for perturbative approaches is the ideal gas, where particles are supposed to be point-like and non-interacting at finite distances. In a sense, dense fluids lie perfectly in the middle between gases and crystals and, as a consequence, neither of these two extreme situations can be considered as a reference one. Despite that, in the 70's-80's many theoretical approaches have been attempted in order to give a more or less approximate description of microscopic dynamics as, for example, the generalized kinetic theory and the mode-coupling theory [8, 9]. However, the formalism is often rather complex and somewhat obscure, so that also phenomenological approaches have been largely adopted.

This thesis work deals only with fluids for which Boltzmann statistics is applicable. Actually, this is not a big restriction, since there are only few fluids that need a pure quantum treatment. For example, the two isotopes ^{3}He and ^{4}He at very low temperatures.

In the following a brief description will be given of the basic dynamical quantities characterizing monatomic Boltzmann fluids composed of N particles in equilibrium at temperature T

in a volume V. The dynamical behavior of the system is representable by means of appropriate correlation functions of microscopic variables [10] as, for example, the microscopic particle density

$$\rho(\mathbf{r}, t) = \sum_{j=1}^{N} \delta(\mathbf{r} - \mathbf{R}_j(t)) \tag{2.1}$$

which gives the probability that, at a given instant t, a given configuration of N particles, identified by vectors $\mathbf{R}_j$, is realized. In the context of the canonical ensemble, here adopted, one can immediately verify that $\langle\rho(\mathbf{r}, t)\rangle$ is equal to the macroscopic number density $\rho = N/V$ of the system. The definition (2.1) allows to introduce the well-known van Hove autocorrelation function [10]

$$G(\mathbf{r}, t) = \frac{1}{\rho}\langle\rho(\mathbf{0}, \mathbf{0})\rho(\mathbf{r}, \mathbf{t})\rangle, \tag{2.2}$$

that represents the probability of having, at time $t = 0$, a given atom somewhere in the fluid, for example in the origin ($\mathbf{r} = \mathbf{0}$), and whatever atom (also the same) at a distance $\mathbf{r}$ after a time t. In Eq. (2.2) the time invariance of averages at thermodynamic equilibrium, as well as the translational invariance (consequence of the homogeneity and the isotropy of the fluid) have been exploited. The spatial Fourier transform of Eq. (2.2)

$$F(\mathbf{Q}, t) = \int \mathrm{d}\mathbf{r}\, \mathrm{e}^{i\mathbf{Q}\cdot\mathbf{r}} G(\mathbf{r}, t) = \frac{1}{N}\langle\rho_{-\mathbf{Q}}(0)\rho_{\mathbf{Q}}(t)\rangle = \frac{1}{N}\sum_{j,j'=1}^{N}\langle \mathrm{e}^{-i\mathbf{Q}\cdot\mathbf{R}_j(0)}\mathrm{e}^{i\mathbf{Q}\cdot\mathbf{R}_{j'}(t)}\rangle \tag{2.3}$$

is called intermediate scattering function and represents the time correlation of the Fourier components of wave vector $\mathbf{Q}$, $\rho_{\mathbf{Q}}(t) = \sum_j e^{i\mathbf{Q}\cdot\mathbf{R}_j(t)}$, of the microscopic density (2.1). Its frequency spectrum

$$S(\mathbf{Q}, \omega) = \frac{1}{2\pi}\int \mathrm{d}t\, \mathrm{e}^{-i\omega t}\frac{1}{N}\sum_{j,j'=1}^{N}\langle e^{-i\mathbf{Q}\cdot\mathbf{R}_j(0)} e^{i\mathbf{Q}\cdot\mathbf{R}_{j'}(t)}\rangle \tag{2.4}$$

is called *dynamic structure factor*. In a homogeneous and isotropic fluid the dependence of (2.3) and (2.4) on wave vector $\mathbf{Q}$ is only through its modulus Q. Eq. (2.4) defines a quantity of fundamental interest in fluid dynamics and it is the main objective of inelastic neutron (or radiation) scattering experiments.

It is useful to extract from (2.4) the two contributions that come from the correlations of couples with $j' \neq j$ (*distinct*, $S_{\mathrm{dist}}(Q, \omega)$) and with $j' = j$ (*self*, $S_{\mathrm{self}}(Q, \omega)$), so that

$$S(Q, \omega) = S_{\mathrm{dist}}(Q, \omega) + S_{\mathrm{self}}(Q, \omega). \tag{2.5}$$

While the *distinct* part is crucial for the study of the collective dynamics of atoms, the *self* one provides information about the single-particle dynamics. Although only numerical simulation data will be presented in this work, it is important to remind that the *self* dynamics can be accessed experimentally through inelastic incoherent neutron scattering. Incoherence is a unique property of neutron scattering that arises both from the fluctuations of the scattering cross section induced by the two different relative orientations of the neutron and nucleus spins, and from the isotopic composition of the sample.

In the framework of quantum mechanics, the position $\mathbf{R}(t)$ and momentum $\mathbf{p}(t)$ vectors are operators which do not commute. As a consequence, also the vectors $\mathbf{R}_j(t)$ and $\mathbf{R}_j(0)$ do not commute. For this reason, the correlation function (2.3) is a complex quantity and its spectrum (2.4) is real but not symmetric with respect to ω [11]. In particular, $S(Q,\omega)$ can be put in the form

$$S(Q,\omega) = \frac{\hbar\omega\beta}{[1-\exp(-\hbar\omega\beta)]} R(Q,\omega), \tag{2.6}$$

where $\beta = 1/k_B T$ and $R(Q,\omega)$ is the spectrum of the so-called relaxation function [11], which has the property of being a symmetric function of ω. Moreover, it is straightforward to demonstrate that Eq. (2.6) fulfils the detailed-balance relation $S(Q,\omega) = \exp(\hbar\omega\beta) S(Q,-\omega)$.

Hereafter we'll refer only to classical fluids. So, taking the limit $\hbar \to 0$ in Eq. (2.6) yields

$$S(Q,\omega) \to R(Q,\omega), \tag{2.7}$$

i.e. the dynamic structure factor in the classical limit is a symmetric function of ω. As a consequence, it can be shown that the corresponding time autocorrelation function is also real and symmetric [11, 9].

2.2 Basic properties of self functions

Eq. (2.3) shows that the classical expression of the self intermediate scattering function is:

$$F_{\text{self}}(Q,t) = \langle \mathrm{e}^{i\mathbf{Q}\cdot(\mathbf{R}_j(t)-\mathbf{R}_j(0))} \rangle. \tag{2.8}$$

At sufficiently short times it may be Taylor expanded to give

$$F_{\text{self}}(Q,t) = 1 - \langle\omega^2\rangle_s \left(\frac{t^2}{2}\right) + \langle\omega^4\rangle_s \left(\frac{t^4}{4!}\right) + \cdots, \tag{2.9}$$

where the quantities $\langle\omega^n\rangle_s$, defined as the n-th frequency moments of the spectrum $S_{\text{self}}(Q,\omega)$

$$\langle\omega^n\rangle_s = \int_{-\infty}^{+\infty} \mathrm{d}\omega\, \omega^n S_{\text{self}}(Q,\omega), \tag{2.10}$$

are linked to the n-th order time derivatives of $F_{\text{self}}(Q,t)$ in $t = 0$ through the relation:

$$\left(\frac{\mathrm{d}^n F_{\text{self}}(Q,t)}{\mathrm{d}t^n}\right)_{t=0} = i^n\langle\omega^n\rangle \tag{2.11}$$

Obviously, the even character of $F_{\text{self}}(Q,t)$ implies that all odd frequency moments are zero. The expression of the second and fourth moments are [9]:

$$\langle\omega^2\rangle_s = \frac{k_B T}{M} Q^2 \tag{2.12}$$

$$\langle\omega^4\rangle_s = \langle\omega^2\rangle_s \left(3\langle\omega^2\rangle_s + \Omega_0^2\right), \tag{2.13}$$

where Ω_0 is the so-called Einstein frequency given by

$$\Omega_0^2 = \frac{\rho}{3M} \int \mathrm{d}\mathbf{r}\, \nabla^2\phi(r) g(r), \tag{2.14}$$

with $\phi(r)$ the pair potential and $g(r)$ the radial pair distribution function, which gives the deviation from the ideal gas case of the mean fraction of particles at a distance r from a given particle.

Exact expressions of the intermediate scattering function are achievable only in two opposite limits: the free-particle limit (kinetic regime) and the continuous medium one (hydrodynamic regime). Indicating with l and τ, respectively, the mean free path and the mean time between collisions of the particles in the fluid, the kinetic regime corresponds to the conditions $Ql \gg 1$ and $t/\tau \ll 1$, while the hydrodynamic regime to the conditions $Ql \ll 1$ and $t/\tau \gg 1$. In the first case the dynamics is probed over time and space scales such that particles appear as free ($\phi(r) = 0$). In the second case, the scales of observation of the dynamics are such that the system is seen as a continuum. The expressions of $F_{\text{self}}(Q,t)$ and of $S_{\text{self}}(Q,\omega)$ in these limits read [9]:

$$F_{\text{self}}(Q,t) = \exp\left(-\frac{Q^2t^2}{2M\beta}\right) \rightarrow S_{\text{self}}(Q,\omega) = \sqrt{\frac{M\beta}{2\pi Q^2}}\, \exp\left(-\frac{\beta M\omega^2}{2Q^2}\right) \qquad \text{ideal gas} \tag{2.15}$$

$$F_{\text{self}}(Q,t) = \exp\left(-D_s Q^2|t|\right) \rightarrow S_{\text{self}}(Q,\omega) = \frac{1}{\pi}\frac{D_s Q^2}{\omega^2 + (D_s Q^2)^2} \qquad \text{simple diffusion}$$

where D_s is the self (mass) diffusion coefficient. The shape of the spectrum passes from a Gaussian to a Lorentzian function of ω but, in both cases, $F_{\rm self}(Q,t)$ has a Gaussian behavior with respect to the variable Q.

From the definition (2.8) and exploiting the isotropy of the system, the following relation can be derived:

$$\lim_{Q\to 0}\left[-\frac{1}{Q^2}\left(\frac{\mathrm{d}^2 F_{\rm self}(Q,t)}{\mathrm{d}t^2}\right)\right] = \frac{1}{3}\langle \mathbf{v}(0)\cdot\mathbf{v}(t)\rangle, \tag{2.16}$$

which relates the velocity autocorrelation function (VAF), a key quantity for the study of self dynamics, with the time derivatives of $F_{\rm self}(Q,t)$. A Fourier transform of Eq. (2.16) yields an equivalent equation for the spectra:

$$\lim_{Q\to 0}\left[3\frac{\omega^2}{Q^2}S_{\rm self}(Q,\omega)\right] = \frac{1}{2\pi}\int_{-\infty}^{\infty}\mathrm{d}t\,\mathrm{e}^{-i\omega t}\langle \mathbf{v}(0)\cdot\mathbf{v}(t)\rangle. \tag{2.17}$$

Starting from Eq. (2.9) and using Eq. (2.16), one also obtains the power series of the VAF for short times [8]:

$$\langle \mathbf{v}_j(0)\cdot\mathbf{v}_j(t)\rangle = \langle \mathbf{v}^2\rangle - \langle \mathbf{v}^2\rangle\Omega_0^2\left(\frac{t^2}{2}\right) + \cdots . \tag{2.18}$$

Introducing the normalized VAF, the previous equation reads:

$$Z(t) \equiv \frac{\langle \mathbf{v}_j(0)\cdot\mathbf{v}_j(t)\rangle}{\langle \mathbf{v}^2\rangle} = 1 - \Omega_0^2\left(\frac{t^2}{2}\right) + \cdots . \tag{2.19}$$

Another important dynamical quantity is the mean square displacement of a particle $\langle r^2(t)\rangle = \langle(\mathbf{r}_j(0)-\mathbf{r}_j(t))^2\rangle$, which is related to the VAF through the relation [8]

$$\langle r^2(t)\rangle = \int_0^t \mathrm{d}t'\,(t-t')\,\langle \mathbf{v}_j(0)\cdot\mathbf{v}_j(t')\rangle. \tag{2.20}$$

The insertion of Eq. (2.19) in the latter expression yields the short-time behavior of $\langle r^2(t)\rangle$:

$$\langle r^2(t)\rangle = \langle \mathbf{v}^2\rangle t^2 - \frac{1}{12}\langle \mathbf{v}^2\rangle\Omega_0^2 t^4, \tag{2.21}$$

which shows that, initially, $\langle r^2(t)\rangle$ grows quadratically with time, as if the particle was free. Nevertheless, after a time of the order of Ω_0^{-1}, the particle experiences some collisions and its motion is drastically modified, with the result that $\langle r^2(t)\rangle$ reduces its grow. In the opposite limit, $t\to\infty$, Eq. (2.20) shows that $\langle r^2(t)\rangle$ increases linearly with time according to the law

$$\langle r^2(t)\rangle = 6D_s t, \tag{2.22}$$

where the self diffusion coefficient D_s is written as

$$D_s = \frac{1}{3}\int_0^\infty \mathrm{d}t\, \langle \mathbf{v}_j(0)\cdot\mathbf{v}_j(t)\rangle. \tag{2.23}$$

Eq. (2.23) is among the most important examples of Green-Kubo relations which express transport coefficients in terms of time integrals of opportune correlation functions of microscopic variables [10]. Indicating with $\hat{Z}(\omega)$ the Fourier transform of $Z(t)$ and observing that $\int_{-\infty}^{+\infty} \mathrm{d}t\, Z(t) = 2\pi\hat{Z}(0)$, Eq. (2.23) can be put in the alternative form

$$D_s = \frac{\pi}{3}\langle \mathbf{v}^2\rangle \hat{Z}(0). \tag{2.24}$$

Simple analytic expressions of the VAF are known only for few model systems such as a dilute gas of hard spheres, a Brownian particle and a harmonic crystal. As recalled in par. 2.1, none of these situations is actually representative of the behavior of a real fluid; nevertheless they suggest useful guidelines to develop more refined and realistic models.

For a harmonic crystal in the classical limit it can be shown that:

$$Z(t) = \frac{1}{N}\sum_{Q,p} \mathrm{e}^{i\omega_{Qp}t}, \tag{2.25}$$

where ω_{Qp} is the frequency of a phonon of wave vector Q and polarisation index p. As a consequence, the spectrum has the form

$$\hat{Z}(\omega) = \frac{1}{N}\sum_{Q,p} \delta(\omega - \omega_{Qp}), \tag{2.26}$$

that corresponds to the definition of the vibrational density of states (v-DoS). In the $\omega \to 0$ limit, the latter quantity is proportional to ω^2 [12] so that, exploiting Eq. (2.24), it results that a harmonic crystal has a vanishing diffusion coefficient.

Both for a dilute gas of hard spheres characterized by binary, and mutually uncorrelated, collisions (Enskog model) and for a system of Brownian particles in the Langevin description, the VAF is described by a simple exponential decay:

$$Z(t) = \mathrm{e}^{-\gamma|t|}, \tag{2.27}$$

where γ depends on the collision rate and is related to the diffusion coefficient through $D_s = k_B T/M\gamma$. The corresponding spectrum is a Lorentzian function:

$$\hat{Z}(\omega) = \frac{1}{\pi}\frac{\gamma}{\omega^2+\gamma^2}. \tag{2.28}$$

2.3 Models of $Z(t)$ and $F_{\mathrm{self}}(Q,t)$ for the liquid state

The previous paragraph has been devoted to a discussion of the fundamental properties of the two correlation functions predominantly used for the study of self dynamics: the intermediate scattering function, $F_{\mathrm{self}}(Q,t)$, and the normalized VAF, $Z(t)$. Furthermore, we gave explicit expressions of the forms that these functions assume in certain limit conditions, the only ones for which simple and intuitive models can be derived. Unfortunately, the liquid state is much more complex and, in a sense, it is actually defined by the deviations from such limits. Since the 70's, researchers have tried to find models able to describe, with sufficient accuracy, the behavior of liquids in the intermediate situations: the range of medium-high density as regards the $Z(t)$, and the region of $Ql \approx 1$ as regards the $F_{\mathrm{self}}(Q,t)$. A definitive picture has not been achieved yet and this demonstrates that even such simply-defined self functions have properties that are far from being easy to interpret. What has been certainly understood are the qualitative trends of these functions, and some features of the physical processes beneath [8]. However, from the quantitative point of view, there is still much work to be done.

A general theoretical framework that has enabled the development of a great quantity of models for the self dynamics is the one based on the memory function approach, which is extensively illustrated in the next paragraph. However, there are also models that do not belong to such a framework. As regards the $F_{\mathrm{self}}(Q,t)$, two examples are: the jump diffusion model [13] and the Egelstaff-Schofield model [14]. The first one is characterized by the idea that a particle in the fluid diffuses making jumps between "cages" that are temporary formed by the nearest neighbours of the particle itself; the corresponding spectrum is a Lorentzian function with a half-width at half-maximum given by $\Delta\omega = D_s Q^2/(1 + D_s Q^2 \tau_0)$, where τ_0 is the mean residence time in the cage. The second one makes use of the Gaussian approximation[1] [15] to relate the $F_{\mathrm{self}}(Q,t)$ to an expression of the mean square displacement $\langle r^2(t)\rangle$ that interpolates between the two limiting behaviors (2.21) and (2.22). In particular, $\langle r^2(t)\rangle = D_s(\sqrt{t^2+\tau^2} - \tau)$, where τ is an estimate of the time necessary for the particle to pass from a free ($\langle r^2(t)\rangle \propto t^2$) to a diffusive ($\langle r^2(t)\rangle \propto t$) regime.

[1] From Eqs. (2.21) and (2.22) it results that, in the ideal-gas and diffusive limits (Eqs. (2.15)), the $F_{\mathrm{self}}(Q,t)$ can be written as: $F_{\mathrm{self}}(Q,t) = \mathrm{e}^{-\frac{1}{6}Q^2\langle r^2(t)\rangle}$. The generalization of this equation to any Q value defines the so-called Gaussian approximation.

2.3.1 Memory functions

The memory-function theory, initially introduced by Zwanzig and Mori [16, 17, 18], exploits the projection operators formalism to describe general properties of many-body Hamiltonian systems. Calling $A(t)$ a dynamical variable of a system, the theory states that the equation of motion of A follows a *Generalized Langevin Equation* of the form

$$\frac{\mathrm{d}A(t)}{\mathrm{d}t} = -\int_0^t \mathrm{d}t'\, M^{(1)}(t')A(t-t') + f(t), \tag{2.29}$$

where $f(t)$ and $M^{(1)}(t)$ are, respectively, the fluctuating force, in analogy to the Langevin equation of Brownian motion, and the first-order *memory function*. Indicating with $C(t)$ the autocorrelation function of the variable A, it is possible to derive from Eq. (2.29) the equation of motion of $C(t)$, making use of the orthogonality relation between $f(t)$ and $A(t)$ ($\langle f(0)A(t)\rangle = 0$). The result is the *Memory Equation*:

$$\frac{\mathrm{d}C(t)}{\mathrm{d}t} = -\int_0^t \mathrm{d}t'\, M^{(1)}(t')C(t-t'). \tag{2.30}$$

It is important to stress that Eqs. (2.29) and (2.30) are exact, and so completely equivalent to the original Liouville equation for the variable A. The problem has been only reformulated switching the attention to the new function $M^{(1)}(t)$. The success of such reformulation lies in the fact that simple and physically intuitive models of the memory function have proved capable to catch the principal aspects of the dynamics decribed by $C(t)$.

In a subsequent work [19], Mori showed that is possible to write a relation analogous to Eq. (2.29) but for the memory function itself, introducing a second order memory function $M^{(2)}(t)$. Iterating this procedure to higher orders one obtains the following hierarchy of equations, with $j > 1$:

$$\frac{\mathrm{d}M^{(j)}(t)}{\mathrm{d}t} = -\int_0^t \mathrm{d}t'\, M^{(j+1)}(t')M^{(j)}(t-t'). \tag{2.31}$$

Equation (2.30) is solved through a Laplace transformation and making use of the convolution theorem. The result is

$$\frac{\tilde{C}(z)}{C(0)} = \frac{1}{z + \tilde{M}^{(1)}(z)}, \tag{2.32}$$

where $\tilde{C}(z)$ and $\tilde{M}^{(1)}(z)$ are, respectively, the Laplace transforms of $C(t)$ and $M^{(1)}(t)$. Repeating the same operations for Eq. (2.31) and then inserting the result into Eq. (2.32), a representation

of $\tilde{C}(z)$ as a continued fraction is achieved:

$$\frac{\tilde{C}(z)}{C(0)} = \frac{1}{z + \tilde{M}^{(1)}(z)} = \cfrac{1}{z + \cfrac{M^{(1)}(0)}{z + \tilde{M}^{(2)}(z)}} = \cfrac{1}{z + \cfrac{M^{(1)}(0)}{z + \cfrac{M^{(2)}(0)}{z + \tilde{M}^{(3)}(z)}}} = \cdots \tag{2.33}$$

The spectrum $\hat{C}(\omega)$ is then obtained through the relation

$$\frac{\hat{C}(\omega)}{C(0)} = \frac{1}{\pi}\mathrm{Re}\frac{\tilde{C}(z = i\omega)}{C(0)}. \tag{2.34}$$

Moreover, the theory yields explicit expressions for the quantities $M^{(j)}(0)$ in terms of the frequency moments of the normalized spectrum [9]:

$$M^{(1)}(0) = \langle\omega^2\rangle \tag{2.35}$$

$$M^{(2)}(0) = \frac{\langle\omega^4\rangle}{\langle\omega^2\rangle} - \langle\omega^2\rangle \tag{2.36}$$

$$M^{(3)}(0) = \frac{1}{M^{(2)}(0)}\left[\frac{\langle\omega^6\rangle}{\langle\omega^2\rangle} - \left(\frac{\langle\omega^4\rangle}{\langle\omega^2\rangle}\right)^2\right] \tag{2.37}$$

$$\cdots$$

Most of the functionalities that have been proposed for $Z(t)$ and $F_{\mathrm{self}}(Q,t)$ correspond to assuming a model for the first or second order memory function to be inserted into Eq. (2.33). Clearly it is a heuristic approach, where physical intuition plays a fundamental role. The reason of the success of this method is to be traced in its capability of describing a large variety of different dynamical situations despite the use of simple expressions for the memory function [8].

While the mathematical context these memory functions belong to is very clear, their physical meaning becomes more and more obscure with increasing j. Nevertheless, some physical insight on the concept of memory function can be obtained with the following example where it is supposed that the correlation under consideration is $Z(t)$. Indeed, taking $\tilde{M}_v^{(1)}(z)$ as a constant in Eq. (2.32), i.e. performing the Markovian hypothesis $M_v^{(1)}(t) \propto \delta(t)$, the resulting $Z(t)$ is an exponential decay as in Eq. (2.27), which is valid in the limit of a diluite gas characterized by binary and mutually uncorrelated collisions. Therefore, the assumption $M_v^{(1)}(t) \propto \delta(t)$ corresponds to have an instantaneous loss of memory between subsequent collisions in the system.

Consequently, taking a function $M_v^{(1)}(t)$ that has a slower (not instantaneous) decay, is equivalent to assume that the dynamics of the particles at a certain instant maintains some "memory" of the collisions occurred at previous times.

Among the vastness of models present in the literature [8] for $Z(t)$, it is possible to identify two main categories: models in which $M_v^{(1)}(t)$ is ruled by a single relaxation term (typical forms are the exponential [20, 21] and the Gaussian [22] functions) and models where two processes, having different characteristic times, are hypothesized (an example is the Levesque and Verlet model [9, 23]). The latter typology of models have proved superior in reproducing the behavior of the VAF and has found a formal justification in the context of the *Mode Coupling* (MC) and the *Generalized Kinetic* (GK) theories, according to which the memory function is composed of two terms: a fast decay that describes the effect of binary collisions and a slower one that takes into account the effect of many-body correlated collisions [9] consequence of the coupling with collective modes in the system.

Like for the VAF, the memory function approach has been widely employed also for the intermediate scattering function $F_{\text{self}}(Q,t)$. In this case a good starting point for the discussion is the following continued fraction representation:

$$\tilde{F}_s(Q,z) = \frac{1}{z + \tilde{M}_s^{(1)}(Q,z)} = \cfrac{1}{z + \cfrac{\langle\omega^2\rangle_s}{z + \tilde{M}_s^{(2)}(Q,z)}}. \tag{2.38}$$

It can be demonstrated [9] that, for vanishing wave vectors Q, the quantity $M_s^{(1)}(Q,t)/Q^2$ tends to the VAF and so, correspondingly, $M_s^{(2)}(Q,t)$ tends to the first order memory function $M_v^{(1)}(t)$ of the VAF. Based on this relation, the two categories of models previously introduced for $Z(t)$ are also applicable to the case of $F_{\text{self}}(Q,t)$ in the limit $Q \to 0$, but with reference to the second order memory function. Among the single relaxation time models, an example is the one of Lovesey, characterized by $M_s^{(2)}(Q,t)$ of exponential shape; among the other models the one of Wahnström and Sjögren [24], derived in the context of MC and GK theories, can be mentioned. The physical picture that emerges from the latter models can be summarized as follows. For small wave vectors the particle is seen to perform an essentially diffusive motion during which, however, the formation of cages, that trap the particle for a certain time, is the evidence of a coupling with collective density fluctuations. For wave vectors large enough to

prevent the observation of such cages the situation changes drastically and the dynamics appears to be determined by binary and mutually uncorrelated collisions. For even larger wave vectors not even the collisions are observable, and so the dynamics approaches that of a system of non-interacting particles (ideal gas). It is worth to be noticed that, typically, the comparison between models and experimental (or simulated) data does not concern the detailed shape of $S_{\text{self}}(Q,\omega)$ spectra, but rather the behavior of two functions, $\Gamma_s(Q)/D_sQ^2$ and $\pi D_sQ^2S_s(Q,0)$, that represent the deviation from the $Q \to 0$ limit of the half width at half maximum of the spectrum and the peak height respectively. Even though not fully satisfactory, this choice is justified by the fact that $S_{\text{self}}(Q,\omega)$ spectra exhibit a smooth and monotonous trend so that it is reasonable to expect that the relevant physical information is contained in the evolution with Q of their width and height. Nevertheless, we'll illustrate in this work (see Ch. 7) that it is possible to go further and to avoid such a rough approach in favor of a well founded one, that is based on concepts that are the object of the following section.

2.4 Exponential series theory

Until very recently, the study of the dynamical behavior of many-body Hamiltonian systems mainly occurred in the framework of the generalized Langevin equation introduced by Mori and Zwanzig, as previously summarized. Indeed, many theoretical works dealt with the search for expressions of the memory function that were able to reproduce the characteristics of measured and simulated spectra. An alternative theory to that of Mori and Zwanzig has been proposed in recent works of Barocchi et al. [1, 2, 3] where, starting from the Lee approach [25, 26, 27] to account for many-body dynamics, it is demonstrated that every autocorrelation function $C(t)$ of microscopic variables of a system at thermodynamic equilibrium has an exact expression in the form of a series of exponential functions.

Indeed, albeit following a different method that does not refer to the concepts of memory functions and fluctuating forces, even in this case the solution of the Langevin equation is put

in the form of a continued fraction

$$\tilde{C}(z) = \cfrac{1}{z + \cfrac{\Delta_1}{z + \cfrac{\Delta_2}{z + \cfrac{\Delta_3}{z + \cdots}}}}, \tag{2.39}$$

but an additional substantial step is carried out, that consists in rewriting the fraction as

$$\tilde{C}(z) = \sum_{j=1}^{\infty} \frac{I_j}{z - z_j}, \tag{2.40}$$

where I_j and z_j acquire the meaning, respectively, of amplitudes and eigenfrequencies of the normal modes representation (2.40) of the spectra of the correlation $C(t)$. The time analogous of Eq. (2.40) is a series of exponential functions:

$$C(t) = \sum_{j=1}^{\infty} I_j \mathrm{e}^{z_j |t|}, \tag{2.41}$$

where each term of the series is associated to a particular relaxation channel of the system. If I_j and z_j are complex quantities then the corresponding mode and its complex conjugate are both present in the series and, taken together, describe an exponentially damped oscillation. If I_j and z_j are instead real then they define a pure exponential decay. In all cases, however, the real part of z_j is negative so that the correlation $C(t)$ decays to zero in the limit $t \to \infty$.

Moving to spectra through Eq. (2.34), it is straightforward to see that real I_j and z_j give Lorentzians centered at $\omega = 0$:

$$\frac{1}{\pi}\mathrm{Re}\left[\frac{I_j}{i\omega - z_j}\right] = I_j \cdot \frac{1}{\pi}\frac{-z_j}{\omega^2 + z_j^2}, \tag{2.42}$$

while complex $I_j = I_j^{'} + i\, I_j^{''}$ and $z_j = z_j^{'} + i\, z_j^{''}$ result in distorted Lorentzians centered at $\pm z_j^{''}$:

$$\frac{1}{\pi}\mathrm{Re}\left[\frac{I_j}{i\omega - z_j} + \frac{I_j^*}{i\omega - z_j^*}\right] = \tag{2.43}$$

$$= \frac{1}{\pi}\left[I_j^{'} \cdot \frac{-z_j + I_j^{''}/I_j^{'}(\omega - z_j^{''})}{(\omega - z_j^{''})^2 + z_j^2} + I_j^{'} \cdot \frac{-z_j - I_j^{''}/I_j^{'}(\omega + z_j^{''})}{(\omega + z_j^{''})^2 + z_j^2}\right]$$

As well known, the properties of $C(t)$ in the origin are directly linked to the frequency moments of the spectrum $\hat{C}(\omega)$:

$$\left(\frac{\mathrm{d}^k C(t)}{\mathrm{d}t^k}\right)_{t=0} = i^k \langle \omega^k \rangle \equiv i^k \int_{-\infty}^{\infty} \mathrm{d}\omega\, \omega^k\, \hat{C}(\omega). \tag{2.44}$$

Since in a classical system of particles interacting via a continuous potential, every correlation function is even in time and infinitely differentiable in $t = 0$, Eq. (2.44) implies that $\langle \omega^k \rangle$ is zero for odd k and has a finite value for even k. As a consequence, the parameters I_j and z_j of the mode expansion are not independent. Indeed, inserting the exponential series (2.41) in Eq. (2.44), one obtains a set of sum rules, for $k \geq 0$, of the form

$$\sum_{j=1}^{\infty} I_j z_j^k = i^k \langle \omega^k \rangle. \tag{2.45}$$

In practical cases, Eq. (2.41) is applied as a fit model to the $C(t)$ data by truncating the series at a certain level, which depends both on the extension and accuracy of the available data and on the need to avoid an overparametrization of the fit model. After the truncation, Eqs. (2.44) and (2.45) are no longer valid for any value of k but only up to a specific k_m that depends both on the level of the approximation and on the model assumed [1, 5]. Moreover, in Ref. [28] it is shown that imposing a sum rule $\sum_j I_j z_j^k = 0$ with odd k is equivalent to guarantee the finiteness of the spectral moment $\langle \omega^{k+1} \rangle$.

Given its generality, this method of analysis based on exponential expansions has been adopted in this thesis to describe self correlation functions of various systems, and for this purpose a specific fit routine has been implemented via the Matlab platform.

Chapter 3

Basic principles of MD simulations of a fluid

The molecular dynamics (MD) simulation is a method that allows to compute equilibrium and transport properties of a classical many-body system. The term classic means that the motion of all nuclei of the N atoms that compose the system obeys classical mechanics laws. The basic principle is quite simple: a trajectory is generated in the phase space of the chosen system by solving the Newton equations of motions. More in detail, the simulation can be divided into two stages: an equilibration part in which the mean properties of the system drift until thermodynamic equilibrium is reached, and a production part that represents the actual "measurement" of the system.

Denoting by $\{\mathbf{r}_j\}$ and $\{\mathbf{p}_j\}$ the set of coordinates and momenta of the identical N particles (each of mass m) and using the pair-potential approximation, the Hamiltonian of the system can be written as

$$H(\{\mathbf{r}_j\},\{\mathbf{p}_j\}) = K(\{\mathbf{p}_j\}) + U(\{\mathbf{r}_j\}) = \sum_{j=1} \frac{\mathbf{p}_j^{\,2}}{2m} + \sum_{i<j} U(r_{ij}), \tag{3.1}$$

i.e. the sum of kinetic and potential terms, where r_{ij} indicates the distance between particles i and j. Inserting the last expression in the Hamilton equations, one extracts the Newton equations of motion for each particle:

$$m\frac{\mathrm{d}^2\mathbf{r}_i}{\mathrm{d}t^2} = -\sum_{j\neq i} \nabla_{\mathbf{r}_j} U(r_{ij}) = \sum_{j\neq i} \mathbf{f}(r_{ji}), \tag{3.2}$$

where $\mathbf{f}(r_{ji})$ is defined as in Fig. 3.1. For the purposes of investigating general properties of

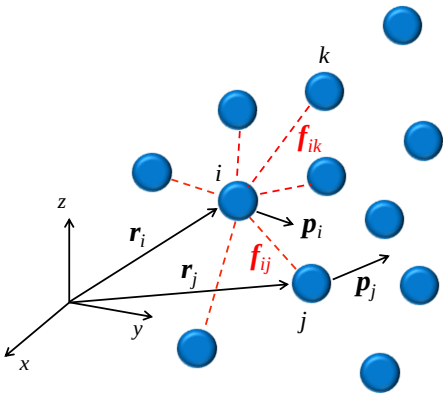

Figure 3.1: Schematic picture of a system of N interacting particles. The particle i is identified by a position vector $\mathbf{r}_i$, has a momentum $\mathbf{p}_i$ and exerts a force $\mathbf{f}_{ij}$ on particle j.

liquids and for comparison with theories, a simple Lennard-Jones 12-6 pair potential is often employed:

$$U^{LJ}(r) = 4\epsilon\left[\left(\frac{\sigma}{r}\right)^{12} - \left(\frac{\sigma}{r}\right)^{6}\right] \tag{3.3}$$

It is composed of a long-range tail of the form $-1/r^6$, a negative well of depth ϵ, and a steeply rising repulsive barrier which becomes positive for $r < \sigma$.

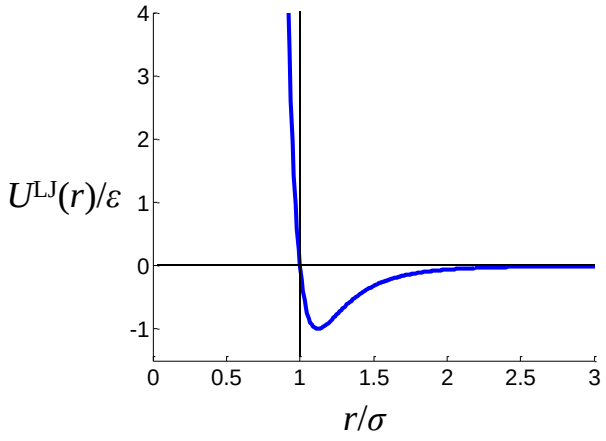

Figure 3.2: Lennard-Jones 12-6 pair potential.

To perform a MD simulation it is convenient to work with dimensionless quantities. There are several reasons for doing this: i) properties that are measured in reduced units can easily be scaled to the appropriate physical units for each problem of interest, ii) the equations of motion can be written in a simplified and concise way, iii) it is possible to work with numerical values

that are not too distant from unity. In the case of a LJ potential the reduction is made by choosing σ, m and ϵ as the units of length, mass and energy. For example, the reduced time is given by $t^* = t/\sqrt{m\sigma^2/\epsilon}$ and the reduced temperature by $T^* = k_B T/\epsilon$. Inserting the LJ potential (3.3) into the Newton equation (3.2), and using reduced units, one arrives at the following relation:

$$\frac{\mathrm{d}^2\mathbf{r}_i^*}{\mathrm{d}t^{*2}} = \sum_{j\neq i} 24\left[2\left(\frac{1}{r_{ij}^*}\right)^{14} - \left(\frac{1}{r_{ij}^*}\right)^{8}\right]\mathbf{r}_{ij}^* \tag{3.4}$$

In practice the force on particle j is calculated from the force on i by exploiting Newton's third law, and so each pair need only be examined once. Moreover, the interaction is typically cut off at some upper limit separation r_c so that $\mathbf{f}(r_{ij}) = 0$ if $r_{ij} > r_c$.

In order to simulate properties of the bulk liquid, one of the major obstacles is the large fraction of molecules which lie on the surface of the simulation box. This problem is usually overcome by implementing Born-von Karman periodic boundary conditions, which amount to consider an infinite space-filling lattice of identical copies of the simulation region. This periodicity has two consequences: i) a particle leaving the original box through a particular bounding face immediately reenters the box through the opposite face; ii) particles lying within a distance r_c of a boundary interact with particles in an adjacent copy of the system. Periodic boundaries have also to be considered when analyzing the results of the simulation because they can lead to spurious effects. One example is the fact that disturbances generated inside the box, if not sufficiently attenuated, can propagate within the system and, through the wraparound effect, return to affect the particles at a later time.

To start the simulation, positions and velocities of all particles have to be assigned. To do that, it is often preferred to start from a lattice configuration spaced to give the desired density. A common choice is that of a face-centered cubic structure. The initial velocities are typically assigned random directions and a fixed magnitude based on temperature, through the relation $\langle \frac{1}{2} m\mathbf{v}_i^2 \rangle = \frac{3}{2} k_B T$. Velocities are also constrained so that there is no overall momentum that shifts the system.

After the start-up process, a first run of the simulation is necessary to lose memory of the initial configuration and so reach the equilibrium at the desired fluid state. A way to monitor the progress to equilibrium is that of recording the trend of the instantaneous values of some thermodynamic functions, as the potential energy and the pressure. The latter, in particular, can

be calculated exploiting the virial theorem that reads:

$$P = \frac{Nk_BT}{V} + \frac{1}{3V}\left\langle \sum_{j>i} \mathbf{r}_{ij} \cdot \mathbf{f}(r_{ij}) \right\rangle . \tag{3.5}$$

The equilibration should proceed at least until these quantities stop showing a systematic drift and start to oscillate around mean values. Instead of recording instantaneous values, an alternative and wiser method could be that of dividing the simulation into small subruns and record the mean values of the functions calculated in each sunbrun. Moreover, when the fluid to simulate is at quite low temperatures it is better to start the equilibration at a higher temperature and later decrease it until the desired one is reached.

The core of a MD simulation, as well as its most time-consuming part, is the calculation of forces which requires a double loop on particles to examine only pairs that are separated by less than r_c. There are some techniques that make this calculation more efficient, in such a way that computing time passes from a N^2 scaling to a N scaling. Two examples are the cell subdivision and the tabulation of forces. The first technique consists in dividing the simulation region into a lattice of small cells whose edges all exceed r_c in length, so that interactions are only possible between particles in the same, or in adjacent, cells. Taking a list of the particles present in each cell at any time then the computation of interaction is a rapid process, which avoids the unneeded examination of all pairs in the box. The second technique is an alternative to the direct runtime evaluation of forces that takes advantage of a lookup table constructed once, at the beginning of the simulation. This method is particularly useful when the potential is a rather complicated function and includes, for example, exponentials.

Once the forces between particles are computed, Newton equations of motion must be integrated with a proper numerical algorithm. It would be desirable to have an algorithm that accurately predicts the trajectory of all particles for both short and long times. In fact, no such algorithm exists. The Lyapunov instability is such that any integration error, no matter how small, causes the simulated trajectory to diverge exponentially from the true one. However, the calculation of time correlation functions requires an essentially exact solution of the equation of motions only for times comparable to the correlation time. Moreover, the method is used just to generate trajectories from which to take microscopic states that are representative of the microcanonical ensemble of the system.

Of fundamental importance in an MD algorithm is the energy conservation over long times, a requirement that is linked to the properties of time reversibility and phase space area-preserving (symplecticity) that characterize Hamilton equations. The class of algorithms that satisfy this condition includes the leapfrog and Verlet methods. For the LJ simulations of this thesis it has been used a two-step form of the leapfrog algorithm, whose integration formula reads:

$$\begin{aligned} v(t + \mathrm{d}t/2) &= v(t) + \frac{\mathrm{d}t}{2m} f(t) \\ x(t + \mathrm{d}t) &= x(t) + \mathrm{d}t\, v(t + \mathrm{d}t/2) \\ v(t + \mathrm{d}t) &= v(t + \mathrm{d}t/2) + \frac{\mathrm{d}t}{2m} f(t + \mathrm{d}t) \end{aligned} \tag{3.6}$$

where x, v and f refer to each component respectively of position, velocity and force vectors, and $\mathrm{d}t$ is the integration step. Despite its low order, this algorithm has the merit to be extremely simple on one hand and to guarantee excellent energy conservation on the other.

As already noted, simply integrating Newton equations of motion generates a microcanonical NVE ensemble as a consequence of the conservation of the total Hamiltonian. By contrast, in a canonical NVT ensemble, energy is not conserved, but fluctuates so as to generate the Boltzmann distribution $\exp(-\beta H)$ due to exchange of energy between the system and the thermal reservoir to which it is coupled. In order to generate these fluctuations in a MD simulation, so as to mimic the effect of the thermal reservoir, various methods have been proposed [29, 30, 31, 32, 33, 34]. Here only the Gaussian thermostat [33] will be mentioned, which is the one used for the LJ simulations of this thesis. Actually, this thermostat generates trajectories in the isokinetic ensemble, i.e. the ensemble where the total kinetic energy of the system is maintained at a constant value. So, while the position-dependent part of the distribution function is canonical, the momentum distribution is not. The reasons we used a Gaussian thermostat (i.e. the isokinetic ensemble) are both convenience and stability. When running the simulations at constant energy, one doesn't know the exact eventual temperature beforehand, and there may always be a slight energy drift in very long runs. By contrast, the Gaussian thermostat is extremely stable, keeping the kinetic energy constant to within many figures even after 10^7 or more timesteps. Moreover, in contrast to the widely used Nosé-Hoover thermostat, it is completely parameter free. However, since all ensembles are equivalent in the thermodynamic limit, then one may just as well use the isokinetic ensemble, especially when dealing with rather large

systems.

The new equations of motion are obtained by imposing a kinetic-energy constraint

$$\sum_{j=1} \frac{\mathbf{p}_j^{\,2}}{2m} = K \tag{3.7}$$

on the Hamiltonian dynamics of the system. So, Hamilton equations can be put into the form

$$\begin{aligned} \frac{\mathrm{d}\mathbf{r}_j}{\mathrm{d}t} &= \frac{\mathbf{p}_j}{m} \\ \frac{\mathrm{d}\mathbf{p}_j}{\mathrm{d}t} &= \mathbf{f}_j - \alpha \mathbf{p}_j \end{aligned} \tag{3.8}$$

where α is the single Lagrange multiplier needed to impose the constraint [35]. Then, using Gauss principle of least constraint, one arrives to a closed-form expression for α in the following way. Differentiating Eq. (3.7) once with respect to time yields

$$\sum_{j=1} \frac{\mathbf{p}_j}{m} \cdot \frac{\mathrm{d}\mathbf{p}_j}{\mathrm{d}t} = 0. \tag{3.9}$$

Thus, substituting the second of Eqs. (3.8) into Eq. (3.9) gives

$$\sum_{j=1} \frac{\mathbf{p}_j}{m} \cdot (\mathbf{f}_j - \alpha \mathbf{p}_j) = 0, \tag{3.10}$$

which can be solved for α giving

$$\alpha = \frac{\sum_j \mathbf{f}_j \cdot \mathbf{p}_j}{\sum_j |\mathbf{p}_j|^2}. \tag{3.11}$$

Once a proper algorithm has been set up, the system can be equilibrated at the desired density and temperature. Then the subsequent production run generates a trajectory in the equilibrium phase space that starts at some point $(\vec{\mathbf{r}}_i, \vec{\mathbf{p}}_i)$ and stops at some point $(\vec{\mathbf{r}}_f, \vec{\mathbf{p}}_f)$. The successive configurations produced at each timestep are used to store the instantaneous values assumed by certain phase space functions of interest. In practice it would be inappropriate to consider every configuration since neighboring configurations can be highly correlated. If $A(\vec{\mathbf{r}}(t), \vec{\mathbf{p}}(t))$ is the generic dynamical variable that depends on both coordinates and momenta of all particles, then its mean value is calculated as

$$\langle A \rangle = \frac{1}{M} \sum_{k=1}^{M} A(k), \tag{3.12}$$

where M is the number of configurations supposedly independent and A_k is the value A assumes in each of them. In Eq. (3.12) the ergodic hypothesis has to be invoked in order to justify equating trajectory averages with ensemble-based thermodynamic properties.

Also time correlation functions $C_{AA}(\tau) = \langle A(\tau)A(0)\rangle$ can be evaluated, according to their definition, averaging over different time origins the product of A at time k and A at a time τ later:

$$C_{AA}(\tau) = \frac{1}{k_{\mathrm{m}}(\tau)} \sum_{k=1}^{k_{\mathrm{m}}(\tau)} A(k)A(k+\tau), \tag{3.13}$$

where $k_{\mathrm{m}}(\tau)$ represents the maximum number of time origins available to perform the average, which is clearly a function of the delay τ (the larger τ the smaller k_{m}). As a consequence, the short-time part of $C_{AA}(\tau)$ is determined with a slightly greater statistics.

Despite the presence of some approximate recipes to estimate statistical errors in calculating averages [36], the method adopted in this thesis for the LJ simulations has been that of evaluating the standard deviation of the set of different determinations relative to independent runs. Although this approach is rather time-consuming, it has the merit of reducing the errors of a factor $1/\sqrt{N}$, where N is the number of independent runs.

Chapter 4

Velocity autocorrelation function of a low-density LJ fluid

4.1 Introduction

As evidenced in Ch. 2, the VAF is a key quantity for the study of the self dynamics in a fluid [10, 9, 8]. Indicating with $\mathbf{v}(0)$ the velocity of a generic particle at the instant $t = 0$, it expresses which is, on average, the projection of the velocity of the same particle at the instant t along the original direction of motion. That is,

$$Z(t) = \frac{\langle \mathbf{v}(0) \cdot \mathbf{v}(t) \rangle}{\langle \mathbf{v}^2 \rangle}. \tag{4.1}$$

Despite the simplicity of its definition, the VAF is a rather complex quantity to describe in detail, because it contains contributions from all the dynamical processes of the system, both diffusive and vibrational [37, 38]. A great number of works about the VAF were published in the late 60's thanks to the development of numerical simulation techniques [39, 40, 23]. Experimental determinations of the VAF spectrum, although possible in principle by means of Eq. (2.17), pose in practice some problems because of the extrapolation procedure to $Q = 0$.

The main reason why the VAF has received great attention at the beginning is to be found in the unexpected phenomenon of the *long-time tail* (LTT), evidenced for the first time in the works of Alder and Wainwright [39, 40]. Through simulations of the VAF of a system of hard spheres, these authors noticed that the long-time decay was not represented by an exponential,

as established by the Boltzmann theory, but by a power-law behavior of the type $At^{-3/2}$. This was the first observation of a LTT in correlation functions of microscopic variables of fluids. The effect was interpreted [40] by observing that the motion of a particle in the fluid generates around itself a sort of vortex that is able to "push" in some way the same particle along the initial direction of motion, so favouring a persistence of the correlation.

After these findings, numerous theoretical works have tried to give an explanation of the LTT. Substantially different approaches have been pursued: the hydrodynamic theory with its phenomenological equations [41, 42, 43] on the one hand, and the kinetic theory with the phenomenon of ring collisions [44] on the other. Even though they predict the same power law $At^{-3/2}$ for sufficiently long times, the results of the two theories differ in that the former derives the $t^{-3/2}$ dependence as the *asymptotic* time behavior of the VAF, while in the latter there is no claim of such a property.

Further simulation studies have concerned model fluids interacting with continuous potentials, in various thermodynamic conditions, aiming at an unambiguous assessment of the LTT [45, 46, 47, 48, 49, 50, 51, 52]. In fact, the effect of the mechanisms assumed to lie at the basis of the LTT makes it not observable under all conditions. For example, in too dense systems some dynamical effects, such as backscattering due to the bouncing of atoms off near neighbors, may become dominant and mask the LTT [46, 47].

In summary, a power-law decay has been established for various model fluids in at least some range of their thermodynamic states, although debated through confirmations and denials, as clearly recalled in Ref. [47]. In particular, a more recent two-dimensional hard-disk simulation performed on a very large system [51] has shown clear deviations of the VAF from the t^{-1} decay predicted by theory for a 2-D system. This result casts some doubt on the validity of the power law as the asymptotic time dependence also in real fluids.

The relevance of the VAF is, however, far from being confined to its very-long-time behavior. The initial decay was also studied [9, 8], but mostly by looking for an appropriate functionality of the first-order memory function $M_v^{(1)}(t)$ to be inserted into the memory equation (2.30), as recalled in par. 2.3.1.

The relative weight of the various processes that rule the decay of the VAF depends on the particular thermodynamic state of the fluid and their change determines the evolution of the

shape of the VAF itself. Thus, one would ultimately aim at a well-founded approach to the VAF analysis covering the whole time range from zero up to the longest time for which a VAF can be determined, including the LTT range if detected, and in the whole fluid-state (ρ,T) space.

In the first part of this thesis work, we pursue this goal by applying the multi-exponential method described in par. 2.4 to analyze the full-time behavior of the VAF of a Lennard-Jones fluid in a range of low-density, supercritical, states.

4.2 Simulations

The VAF of the (12-6) LJ fluid has been simulated through the MD technique described in Ch. 3, at thermodynamic states belonging to the slightly supercritical $T^* = 1.35$ isotherm and with densities ranging from the critical one ($\rho^* = 0.3$) to a value ($\rho^* = 0.6$) about halfway between the critical and the triple point density[1]. All the simulated states are reported in Fig. 4.1. This medium-density gas region was selected because a previous careful work [47] had

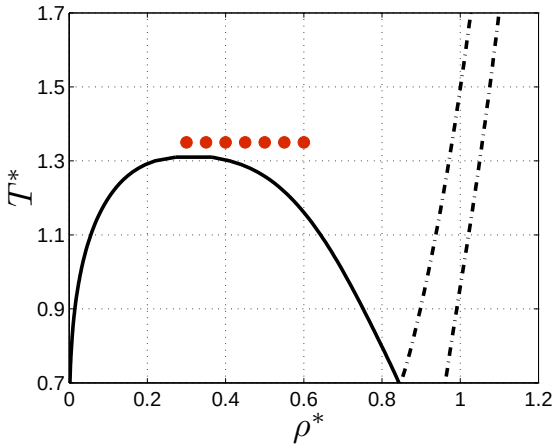

Figure 4.1: Red points represent the simulated states in the (ρ^*,T^*) plane. The black continuous line indicates the liquid-vapor coexistence boundary. The dot-dashed lines delineate the region of solid-fluid coexistence.

already given evidence of the presence of a $t^{-3/2}$ LTT for the $\rho^* = 0.3$ state. Thus, it was considered worthwhile to investigate if also nearby higher-density states showed such a LTT in the correlation. The simulation was carried out with the same number of particles, $N = 10976$, and the same (large) force cutoff $r_c = 6.5\,\sigma$ as in Ref. [47].

[1] As already introduced in Ch. 3, variables marked by an asterisk denote reduced quantities

To maintain the system at the required temperature, the Gaussian thermostat described in Ch. 3 has been employed. Moreover, the results of such an isokinetic simulation have been checked to be consistent with the correlation function obtained in the microcanonical ensemble. The equations of motion were integrated by means of the two-step leapfrog algorithm shown in Eq. (3.6) with a timestep of $\Delta t^* = 0.001$ and, to speed up the calculation of the forces, the cell subdivision method discussed in Ch. 3 was used. At each thermodynamic state, the normalized velocity autocorrelation function in Eq. (4.1) was computed on a grid with spacing $5\Delta t^*$ from zero up to a maximum time lag of $t^* = 20$, averaging over 10 independent runs of 10^7 time steps each. The angular brackets $\langle \cdots \rangle$ include also an average over all N particles.

Fig. 4.2 shows $Z(t)$ for all thermodynamic states considered here.

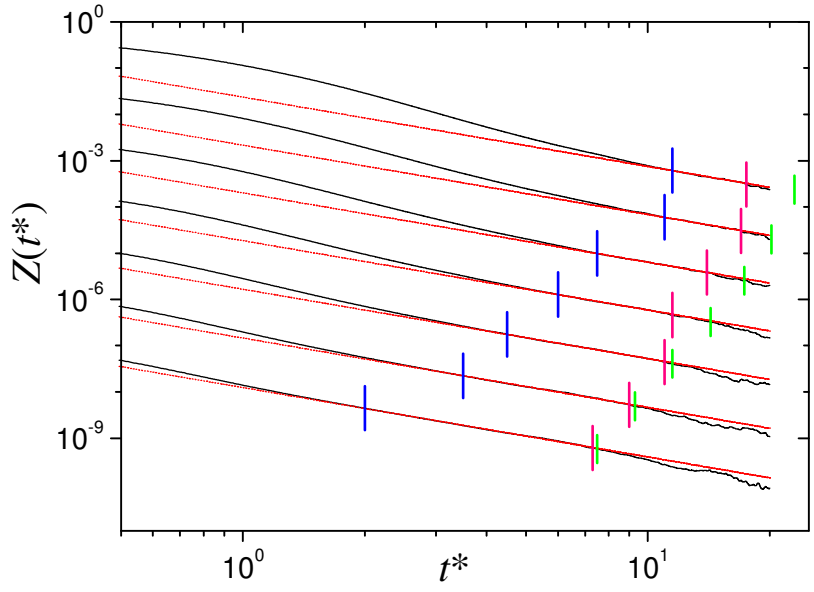

Figure 4.2: $Z(t^*)$ from simulation (black solid lines) is plotted for $t^* \geq 0.5$ showing its approach to the $(t^*)^{-3/2}$ behavior (red straight lines in the log-log scale). The curves are plotted in order of increasing density from top ($\rho^* = 0.30$) to bottom ($\rho^* = 0.60$), and for clarity each curve is shifted downwards by a factor of 10 with respect to the preceding one. The vertical bars mark the values of t_1^* (blue), t_2^* (pink), and t_R^* (green). See text for details.

As mentioned in Ch. 3, the use of periodic boundary conditions may introduce distortions into correlation functions [10, 36, 53], depending on the size of the simulation box, for time lags greater than the recurrence time t_R. The latter is usually defined as the time it takes a density fluctuation to propagate over a distance equal to the box length when traveling at the speed of

sound c_s, i.e., $t_R = (N/\rho)^{1/3}/c_s$, for a cubical box. Sound speed data were taken from Ref. [54] to calculate the t_R^* values displayed in Fig. 4.2, where the recurrence problem manifests itself in a reduction of the VAF intensity at the end of the reported time range. Actually, t_R^* slightly overestimates the time where problems with the simulation begin to show up, but this effect tends to diminish with increasing density.

A two-parameter fit of the function At^{-p} was performed to the tail of $Z(t)$ data in variable time windows and, for each density, the widest interval $t_1 \leq t \leq t_2$ within which the values of A, p, and the reduced χ^2 were found to be constant was empirically determined. The values of t_1 and t_2, also shown in Fig. 4.2, are consistent with what one would actually choose by visual inspection. The fitted p turned out to fluctuate around an average of 1.500 ± 0.005 without any density trend. Thus, a new fit with p fixed at $3/2$ was performed to obtain, at each density, a better determination of A. Such A values were used in Fig. 4.2 to draw the power-law dependence along with the simulated $Z(t^*)$. In Fig. 4.3 the fitted values of A are compared with

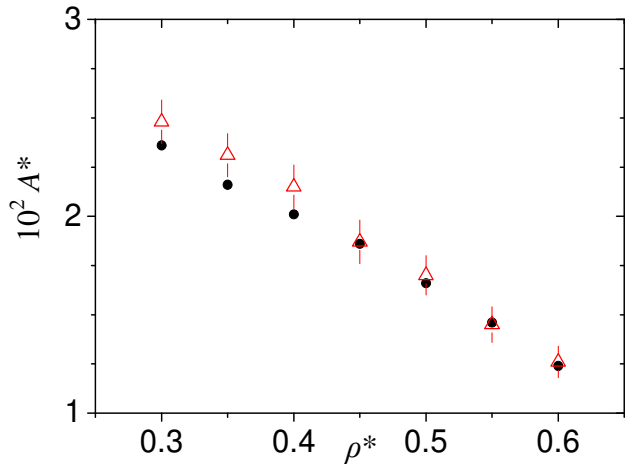

Figure 4.3: Amplitude A^* of the power-law behavior. The theoretical values (red triangles), calculated via Eq. (4.2), are shown together with those obtained by fitting the function $At^{-3/2}$ to the VAF data in the range $t_1 \leq t \leq t_2$. Error bars for the theoretical values are estimated from the uncertainties in the quantities D_S and ν. The errors on the fitted points are within the symbol size.

the predictions that the theories quoted in par. 4.1 equally provide as [9]

$$A = \frac{1}{12\rho[\pi(D_s + \nu)]^{3/2}}, \tag{4.2}$$

where D_s is the self-diffusion coefficient, and $\nu = \eta/(m\rho)$ and η are the kinematic and shear

viscosities, respectively. D_s was estimated from the time integral of the VAF [10, 9] according to Eq. (2.23), and obtaining values in agreement with those of Ref. [55], while η was taken from Ref. [48]. Evaluations of A, via Eq. (4.2), are in good agreement with the fitted values, especially at the higher densities. The slight discrepancy at lower densities might be due to the fact that the fit range shrinks with decreasing density.

4.3 Results

While in the previous section the $t^{-3/2}$ law was found to be a good representation of the LTT in the states studied here, the goal of this work was to obtain a full account of the whole VAF time dependence, since no such result is available yet. The exponential series expansion of time correlation functions, described in par. 2.4, is adopted here for such an attempt.

In the whole reliable range $0 \leq t \leq t_2$ of our LJ data, a remarkably accurate description of the VAF was obtained with two pairs of complex conjugate exponentials and four real exponentials (see Eq. (2.41)). It has been checked that, at all studied thermodynamic states, this set of exponential terms is the smallest one to be kept in Eq. (2.41) in order to obtain the required accuracy of the fit, which means that, if one wants to avoid an unjustified overparametrization of the fit function, this is univocally determined. Four constraints, provided by the sum rules of Eq. (2.45) with $k = 0, 1, 3, 5$, have been specified. Imposing these constraints does not merely provide a useful reduction in the number of free parameters, but also renders the model used here a much more accurate description of the VAF and its spectrum than it is customarily obtained. We are not aware, in fact, of any study of dynamical spectra where the finiteness of the sixth frequency moment was imposed. The reason why we do not enforce any sum rules with even k (apart from the normalization condition) is that the corresponding zero-time derivatives of the autocorrelation function are, in general, unknown beyond the $k = 2$ one. In the case of the VAF, for example, the computation of the fourth derivative of $Z(t)$ at $t = 0$ requires the knowledge of the three-body distribution function $g^{(3)}(\mathbf{r}_{12}, \mathbf{r}_{13})$. From the computational point of view, the fitting of the multiexponential model is performed by means of a program run in the Matlab environment, where the core least-squares-fit calculation is carried out by a built-in Levenberg-Marquardt-type minimization routine. Weights defined via the statistical uncertain-

ties evaluated in the VAF computation are used for the definition of the χ^2 to be minimized. The implementation of the sum rule constraints is performed by applying linear algebra routines to the solution of the system of equations that give the unfitted parameters in terms of the fitted ones.

A first check of the consistency of the applied fit function is its fulfillment of the $k = 2$ sum rule. Equation (2.19) for the short-time expansion of the VAF evidences that the second frequency moment is the square of the Einstein frequency Ω_0 reported in Eq. (2.14). For the LJ case this reads

$$\Omega_0^2 = 32\pi\rho^* \int_0^\infty \mathrm{d}r^*\, g(r^*) \left[22 \left(\frac{1}{r^*} \right)^{12} - 5 \left(\frac{1}{r^*} \right)^{6} \right], \tag{4.3}$$

and was calculated using the results of Monte Carlo simulations of $g(r)$ at the various densities [56]. Using the series (2.45) with the finite number of terms of the fit function, Ω_0^2 can be evaluated from the fitted I_j and z_j. The two values of Ω_0^2 obtained from Eqs. (4.3) and (2.45) were found to agree within 2% at $\rho^* = 0.30$ and better than 1% at all higher densities, indicating a good performance of both models and algorithms.

Figure 4.4 shows that the multiexponential fit curves agree perfectly with the VAF data at all densities. In particular, for times between t_1 and t_2 the fit residuals are at least as small as in a fit with the power law. The various components of the fit model are also shown in Fig. 4.4 for a more detailed understanding of the results. The oscillatory modes (labeled C1 and C2) are strongly damped and one of them (C1) is characterized by a very low intensity. These modes and the two faster decaying real exponentials (R1 and R2) mainly determine the VAF behavior at short and intermediate times, respectively. The role of the slower decaying exponentials (R3 and R4) can instead be better appreciated at the larger times displayed in the right panels of the figure. Notably, the LTT range ($t \geq t_1$) is described by the R3 and, predominantly, R4 terms. The latter, however, is apparently characterized by a time constant much longer than the other modes, suggesting the onset of a different (hydrodynamic-like) regime for the fluid. With increasing density, the short-time oscillatory mode progressively grows in importance with respect to the two fast decaying real modes R1 and R2. This is suggestive of the onset of bouncing effects in cages surrounding a given atom, which are typical of a dense liquid but may already start to form at lower densities as the packing fraction grows.

The fact that two exponential terms (R3 and R4) provide an accurate representation of the

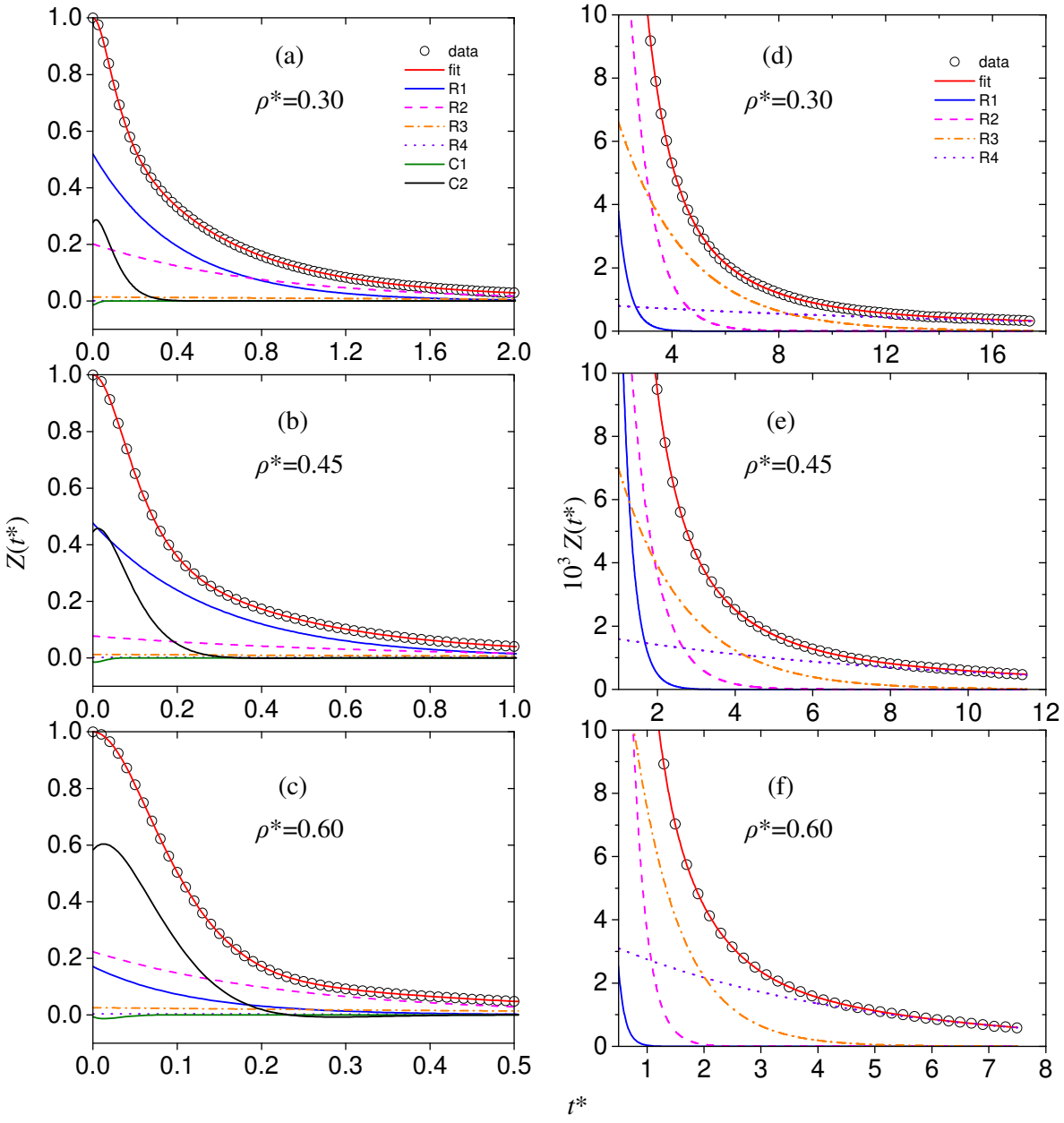

Figure 4.4: The simulated $Z(t^*)$ is displayed (symbols) for the three indicated densities together with the multi-exponential fit described in the text (red solid line through the data points). In the left frames, referring to short times, the various components of the fit function are also displayed separately according to the legend given in the top panel. R1 to R4 denote the real exponential terms ordered by increasing decay time. C1 and C2 indicate the pairs of complex conjugate exponentials. In the right panels, covering the remaining time range up to t_2^* , only the real terms are shown because C1 and C2 have already decayed to zero. For graphical clarity, not all available data points have been displayed.

MD data for $t_1 \leq t \leq t_2$, i.e. in the same range where the algebraic $t^{-3/2}$ dependence is detected, should not appear as a contradiction. Of course, this is not an absurd claim that the sum of two exponentials amounts to an algebraic function, but simply the statement that the two representations can only be assessed in the comparison with data of finite precision. In this respect, it has been already noted that in the above quoted range the multiexponential fit is at least as good as the $t^{-3/2}$ one.

It is intrinsic to the theory that the VAF decays by superposition of effects that can be identified with relaxation channels of different nature. Here it is learned, however, that these channels are limited in number to a few, and still fewer of them are sufficient to account for the LTT. Moreover, it is a natural consequence of the theory that, if VAF data were obtainable in a significantly wider range, additional slower-decay modes should eventually be added to the model and that these would account for contributions to the VAF of lesser and lesser intensity and located in the very far tail.

As already visible in Fig. 4.4, the slowly decaying real exponentials R3 and R4 have very small intensities. However, they account for the total VAF in the very important long-time range where all other terms have already fully decayed to zero. In Fig. 4.5, which displays the mode intensities as functions of density, it is seen that (i) C2 and R1 are the most intense modes, followed by R2, but (ii) the density dependence clearly suggests that the oscillating mode gains intensity at the expense of the fastest decaying real exponential one.

It's worthwhile to measure characteristic times of the various processes in units of "collision times", since all dynamical effects are ultimately determined by repeated collisions between particles, which become more frequent the higher the density. As a reference collision time it is customary to take the Enskog mean free time τ_E of a corresponding hard sphere fluid, the only system where such a quantity can be rigorously defined. For hard spheres of diameter σ, the Enskog kinetic theory predicts a mean time between collisions given by [8]

$$\tau_E = \frac{1}{4\rho\sigma^2 g(\sigma)} \sqrt{\frac{m}{\pi k_B T}}, \tag{4.4}$$

where $g(\sigma)$ can be obtained from the approximated Carnahan-Starling equation of state for hard spheres. Considering that $z_j = -1/\tau_j$ or $z_j = (-1/\tau_j) + i\omega_j$ for a real or complex mode, respectively, and evaluating the scaled quantities τ_j/τ_E for the time decays and $\omega_j\tau_E$ for the complex mode oscillation frequencies, it is possible to estimate the number of collisions involved in the

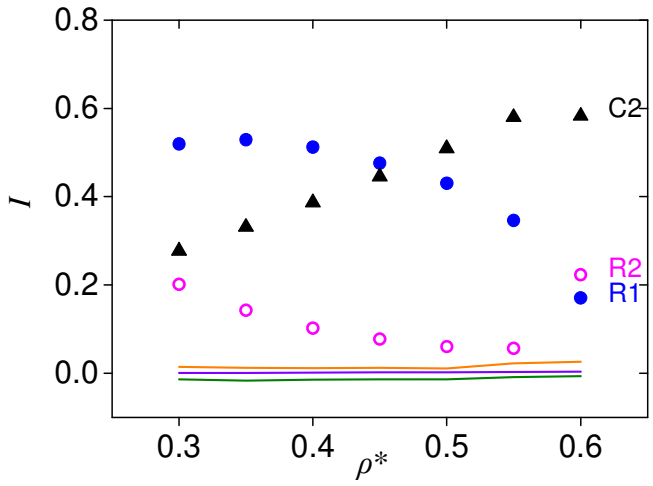

Figure 4.5: Amplitudes I of the fitted modes as functions of density. The three most intense modes are shown as symbols. The other modes have amplitudes too small to be clearly distinguishable on the scale of the figure and are displayed as continuous lines. For the complex modes the amplitudes of the sums of each pair of complex conjugate terms, given by $2\mathrm{Re}I$, are shown.

loss of correlation brought about by the various processes related to each fitted mode in Eq. (2.41). Figure 4.6(a) shows the density dependence of τ/τ_E. The oscillatory modes have the shortest decay times, which, together with that of R1, are less than, or of the order of, one collision time. R2 is also a relatively fast process related to a very small number of collisions. These modes correspond qualitatively to the mentioned binary collision components. There also appears a mode (R3) with τ/τ_E of the order of ten. This intermediate value denotes a process where more collisions are involved but still not in such a number as to suggest a truly cooperative damping mechanism. However, the most striking result is the great gap between the first three real modes and the fourth one (R4), which has a decay time of the order of 60 collisions, revealing its true multiparticle, collective origin. These observations are quantitative confirmations of the Alder and Wainwright findings, but also show that the loss of velocity correlation is a consequence of more than one relaxation process, ranging from the single-collision fast processes R1, C1, and C2 to the slow, hydrodynamic-like one, R4. Figure 4.6(b) confirms that the oscillations the complex modes have a fast nature. In particular, the C2 pair is characterized by a frequency of the order of the inverse of Enskog time.

More insight into the effects of increasing density is gained by considering the relative

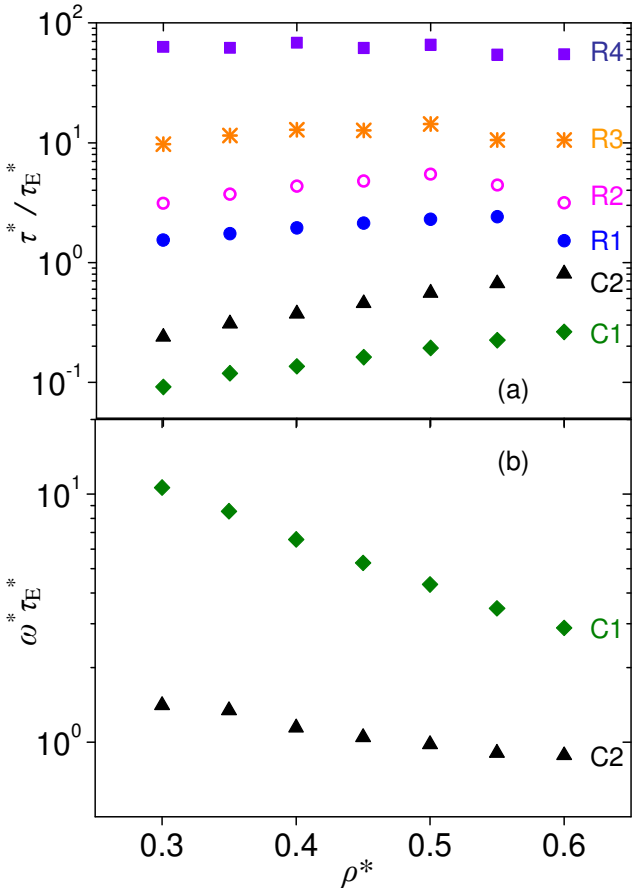

Figure 4.6: Parameters of the exponential fit. (a) Decay times τ_j of the fitted exponentials in units of τ_E as functions of density. (b) Product $\omega_j \tau_E$ of the two complex modes.

weights $w_j = (I_j/z_j)/\sum_h (I_h/z_h)$ of the various modes defined as their fractional contribution to the integral of the VAF. In order to present the density trends in a simpler but more effective way, modes are combined in Tab. 4.1 into three groups consisting of the complex modes, the two faster real ones, and the two slower ones. The interpretation of Tab. 4.1 is straightforward. By moving toward dense fluid conditions, the slow modes play an increasing role to account for

ρ^*	0.30	0.35	0.40	0.45	0.50	0.55	0.60
C1 + C2	7.8	10.6	14.3	18.6	23.6	30.1	34.1
R1 + R2	81.0	78.1	73.9	68.2	62.9	50.8	44.5
R3 + R4	11.1	11.3	11.9	13.2	13.4	19.1	21.4

Table 4.1: Percent contribution of the fitted modes grouped as shown in the first column, to the integral of the VAF.

the hydrodynamic-like behavior, which is also responsible for the emergence of the LTT. On the other hand, for the fast modes (C1+C2 and R1+R2), essentially governed by single-collision processes, one observes a shift towards a progressively stronger oscillatory nature in parallel with the formation of better structured nearest-neighbor cages. This is the same phenomenon that, when the density of the liquid state is reached, will have increased to the point of making the total VAF display a negative part.

Chapter 5

Velocity autocorrelation function of a high-density LJ fluid

5.1 Introduction

The effectiveness of the analysis described in the previous chapter, naturally suggested to extend the multi-exponential approach to the VAF of a LJ system to thermodynamic states closer to a liquidlike, and even true-liquid, behavior, for a number of reasons. One is the fact that it is still unclear whether the LTT persists in denser and/or colder fluids, given that the overall decay to zero reduces the VAF intensity to very small values in the time range where the LTT should be its dominant feature. However, a more important point is the fact that, so far, no theory has produced a model able to describe, as a whole and in an accurate way, both the negative portion of the VAF and its subsequent growth to positive values, followed by the final decay to zero from above. This is the time range where oscillatory components of the total VAF develop as the dynamical behavior tends to the one typical of a liquid.

The interpretation of the frequency spectrum of the VAF as a density distribution of states, which is straightforward for crystalline solid [12], when extended to the fluid phase provides, in principle, a route to the investigation of the dynamics also for what concerns the collective motions. However, no clear way of carrying out this task has been developed so far. It is, thus, a main goal of the subsequent part of this thesis to explore the possibility of exploiting the mode decomposition allowed for by the exponential expansion to relate the various VAF components

to specific collective and single-particle motions typical of a fluid.

Therefore, additional MD simulations were performed in order to extend the analysis carried out in Ch. 4 both to the high density supercritical fluid and to some liquid states at subcritical temperatures. The results of this analysis will show that the evolution of the fitted exponential terms in number, nature, intensity and time scale, is extremely helpful for the identification of some of the fitted modes with specific dynamical properties. In particular, besides the already recognized role of slowly decaying exponentials in accounting for the LTT, which is confirmed by the new simulations, we also demonstrate the correspondence between the highest-frequency complex mode and the properties of the dispersion curve of longitudinal acoustic waves. Moreover, we will show in the following that the remaining exponential modes account for the transverse collective dynamics and that their density evolution provides clear evidence of a crossover.

In this context, it is worth to mention that recent studies [57, 58, 59, 60, 61, 62] have discussed the existence of a transition between a low-density gaslike and a high-density liquidlike dynamical regime for a supercritical fluid. Actually, different criteria have been proposed in order to establish the location and the nature of such a crossover. Indeed, the authors in Refs. [57, 58] characterized it with the onset of positive dispersion in longitudinal acoustic waves when crossing the so-called Widom's line, which is an extension of the liquid-vapor coexistence line in the supercritical region and is defined as the thermodynamic locus of specific heat maxima. Conversely, in Refs. [60, 61] the transition has been connected to the onset of a non-monotonic time dependence of the VAF, and a different line is introduced, for which the name of Frenkel line has been proposed.

5.2 Simulations

MD simulations of the VAF for the (12-6) LJ fluid along the slightly supercritical $T^* = 1.35$ isotherm were already reported for particle number densities up to $\rho^* = 0.60$ (see par. 4.2). Here, higher density states (with ρ^* varying from 0.65 to 0.95 in step of 0.05) at the same temperature are considered, reaching a density very close to that where isothermal solidification begins. Moreover, we simulated a few colder liquid states along the $\rho^* = 0.80$ isochore and below the critical isotherm, with $T^* = 1.20, 1.10, 1.00, 0.90$. The point at $T^* = 1.35$, $\rho^* = 0.80$ thus

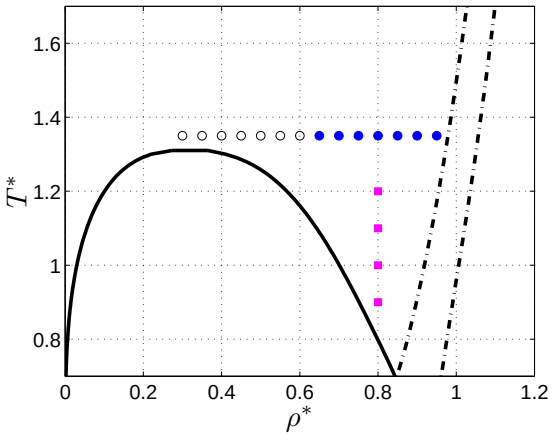

Figure 5.1: Simulated LJ states in the (ρ^*,T^*) plane. Black open circles indicate the points investigated in the previous work (see par. 4.2). Blue dots are higher density states on the same $T^* = 1.35$ isotherm, while pink squares are at lower temperatures along the $\rho^* = 0.80$ isochore. The black continuous line indicates the liquid-vapor coexistence boundary. The dot-dashed lines delineate the region of solid-liquid coexistence.

belongs to both the isotherm and the isochore here considered. Figure 5.1 shows the state points in the (ρ^*,T^*) plane, including for completeness and reference also the lower density states of Fig. 4.1. All simulations have been performed, and the respective VAF computed, exactly in the same way as described in par. 4.2, here recalling only that the same number of particles $N = 10976$ was used in a cubical box for all states.

For all thermodynamic states considered here, Fig. 5.2 shows the low-intensity part of $Z(t)$ at small values of the reduced time t^*. Starting from a monotonous decay of $Z(t)$, the increase of density at constant T^* (Fig. 5.2(a)) leads to the presence of a plateau which soon changes into a relative minimum. This already happens when $Z(t)$ still remains everywhere positive, but with a further density increase this minimum deepens and shifts to smaller times, the curve crosses the zero axis to become negative, and another shallow minimum appears at a later time. The changes of shape in cooling the system at constant density, shown in Fig. 5.2(b), are less marked and are characterized essentially by a strengthening of the negative portion of $Z(t)$.

The behavior of $Z(t)$ at long times is best appreciated in Figs. 5.3 and 5.4 where the log-log scale is used for an easy comparison with a power-law time dependence. As already recalled in par. 4.2, spurious effects due to the periodic boundary conditions affect the VAF at time lags greater than the recurrence time t_R, reported in Tabs. 5.1 and 5.2. We also display t_R^* in

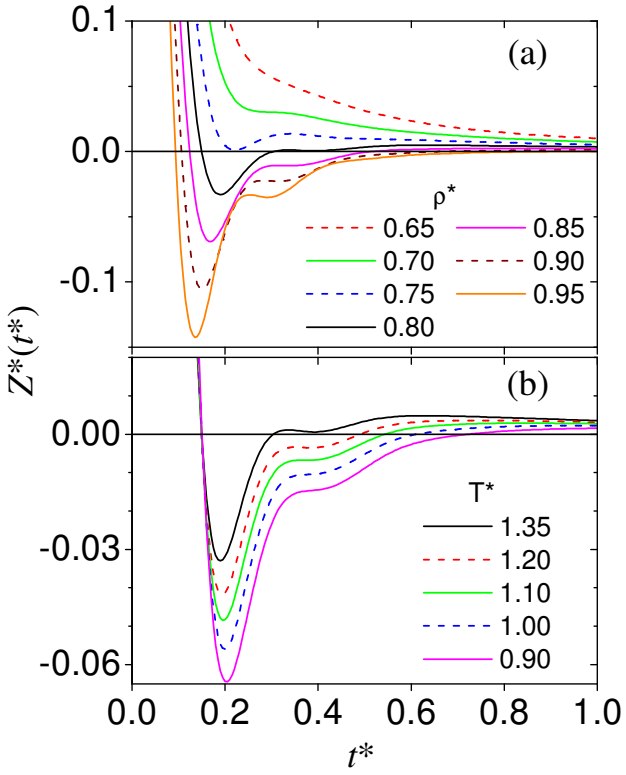

Figure 5.2: Simulated $Z^*(t^*)$ for $t^* \leq 0.1$. Only the part of $Z^*(t^*)$ close to the horizontal axis is shown, and the steep decrease from the initial value is omitted for clarity. (a) States along the $T^* = 1.35$ isotherm at the indicated densities. A lower-density curve stays above a higher-density one. (b) States along the $\rho^* = 0.8$ isochore at the indicated temperatures. Higher temperatures correspond to upper curves. The middle line in (a) and the top line in (b) are the same curve.

Figs. 5.3 and 5.4, where the recurrence problem shows up as a spurious overall reduction of the VAF intensity, which also displays some oscillatory and rapidly increasing noisy behavior.

It can be noted that, at constant temperature, t_R markedly decreases with increasing density due to simultaneous reduction of the box size and increase of c_s, while, at constant density, t_R increases weakly with decreasing temperature due to the reduction of c_s brought about by the lowering of the particle thermal speed. Further analysis of the VAF have been performed, at each state, using data in the respective $0 \leq t \leq t_R$ ranges only. With literature values of D_s and η [55], reported in Tabs. 5.1 and 5.2, equation (4.2) was applied to calculate A and to draw the power-law dependence in Figs. 5.3 and 5.4.

It appears that at all thermodynamic states the VAF tail approaches the $At^{-3/2}$ line, but such

ρ^*	0.65	0.70	0.75	0.80	0.85	0.90	0.95
T^*	1.35	1.35	1.35	1.35	1.35	1.35	1.35
t_R^*	6.2	5.2	4.5	3.8	3.3	2.9	2.6
τ_E^*	0.065	0.054	0.045	0.038	0.031	0.026	0.022
t_R^*/τ_E^*	96	96	100	101	105	111	120
D^* (from Ref. [55])	0.183	0.150	0.122	0.097	0.076	0.058	0.042
η^* (from Ref. [55])	0.99	1.21	1.52	1.97	2.59	3.37	4.81
$10^2 A^*$ (from Eq. (4.2))	1.03	0.83	0.64	0.46	0.32	0.22	0.14

Table 5.1: Recurrence time for the simulations and properties of the LJ states on the $T^* = 1.35$ isotherm. The Enskog mean time between collisions for equivalent hard spheres is given, together with the diffusion coefficient and the viscosity [55]. The coefficient of the $At^{-3/2}$ power law is obtained through Eq. (4.2). All quantities are expressed in reduced units.

ρ^*	0.80	0.80	0.80	0.80	0.80
T^*	1.35	1.20	1.10	1.00	0.90
t_R^*	3.8	4.0	4.2	4.3	4.6
τ_E^*	0.038	0.040	0.042	0.044	0.046
t_R^*/τ_E^*	101	100	101	98	100
D^* (from Ref. [55])	0.097	0.085	0.077	0.068	0.060
η^* (from Ref. [55])	1.97	1.97	2.02	2.05	2.09
$10^2 A^*$ (from Eq. (4.2))	0.46	0.46	0.45	0.44	0.43

Table 5.2: Same as in Tab. 5.1 for the thermodynamic states along the $\rho^* = 0.80$ isochore. The first state at $T^* = 1.35$ also appears in Tab. 5.1.

a time dependence could possibly be determined quantitatively *by a fit* only for $\rho^* \leq 0.75$ at $T^* = 1.35$, while at higher densities and for all states at lower temperatures there is no time range where $Z(t)$ overlaps the power-law behavior. As pointed out also by McDonough et al. [46], this fact excludes the possibility of a *direct* detection of the LTT behavior at high density, although in other works different claims have been made as, for example, by Meier et al. [49] who found a power-law dependence in LJ also at high density but with a different exponent, or by Williams et al. [50] who did find a $t^{-3/2}$ behavior in a HS liquid. We will show in the following paragraph that the presence of an LTT can be established through the exponential mode analysis.

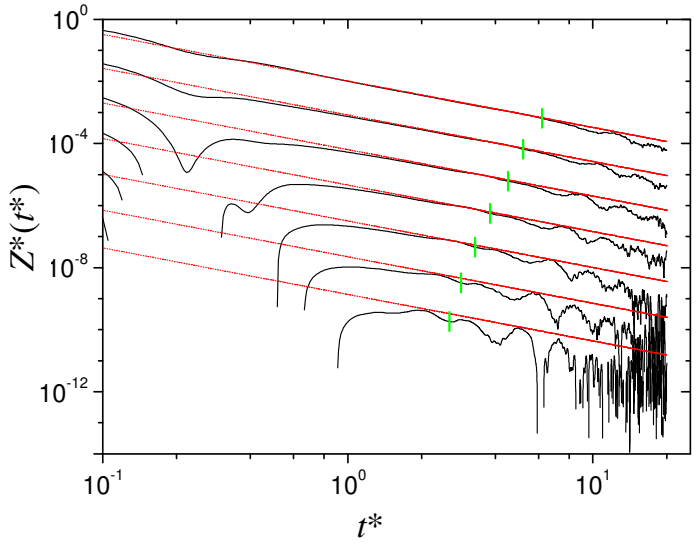

Figure 5.3: Log-log plots of $Z^*(t^*)$ from simulation (black solid line) at $t^* \geq 0.1$ for the states along the $T^* = 1.35$ isotherm. The $(t^*)^{-3/2}$ behavior (red straight lines) is calculated with the theoretical values of the coefficient A from Eq. (4.2). Curves are plotted in order of increasing density from top ($\rho^* = 0.65$) to bottom ($\rho^* = 0.95$), and for clarity each curve is shifted downwards by a factor of 10 with respect to the preceding one. The vertical green bars mark the values of t_R^*.

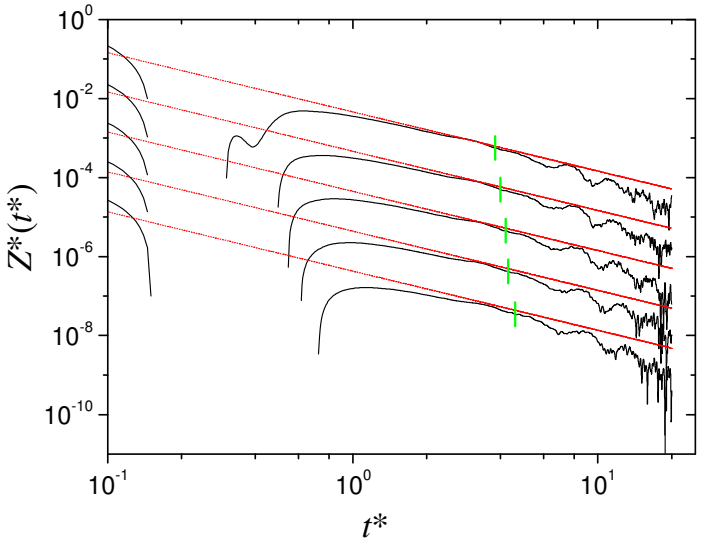

Figure 5.4: Same as in Fig. 5.3 for the thermodynamic states along the $\rho^* = 0.80$ isochore. Curves are plotted in order of decreasing temperature from top ($T^* = 1.35$) to bottom ($T^* = 0.90$) with each curve shifted downwards by a factor of 10 with respect to the preceding one.

5.3 Results

For all thermodynamic states considered here, excellent fits to the VAF data in the range $0 \leq t \leq t_R$ have been obtained with the models described here below and summarized in Tab. 5.3. The left frames of Fig. 5.5 show examples of the fitted curves, highlighting the excellent agreement between data and models.

ρ^*	T^*	C1	C2	C3	R0	R1	R2	R3	R4
0.65	1.35	×	×	—	—	×	×	×	×
0.70	1.35	×	×	×	—	—	×	×	×
0.75	1.35	×	×	×	—	—	—	×	×
0.80	1.35	×	×	×	—	—	—	×	×
0.85	1.35	×	×	×	—	—	—	×	×
0.90	1.35	×	×	×	×	—	—	—	×
0.95	1.35	×	×	×	×	—	—	—	×
0.80	1.35	×	×	×	—	—	—	×	×
0.80	1.20	×	×	×	—	—	—	×	×
0.80	1.10	×	×	×	—	—	—	×	×
0.80	1.00	×	×	×	—	—	—	—	×
0.80	0.90	×	×	×	—	—	—	—	×

Table 5.3: Composition of the fit models. Labels C1 to C3 denote pairs of complex conjugate modes. The modes labeled R0 to R4 correspond to real exponentials. Each mode is indicated as present (×) or absent (—) in the fit model for a given thermodynamic state.

At the lowest density ($\rho^* = 0.65$), the fit model reported in par. 4.3 works very well, in continuity with the low-density states analyzed in Ch. 4. Keeping the same labeling of the modes, there are two pairs of complex modes (C1 and C2) and four real modes (R1 to R4, numbered in order of increasing decay time). The C1 pair amounts to a very fast, very strongly damped oscillation, required for a good fit of the very-short-time data points, but of negligible importance at later times due to its extremely low intensity. This feature is present at all investigated states and will not be discussed further.

Moving along the $T^* = 1.35$ isotherm towards higher densities, Tab. 5.3 evidences two modifications of the optimum fit model: (a) a third pair of complex modes (C3) appears for

$\rho^* \geq 0.70$, and (b) the faster-decaying real exponentials disappear (R1 first for $\rho^* \geq 0.70$, then also R2 for $\rho^* \geq 0.75$). Finally, at the two highest densities, R3 also vanishes, while another real mode labeled R0 is required (the reason to keep R0 distinct from other real modes will be discussed later). Moving along the $\rho^* = 0.80$ isochore, the composition of the fit model remains unchanged while T^* is reduced, apart from a similar disappearance of R3 at the two coldest states.

In the following paragraphs we will show in detail how different dynamical processes can be associated to a sensible regrouping of the various modes. These are grouped in the way indicated by the legend in Fig. 5.5(b), for the reasons explained below.

The multi-exponential analysis of $Z(t)$ facilitates considerably the interpretation of the spectrum of the VAF in terms of the contribution of different dynamical processes, because Eq. (2.41) applied to $Z(t)$ immediately translates, upon FT, into a corresponding series expression for $\hat{Z}(\omega)$ where each real exponential transforms into a Lorentzian line (see Eq. (2.42)), while a pair of complex exponentials gives rise to a pair of distorted Lorentzian lines (see Eq. (2.43)). Once the various modes are determined by fitting the appropriate model to $Z(t)$ data, one automatically obtains the decomposition of $\hat{Z}(\omega)$ in terms of the corresponding centered or shifted spectral lines. This fact is exploited in the right frames of Fig. 5.5 where the spectral contribution of each group of modes is displayed together with $\hat{Z}(\omega)$ and the FT of the total fit curve.

5.3.1 The LTT

At low density we have shown in par. 4.3 that the R3 and, predominantly, R4 terms describe the LTT, with the latter characterized by a time constant much longer than that of the other modes and of the order of about 50-80 if measured in units of τ_E. This fact, revealing its multi-collisional, many-particle nature in agreement with the onset of a hydrodynamiclike regime, has now been found to hold true when going towards the high-density gas or cold liquid conditions investigated here. Figure 5.6 displays the sum of these slow decaying exponentials (or R4 alone when R3 is missing) and shows that an LTT is also found at the thermodynamic states studied in this work but its time dependence is compatible with an effective $t^{-3/2}$ behavior only at the lowest densities, as mentioned in par. 5.2.

A simple inspection of Figs. 5.3 and 5.4, compared with the analogous Fig. 4.2 of par. 4.2,

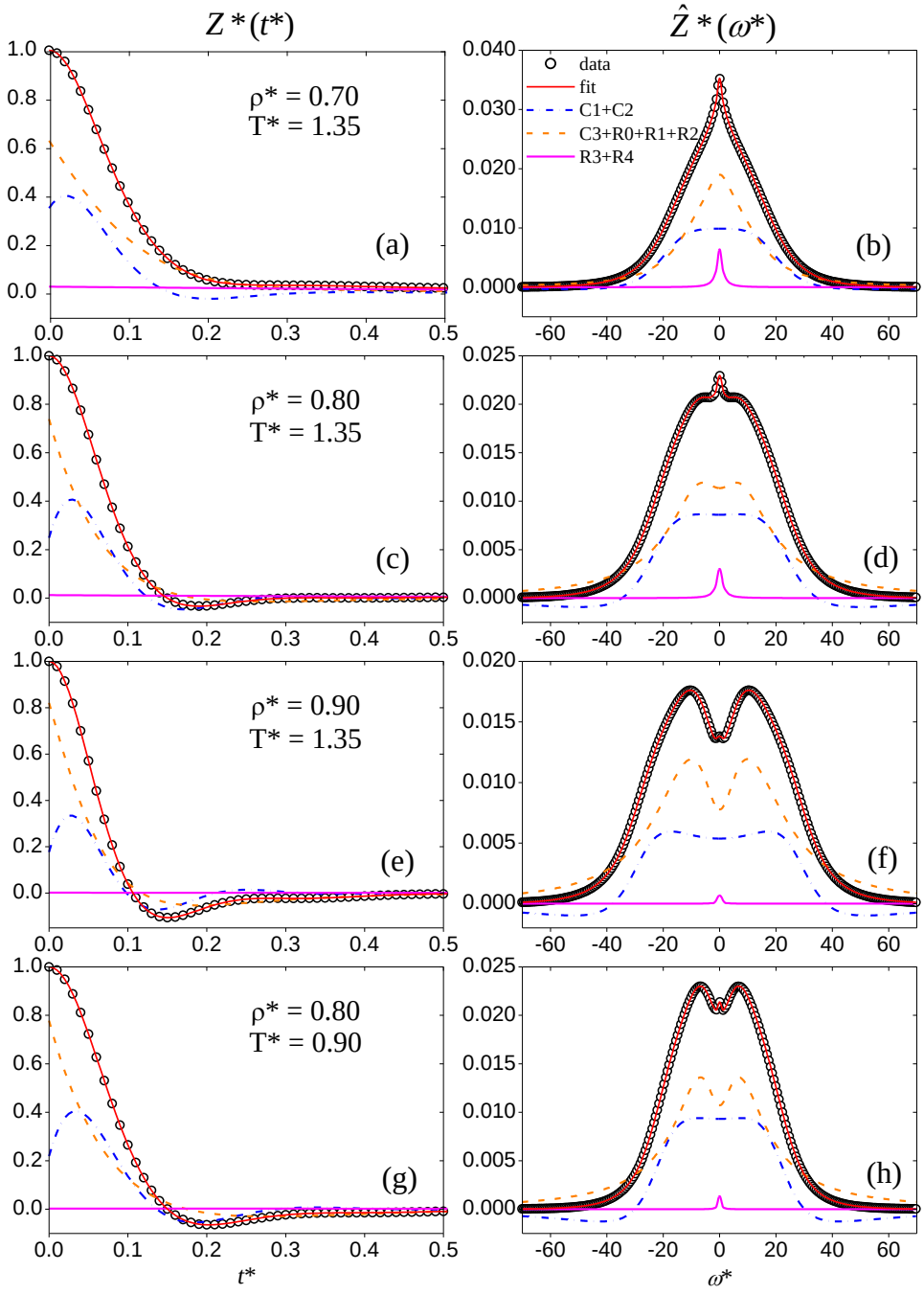

Figure 5.5: $Z^*(t^*)$ and $\hat{Z}^*(\omega^*)$ at four thermodynamic states. In the left frames, MD data for the VAF (symbols) and the multi-exponential fit (red solid line through the points) are displayed at short times. The various components of the fit function, grouped together as indicated by the top right labels, are also displayed separately. In the right panels, the corresponding FT's are shown. For graphical clarity, not all available data points have been displayed.

shows that the time range where an LTT can emerge as a salient feature of the VAF shrinks on the short-time side due to the growth of the VAF negative part, and on the long-time side because of the much smaller values of t_R, beyond which the data become unreliable. This explains why at the densest or coldest states the fitting cannot determine more than just one exponential (R4). As remarked in par. 5.2, in so narrow a range it would be virtually impossible to fit any specific time behavior assumed to represent directly the LTT alone. The multi-exponential analysis, however, exploiting the knowledge of the VAF in the whole time range $0 \leq t \leq t_R$, has a far better sensitivity to, and allows for the determination of, its slowly decaying long-time part. It

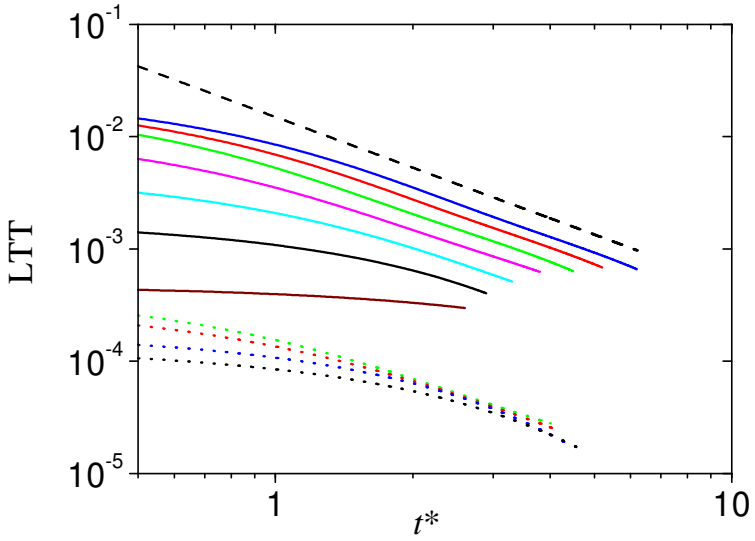

Figure 5.6: Contribution of the sum of the R3 and R4 terms to the VAF. Solid curves refer to thermodynamic states at $T^* = 1.35$ and are plotted in order of increasing density from top ($\rho^* = 0.65$) to bottom ($\rho^* = 0.95$). Dotted curves refer to states at $\rho^* = 0.80$, plotted in order of decreasing temperature from top ($T^* = 1.20$) to bottom ($T^* = 0.90$) and have been divided by a factor of 20 for graphical clarity. The dashed line is the $(t^*)^{-3/2}$ function, arbitrarily scaled.

also follows from the above observation that a more accurate determination of the long-time VAF dependence in a dense fluid may only be obtained through a substantial increase of t_R, i.e. by using larger simulation boxes with a number N of atoms at least one order of magnitude larger than the present one.

The fact that the slow decaying exponentials are indeed able to describe the LTT is even more evident if one looks at the spectra reported in the right part of Fig. 5.5, which show the

presence of a tiny but clearly visible tip at $\omega = 0$. This is the spectral signature of the LTT which, assuming a $t^{-3/2}$ power-law dependence, would appear as a $\sim -\sqrt{\omega}$ cusp. The multi-exponential fit shows that such a pathological frequency behavior is not justified and can be avoided, since a simple continuous function like the sum of the centered Lorentzian lines corresponding to the R3 and R4 modes accounts very well for the spectral representation of the LTT, which is displayed as the by far weakest component, confined to extremely low frequencies, of the spectra of Fig. 5.5. Accordingly, the modeling of the LTT in the form of an algebraic time dependence is also not necessary.

5.3.2 Sound modes

The two complex modes forming the C2 pair define an exponentially damped oscillation that in the previous chapter (see par. 4.3) was found to be characterized by a frequency $|\mathrm{Im} z|$ close the Enskog collision frequency and a decay time $\tau = -1/\mathrm{Re}\, z$ slightly smaller than τ_E. As the density was increased isothermally from $\rho^* = 0.30$ to $\rho^* = 0.60$, a steady increase of τ/τ_E by nearly a factor of 4 was observed, while $\omega\tau_E$ remained practically constant. Two facts that show that this oscillatory motion becomes better defined, though still strongly damped. Also, we noted that the fractional contribution of C2 to the VAF time integral clearly increases with density (see Tab. 4.1).

In the work illustrated in the previous chapter, the C2 oscillation was not associated to any specific dynamical process, apart from noting that its growing intensity points to an increasing relevance of vibratory motions likely related to the bouncing of atoms off their neighbors. However, the above mentioned characteristics of this component of the VAF are all compatible with the suggestion that what is accounted for by the C2 pair is the dynamics of collective motions due to propagating longitudinal waves. In fact, sound propagation occurs at any density, but when approaching dense fluid conditions the sound speed increases and the visibility of sound modes is enhanced.

The connection between VAF and collective dynamics of fluids is accomplished if one interprets the VAF frequency spectrum as a generalized overall “density of states”. This concept is of standard use in the phonon theory of both harmonic [12] and anharmonic crystals [63], and has also been applied to vibrations in amorphous solids [64] and glasses, and to internal

degrees of freedom of polyatomic molecules. In the case of liquids, a connection between the frequency density distribution of vibrational states and the spectrum of the VAF has been made in Refs. [65, 66] and used, for example, in the framework of the so-called normal modes analysis in various formulations [67, 68]. It has to be noted that the relationship between collective dynamics and density of states is a general property, not restricted to the longitudinal-wave case only. For example, in a recent work [69], the density of states of the crystal phase has been used to interpret dynamic structure factor data of a liquid metal, where an excitation was observed at frequencies close to those of the transverse phonon density of states and was therefore assigned a transverselike character.

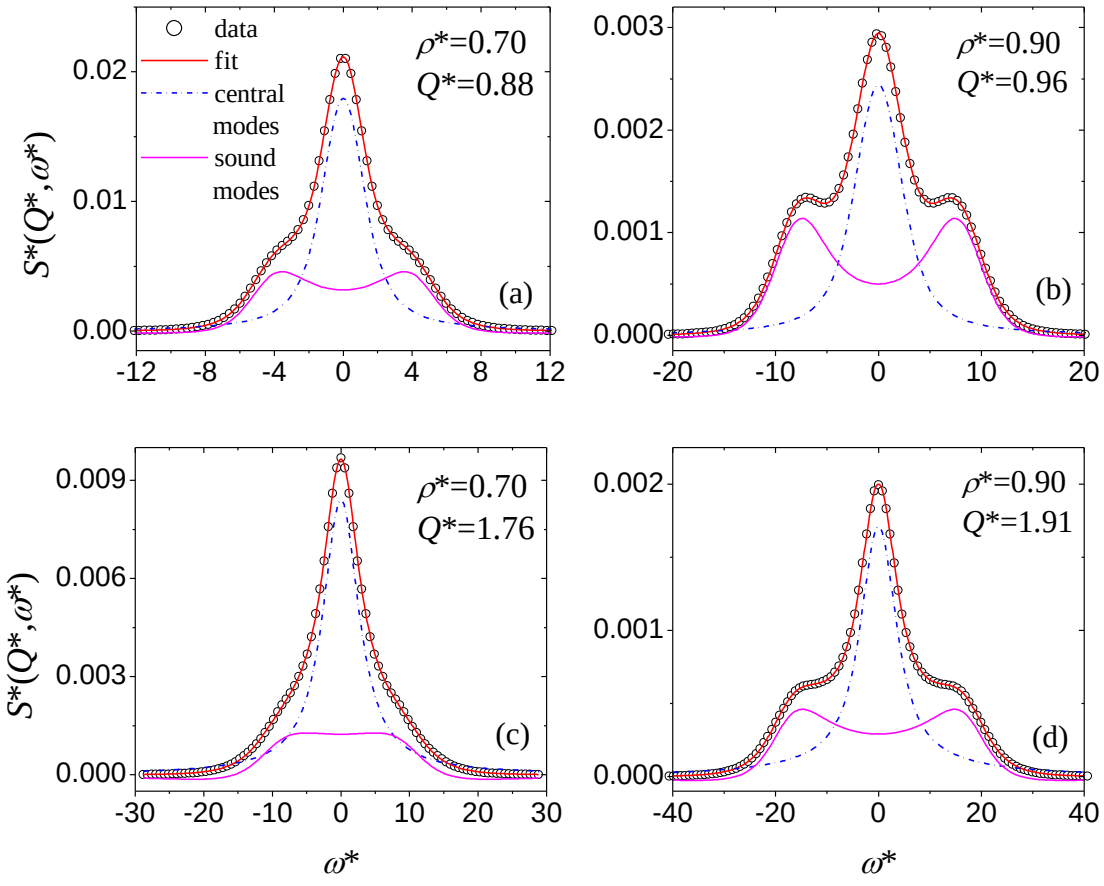

Figure 5.7: Simulated $S(Q,\omega)$ (dots) at two densities and two Q values indicated by the labels. Also shown are the VE fits (solid lines through the data points) and the partial contributions to the fit of the sum of the two central modes and of the two sound modes.

As already stated in par. 4.1, the VAF and its spectrum contain all kinds of dynamical infor-

mation relative to both diffusive and vibrational motions. This was evidenced by the treatment of Gaskell and Miller [37, 38] where, under reasonable assumptions, $Z(t)$ could be written in terms of both self and collective functions. Here we show, in particular, that the C2 pair has a clear and direct quantitative connection to the dispersion curve of the longitudinal acoustic modes.

In order to do so, we also carried out MD simulations of the intermediate scattering function $F(Q,t)$ and, through Fourier transformation, we derived the dynamic structure factor $S(Q,\omega)$ at a number of wavevectors Q for each density. In this case we used 2048 particles with a simulation length of $1.2 \cdot 10^6$ time-steps of duration $\Delta t^* = 0.001$. The Q values were multiples of the minimum Q value allowed, at each density, by the respective box size. With the same simulations we also computed the transverse current correlation spectra that will be discussed in the next paragraph. A smaller number of particles than that used in the simulations of the VAF was allowed because the correlation functions in consideration decay much faster (without long-time tails), so that a shorter t_R is large enough.

The $S(Q,\omega)$ spectra where fitted by means of the viscoelastic (VE) model line shape (for all details of the VE model see Ref. [28]), which provided a very accurate description of the dynamics of density fluctuations in various fluids [4]. Examples of $S(Q,\omega)$ simulated spectra with the corresponding VE fit curves are shown in Fig. 5.7. The fits are of excellent quality at all Q and density values, and allowed us to extract the parameters relevant to the description of sound modes, namely the frequency ω_s and the damping z_s. These are plotted in Fig. 5.8(a) and Fig. 5.8(b), respectively.

In much the same way as the density of crystal phonon states peaks at frequencies where the dispersion branches have a horizontal tangent [12], the contribution of sound modes to the total VAF spectrum of a liquid is also expected to be centered around the top frequency value of the sound dispersion curve. Figure 5.8(a) shows that the frequency of the fitted C2 pair is very close to the maximum sound frequency, with an increasingly better agreement as the density grows. In Fig. 5.5, contrary to the crystal case, $\hat{Z}(\omega)$ does not display a clear shoulder at the acoustic frequencies $\pm|\mathrm{Im}z_{C2}|$, because its overall shape is also determined by other contributions of different dynamical origin. Thus, one can well appreciate the advantage brought about by the possibility of extracting specific partial contributions to the total $\hat{Z}(\omega)$: the

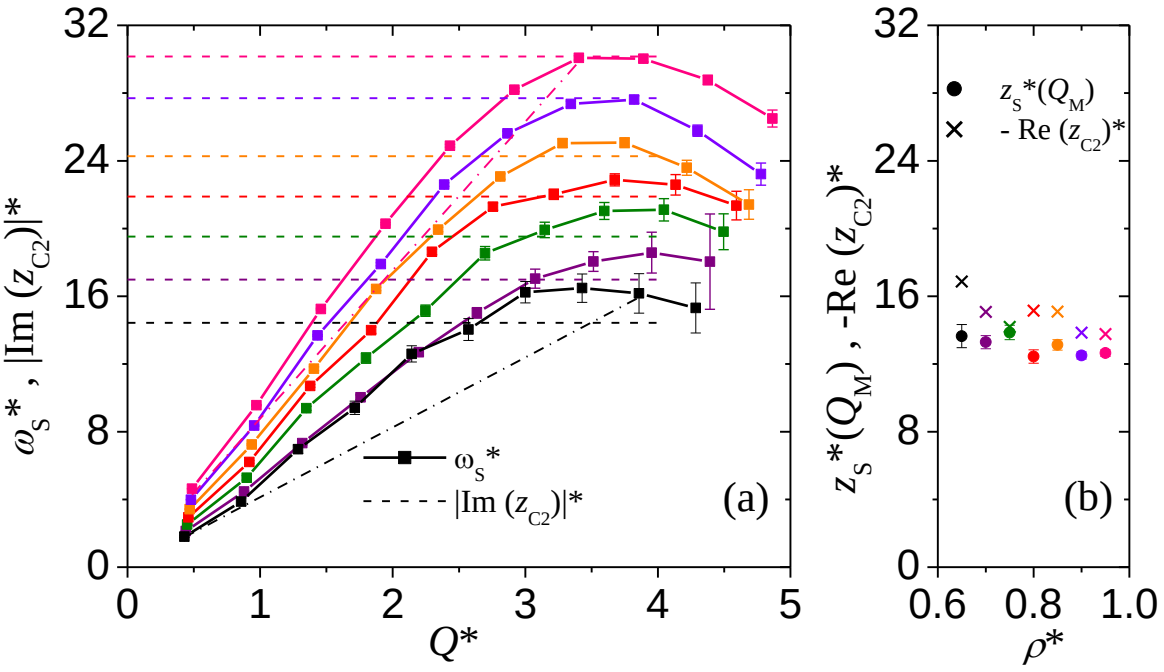

Figure 5.8: (a) The curves joining symbols with error bars are the dispersion curves $\omega_s^*(Q^*)$ of the longitudinal acoustic mode along the $T^* = 1.35$ isotherm, in order of increasing density from bottom ($\rho^* = 0.65$) to top (($\rho^* = 0.95$)). Dashed lines, in the same order, mark the corresponding values of the C2 oscillation frequency. The hydrodynamic dispersion straight lines $c_s^* Q^*$ are also shown (dash-dots) for the highest and the lowest density. (b) Damping $z_s^*(Q_m^*)$ of the longitudinal acoustic mode (dots with error bar) at $Q^* = Q_m^*$, i.e. where the respective dispersion curve reaches its maximum value in (a), and damping $-\mathrm{Re}(z_{C2})^*$ of the complex pair C2 (crosses). The color code is the same in the two frames.

spectral partial components relative to C1 and C2 mode group do, in fact, show clear shoulders at nonzero frequencies, as seen in Fig. 5.5.

Besides the frequency, also the broadening of the acoustic line in $S(Q,\omega)$ directly reflects itself into a corresponding broadening of the density of states. Accordingly, Fig. 5.8(b) shows that the damping $-\mathrm{Re}z_{C2}$ of the C2 exponentials match very closely the damping parameter $z_s(Q_m)$ of the acoustic spectral lines if Q is taken to be the position Q_m of the maximum in the dispersion curve. This is in agreement with the already stated fact that the density of states is dominated by the sound modes of maximal frequency.

It is worth noting from Fig. 5.8 that the top sound frequency varies with density between reduced values of about 16 and 30, while the corresponding dampings remain constant around

13, indicating that the acoustic excitation becomes less sharply defined in less dense fluids. As a consequence, also sound modes of frequency not much lower than the maximum one in the dispersion curve can contribute partially to the density of states of a fluid: the more so the lower the density. This fact explains why $|\mathrm{Im}z_{C2}|$ becomes smaller than the maximum of $\omega_s(Q)$ when the density is decreased. Analogously, the contribution of lower-frequency sound modes with their respective broadenings make the damping of the C2 modes a bit larger than the damping z_s of the acoustic excitation at the top of the dispersion curve, as shown in Fig. 5.8(b).

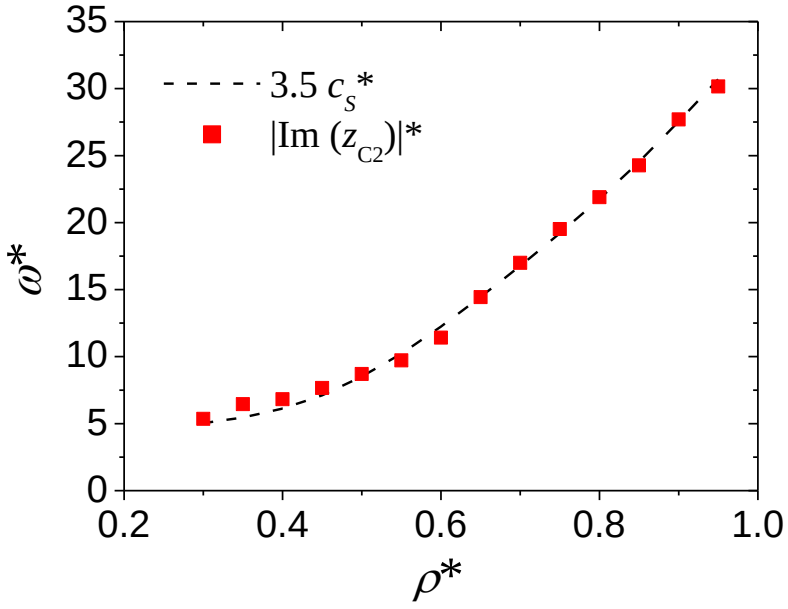

Figure 5.9: Oscillation frequency of the C2 modes (full squares) as a function of density at $T^* = 1.35$ including the low-density states. The dashed line depicts the $3.5c_s^*$ behavior explained in the text.

The strict relation between the oscillation frequency of the C2 modes and the collective longitudinal dynamics can also be visualized in another way. In Fig. 5.9, $|\mathrm{Im}z_{C2}^*|$ is plotted as a function of density, including for completeness the lower density states discussed in Ch. 4. The line is the plot of $3.5c_s^*$, which describes very well the density behavior of the data points. Here 3.5 is only an empirically adjusted number, to which no specific meaning is attached. However, there are reasons to justify this kind of relationship and a numerical factor close to and slightly larger than π. Figure 5.8(a) shows that, for increasing Q^*, the dispersion curves bend upwards (positive dispersion) before reaching their top values, and it is also found that they intersect the hydrodynamic linear dispersion $c_s^*Q^*$ somewhere near the position Q_m^* of the maximum.

Beyond this point, dispersion curves in fluids drop typically a bit faster than they rise to the left of it, up to the value of $Q^* = Q_p^*$, where the static structure factor $S(Q^*)$ displays its main peak. Thus, Q_m^* is usually close to, but slightly greater than, $Q_p^*/2$. On the other hand, in a fluid Q_p^* is close to 2π, therefore the top frequency of the acoustic mode is well approximated by the hydrodynamic dispersion evaluated at $Q^* \gtrsim \pi$, which gives the result displayed in Fig. 5.9.

Though the above is just a semi-quantitative argument, the agreement displayed in Fig. 5.9 is actually remarkable, highlighting a simple but accurate proportionality relation between two properties of the system under study: one, $|\mathrm{Im}z_{C2}|$, derived from the theoretically well-founded exponential mode expansion, the other, c_s, being a fundamental thermophysical quantity of a fluid. The link between these two properties is meaningful independently of possible minor changes of the actual proportionality factor.

To summarize, we have thus definitely established in a quantitative way that the exponential expansion of the VAF allows to extract that part of the density of states which is strictly and directly connected to the propagation of longitudinal sound waves. We remark that, in doing so, we relate the dispersion curves and the VAF spectrum *of the same fluid state*, without using any information on the vibrational density of states of the corresponding crystalline solid. In this respect, these findings conform to the results of the Gaskell and Miller [37, 38] approach that explicitly links $Z(t)$ to the self and collective correlation functions of the one and the same system. However, our method deepens considerably the analysis by providing a way to separate different dynamical processes, opening a route for studying their evolution as functions of any relevant state parameter.

5.3.3 Low-frequency dynamics

So far we have identified the modes of the VAF expansion which are related to the LTT (i.e. R3 and R4) and to the longitudinal collective dynamics (the C2 pair, remembering that the contribution of the C1 pair is by far negligible). We now turn to the remaining modes. As shown in Tab. 5.3, these include the real exponentials R1 and R2 which can be qualified as fast decaying terms. In fact, their decay times are of the order of τ_E (we find $\tau_{R1}/\tau_E = 0.86$ for $\rho^* = 0.65$ and $\tau_{R2}/\tau_E = 3.30$ and 3.48 for $\rho^* = 0.65$ and 0.70, respectively).

However, we noted that optimization of the fit model leads to the elimination of both terms

while introducing a new complex pair C3 already at density $\rho^* = 0.70$. This suggests that we are witnessing a transition from non-propagating to propagating modes, with the transformation of purely decaying term(s) into another oscillatory component of the VAF time dependence. We also noted that at the highest densities a good fit requires an extra real mode (labeled R0) which turns out to have a negative amplitude. Some insights about the origin of this rather peculiar mode will be given in Ch. 7. The interplay between these components of the VAF can be complicated to follow in extreme detail. However, what we were interested in this work was to see how a contribution to the VAF that starts at low density as a sum of diffusive relaxation channels (see par. 4.3) evolves towards an oscillatory behavior, and what kind of dynamics it corresponds to. Thus, we define another group by summing together the exponentials R1, R2, C3, and R0, whenever present. The time function so obtained and its FT are denoted as $Z_T(t)$ and $\hat{Z}_T(\omega)$, respectively.

Both these quantities were displayed in Fig. 5.5, from which a few facts can be immediately noticed. First, $Z_T(t)$ constitutes the largest component of the total VAF at low densities, while providing an intensity comparable to the high-frequency group (C1+C2) at high density. Second, $\hat{Z}_T(\omega)$ shows clearly the presence of a peak at a nonzero frequency for $\rho^* \geq 0.80$. On the other hand, Tab. 5.3 indicates that the C3 complex pair is still missing at $\rho^* = 0.65$ but is present at $\rho^* = 0.70$. Thus a vibrational dynamics seems to set on in the crossover range $0.65 < \rho^* < 0.75$. In Fig. 5.5(b) (i.e. at $\rho^* = 0.70$) one would at first sight conclude that no such vibration frequency is present. However, it's important to note that the spectral signature of a strongly damped oscillation may appear as a single line. Moreover, at $\rho^* = 0.70$ the C3 pair of lines is still added to a central Lorentzian line due the real exponential R2 which can mask partially the spectrum of the oscillating terms. At all densities, however, the frequency of the C3 modes is clearly smaller than that of the high-frequency group, and for this reason we shall refer to these modes as the low-frequency group.

In order to tentatively assign this group of modes to a specific dynamical property of the fluid, we first note that in the Gaskell and Miller approach both longitudinal and transverse dynamics appear, on equal footing, in the integral representation of the VAF [37], but that we have not yet related any fit components of either the VAF or its FT to the dynamics of transverse modes. Moreover, it is known that if excitations in the transverse current autocorrelation

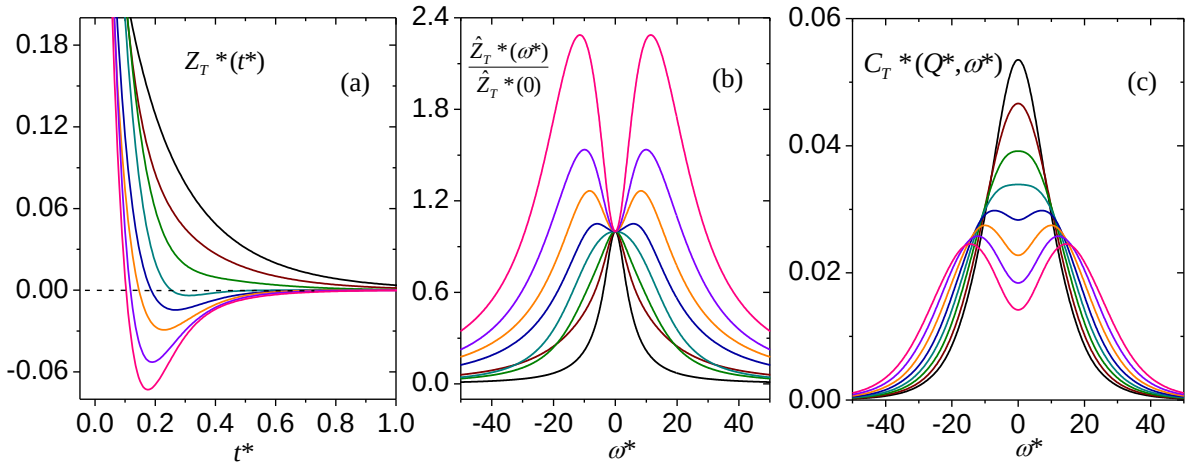

Figure 5.10: (a) Time dependence of $Z_T(t)$, i.e. sum of the fitted exponentials belonging to the low-frequency group. Curves are ordered for increasing density from top ($\rho^* = 0.60$) to bottom ($\rho^* = 0.95$) in steps of 0.05. (b) Frequency spectra of the curves in (a), normalized to their respective zero frequency value. Here lower densities correspond to lower curves (at small frequency). (c) Frequency spectra of the transverse current autocorrelation function at a selected Q^* value (see text) and for the same densities as in (a), (b). Curves are ordered for increasing density from highest to lowest peak height. The color code is the same in all three frames.

function take the form of propagating waves, they do it with lower frequencies than in the longitudinal case [37, 70]. Also, it is a common belief that a low-density fluid does not sustain propagation of shear waves while non-ideal dense liquids do [9, 60, 71]. All these facts point then to a likely connection of the whole low-frequency group of modes to transverse dynamics, and it appears reasonable to check if more quantitative arguments can be put forward to make this relation stand on firm grounds.

Here we go into details of this analysis for the $T^* = 1.35$ states only, but analogous observations can be made for those along the $\rho^* = 0.80$ isochore. The results are summarized in Fig. 5.10, where, for comparison, also the $\rho^* = 0.60$ case have been included. The time dependence of $Z_T(t)$ is shown in Fig. 5.10(a). This quantity begins to feature a negative part for $\rho^* = 0.75$ that progressively deepens and shifts its minimum to lower times. Such a behavior describes the emergence of an oscillation of growing strength and increasing frequency.

It is instructive to compare the plot of $Z_T(t)$ with that of the total VAF shown in Fig. 5.2(a), in two respects. First, the onset of a negative part of $Z(t)$ is also located just above $\rho^* = 0.75$. The near coincidence of this threshold density in $Z(t)$ and $Z_T(t)$ is remarkable, since the former

contains other terms which are absent in the latter. This suggests that the VAF develops its negative part mainly because of the overall oscillating behavior of the low-frequency group (which in turn is mostly due to the C3 complex pair). Second, the next oscillation clearly visible in Fig. 5.2(a) around $t^* = 0.35$ is missing in $Z_T(t)$ and is therefore due to the C2 complex pair.

Going to the frequency domain, $\hat{Z}_T(\omega)$ is plotted in Fig. 5.10(b) after normalization to its zero frequency value. This graphical representation highlights the change in shape brought about by the increase in density: the curve is bell-shaped up to $\rho^* \approx 0.70$ and shows a distinct double peak for $\rho^* \geq 0.80$. At $\rho^* = 0.75$ no peaks are visible but the curve features a flat top that suggests the presence of two strongly overlapping lines, so that this density can again be considered to be a threshold value, in agreement with what has already been discussed.

The connection to transverse dynamics is obtained when Fig. 5.10(c) is considered, where we display the spectrum $C_T(Q, \omega)$ of the transverse current autocorrelation function [9] also obtained from the MD simulations described in the previous paragraph. The curves refer to the various densities and to wavevector Q values ranging from 3.1 to 3.9 (here Q^* varies slightly with density because it was taken to be a fixed multiple of the minimum value accessible in the simulation box). $C_T(Q, \omega)$ and $\hat{Z}_T(\omega)$ are conceptually different quantities that it makes no sense to compare directly. Nevertheless, they are linked by a common underlying set of dynamical processes. Actually, and more precisely, for the same reasons discussed in par. 5.3.2 we can say that the latter represents the density of states related to the Q-dependent collective dynamics described by the former. A meaningful comparison between the spectra in Figs. 5.10(b) and 5.10(c) can be performed at the level of their evolution with density. Doing so, one sees that the overall shape of transverse current spectra and its density dependence follows closely the very similar pattern of $\hat{Z}_T(\omega)$. Again, a flat top at $\rho^* = 0.75$ points at the presence of two peaks not separated because of their width, which become apparent at $\rho^* = 0.80$. The case $\rho^* = 0.70$ cannot be clearly assigned to either the presence or the absence of a propagation by simple visual inspection, and only the fitting of appropriate models to $C_T(Q, \omega)$ can solve the issue. This task is outside the scope of this work, so we limit ourselves to compare in Fig. 5.11 the frequencies of the main spectral features of $\hat{Z}_T(\omega)$ and of $C_T(Q, \omega)$ obtained by estimating both from the positions $\omega_{\max,Z_T}$ and $\omega_{\max,C_T}$ of their respective maxima. Though this is no rigorous

procedure, a clear similarity appears to the sound mode case presented in Fig. 5.8(a).

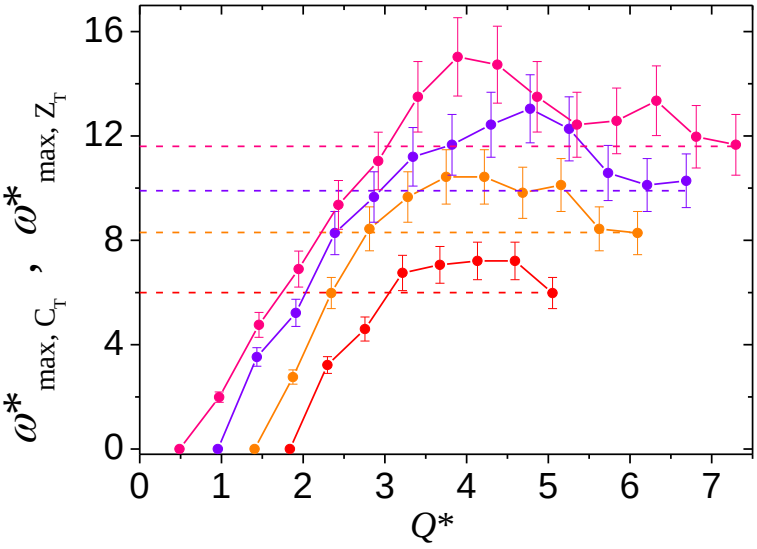

Figure 5.11: The lines joining symbols with error bars are the transverse dispersion curves obtained as the positions of maxima of $C_T(Q,\omega)$. Data for the $T^* = 1.35$ states are shown in order of increasing density from bottom ($\rho^* = 0.80$) to top ($\rho^* = 0.95$). Dashed lines, in the same order, mark the corresponding position of maxima of $\hat{Z}_T(\omega)$.

We have, therefore, obtained clear evidence of the link between the low-frequency mode group, extracted from the exponential expansion of the total $Z(t)$, and the dynamics of transverse collective motions in the fluid, and the subscript T used to denote this component of the total fit model for the VAF does indeed rightly assume the meaning of "transverse".

5.3.4 Dynamical crossover

In the previous paragraph it has been noted how the low-frequency dynamical processes that show up in the exponential mode expansion of the VAF reveal the appearance of a dynamical transition, essentially driven by the transformation of transverse waves from nonpropagating to propagating ones.

A precise determination of the crossover point, besides requiring a very time-consuming finer exploration of the thermodynamic state space, is somewhat hindered by the diversity of criteria that may be applied to define the relevant property. For example, Tab. 5.3 shows that the existence of a low-frequency oscillating component of the VAF is already attained at $\rho^* =$

0.70, which is also the density where the total $Z(t)$ has an inflection point (see Fig. 5.2(a)). Then, the appearance of the inflection point and of the negative part of $Z(t)$ do not occur at exactly the same density. On the other hand, at $\rho^* = 0.70$, besides the oscillatory part, the transverse dynamics contains also a further real mode (R2), and becomes purely oscillatory, though damped, only at $\rho^* = 0.75$. In agreement with that, looking at Fig. 5.10 we have suggested a possible threshold density $\rho^* = 0.75$, though only based on visual inspection.

However, rather than trying to establish a rigid criterion for an exact determination of the crossover density, what matters here is the evidence of a dynamical transition which, for the slightly supercritical states investigated here, can be found at a density which is, broadly speaking, between those of the critical and triple points but closer to the latter. This transition separates lower density fluid states, where the dynamics has a typical gaslike character, from higher density ones where it takes up a more distinctly liquidlike nature.

To clarify this point, it is useful to note that, if $\hat{Z}_{\mathrm{T}}(\omega)$ is characterized by a spectral feature of nonzero frequency, and given its meaning of a partial density of states, this implies the existence of a dispersion curve of propagating (i.e. having nonzero excitation energies) transverse waves. Actually, we can go further by expecting that $\hat{Z}_{\mathrm{T}}(\omega)$ is a spectral distribution centered around the frequency at which the transverse dispersion curve shows a flat Q dependence or attains its top value.

On the other hand, it is well known that a dilute fluid does not support the propagation of shear waves. In quantitative terms, this means that no strictly positive frequency can be introduced, and no dispersion curve can be defined. Accordingly, the whole transverse dynamics reduces to the superposition of diffusive motions and no oscillatory behavior appears in autocorrelation functions (or parts thereof, as in the case of the VAF) related to transversal motions.

Another important point is that propagation of acoustic modes, either longitudinal or transverse, depends not only on the thermodynamic properties of the fluid but also on the wavevector values, a fact critically relevant, in particular, for the transverse excitations. Indeed, it is customarily stated that a dense fluid can sustain transverse waves but only for wavevectors above a certain value [10], in agreement with the fact that in the hydrodynamic limit $Q \to 0$ the transverse current autocorrelation spectrum has the Lorentzian shape typical of diffusive processes [9] without any nonzero-frequency excitations, and this result holds true even for dense liquids.

ρ^*	T^*	C1+C2	C3+R0+R1+R2	R3+R4
0.65	1.35	26.3	52.5	21.3
0.70	1.35	26.9	51.8	21.3
0.75	1.35	24.7	54.5	20.7
0.80	1.35	35.8	47.3	16.9
0.85	1.35	43.4	44.1	12.4
0.90	1.35	37.7	54.4	7.8
0.95	1.35	49.8	42.4	7.9
0.80	1.35	35.8	47.3	16.9
0.80	1.20	38.1	46.8	15.0
0.80	1.10	39.5	47.6	13.0
0.80	1.00	41.2	48.9	9.8
0.80	0.90	42.6	48.9	8.6

Table 5.4: Percent contribution to the integral of the VAF of the fitted modes grouped as indicated. The numbers in each row add up to 100 percent to within rounding of the last digit.

It follows that a transverse dispersion curve can be defined only for Q larger than the minimum required. Therefore, the crossover we are dealing with is the transition between the situation where no transverse modes propagate at any Q, and the one in which they propagate at least in some Q range. Consideration of only one of the two relevant variables (Q,ρ) will only allow for an incomplete account of the transverse dynamics. An evidence of this fact is provided by Fig. 5.11, where the transverse dispersion curve for a lower density state begins at a larger Q value. Analogous results have been very recently obtained in another study of LJ dynamics [72].

As recalled in par. 5.1, the issue of a separation between two different regions of the thermodynamic space of a supercritical fluid, marked by a crossover boundary, has been a largely debated topic in the last years [57, 58, 60, 61]. Following seminal insight and theoretical developments of Frenkel [73], the crossover Frenkel line has been identified through the occurrence of specific properties, actually not all coinciding as far as the line position in the pressure-temperature plane is concerned. Among such properties are the onset of propagation of transverse waves, the emergence of positive dispersion in the propagation of longitudinal sound modes, and the temperature dependence of the constant-volume specific heat per atom crossing the value $c_V = 2k_B$. Another criterion for the definition of the Frenkel line specifically involves

a property of the VAF, as it is formulated by assuming the crossover to occur when the VAF shape begins to display a relative minimum and a relative maximum instead of a monotonic decay [61]. As seen in par. 5.3.3, we obtain a very similar localization of our crossover condition. However, it should be remarked that the discussion about boundary lines in the fluid phase diagram has been mostly concerned with the transition induced by changing temperature and pressure in wide ranges, including consideration of highly supercritical fluid states at very large pressures. In contrast, we have obtained evidence of a crossover driven by the density alone in isothermal conditions at temperatures just above the critical point.

As a final remark, it is useful to assess the relative importance of the three fundamental processes discussed so far (in pars. 5.3.1, 5.3.2 and 5.3.3) as represented by their partial contributions to the total time-integrated VAF, reported in Tab. 5.4 as percent fractions, for all thermodynamic states. It is shown that the LTT contribution is the smallest one, being confined to the long-time range where the VAF intensity decreases to very low values. The high frequency modes related to the sound propagation show a clear trend, growing in importance with both increasing density and decreasing temperature. Finally, the low frequency processes related to the transverse dynamics account for about half of the total VAF integral with no significant variation with the thermodynamic coordinates. This is interesting, because it evidences that the strength of the modes involved in the crossover does not show any abrupt change across the transition boundary.

Chapter 6

Velocity autocorrelation function of a quantum fluid

After the analysis of the VAF of a classical Lennard-Jones fluid, we found it interesting to study the VAF of a semi-quantum system in order to explore possible differences and analogies with a classical model fluid. Para-hydrogen, p-H_2, was perfectly suited to the scope because not only it represents an interesting fluid to study by itself, but also it is a fluid where quantum exchange effects play a negligible role, so that Boltzmann statistics still holds true. As a consequence, its dynamics can be simulated by means of approximated techniques like the *path-integral* method described in the next paragraph. In order to make a meaningful comparison with the VAF of the LJ fluid, we chose to simulate thermodynamic states approximately correspondent to that reported in previous chapters for the LJ fluid, i.e. slightly supercritical constant-T states with densities ranging from that of the critical point up to a density just above that of the triple point. However, since these simulations were very time consuming to reach a reasonable accuracy, it was not possible to carry out, within this thesis work, a complete analysis of the results. A more exhaustive analysis is therefore left to future research.

6.1 Path-integral simulations

The path integral formulation of quantum mechanics [74], which represents a mathematically-equivalent alternative to the Heisenberg and Schrödinger pictures, has been a fruitful source of

simulation techniques for the study of condensed matter properties. In particular, the Path Integral Monte Carlo (PIMC) and Path Integral Molecular Dynamics (PIMD) methods can be used to compute the exact static equilibrium properties of quantum systems, while the Centroid Molecular Dynamics (CMD) and Ring Polymer Molecular Dynamics (RPMD) methods can be used to represent, in an approximate way, the real-time dynamics of such systems.

The starting point to derive the path integral formulation of statistical mechanics is the relation between the canonical partition function $Z_{NVT}(\beta)$ of a quantum system consisting of N particles at temperature T in a volume V, and the density operator $\hat{\rho} = \exp[-\beta\hat{H}]$ (with $\hat{H}$ the Hamiltonian of the system):

$$Z_{NVT}(\beta) = \int \mathrm{d}\vec{\mathbf{r}}\, \hat{\rho}(\vec{\mathbf{r}}, \vec{\mathbf{r}}; \beta), \tag{6.1}$$

where $\hat{\rho}(\vec{\mathbf{r}}, \vec{\mathbf{r}}; \beta)$ is the coordinate representation of the trace of $\hat{\rho}$

$$\hat{\rho}(\vec{\mathbf{r}}, \vec{\mathbf{r}}; \beta) = \langle \vec{\mathbf{r}}|\hat{\rho}|\vec{\mathbf{r}}\rangle = \langle \vec{\mathbf{r}}|\mathrm{e}^{-\beta\hat{H}}|\vec{\mathbf{r}}\rangle \tag{6.2}$$

and $\vec{\mathbf{r}}$ denotes the set of positions all particles. For the sake of simplicity, we will start considering a system made of only one particle, whose position is indicated by $\mathbf{r}$. Then, the result will be easily extended to a many-particle system.

In quantum mechanics, the Hamiltonian $\hat{H}$ is the sum of two operators, the kinetic energy $\hat{K}(\mathbf{p})$ and potential energy $\hat{U}(\mathbf{r})$, that do not commute with each other. Consequently, the density operator $\exp[-\beta\hat{H}]$ in Eq. (6.2) cannot be evaluated straightforwardly. Nevertheless, the Trotter theorem [35] can be exploited to express it as

$$\mathrm{e}^{-\beta(\hat{K}+\hat{U})} = \lim_{P\to\infty} \left[\mathrm{e}^{-\beta\hat{U}/2P}\mathrm{e}^{-\beta\hat{K}/P}\mathrm{e}^{-\beta\hat{U}/2P}\right]^P. \tag{6.3}$$

Substituting Eq. (6.3) into Eq. (6.2) yields

$$\hat{\rho}(\mathbf{r}, \mathbf{r}; \beta) = \lim_{P\to\infty} \langle \mathbf{r}| \left[\mathrm{e}^{-\beta\hat{U}/2P}\mathrm{e}^{-\beta\hat{K}/P}\mathrm{e}^{-\beta\hat{U}/2P}\right]^P |\mathbf{r}\rangle \equiv \lim_{P\to\infty} \langle \mathbf{r}|\hat{\Omega}^P|\mathbf{r}\rangle, \tag{6.4}$$

which also defines the operator $\hat{\Omega}$. Inserting the identity operator, $\hat{I} = \int \mathrm{d}\mathbf{r}\, |\mathbf{r}\rangle\langle\mathbf{r}|$, $P-1$ times in Eq. (6.4), one obtains

$$\hat{\rho}(\mathbf{r}, \mathbf{r}; \beta) = \lim_{P\to\infty} \int \mathrm{d}\mathbf{r}_2 \cdots \mathrm{d}\mathbf{r}_P\, \langle \mathbf{r}|\hat{\Omega}|\mathbf{r}_P\rangle\langle \mathbf{r}_P|\hat{\Omega}|\mathbf{r}_{P-1}\rangle\langle \mathbf{r}_{P-1}| \cdots |\mathbf{r}_2\rangle\langle \mathbf{r}_2|\hat{\Omega}|\mathbf{r}\rangle, \tag{6.5}$$

where each matrix element in Eq. (6.5) can be evaluated in closed form. Indeed, exploiting the fact that $|\mathbf{r}\rangle$ and $|\mathbf{p}\rangle$ are eigenvectors of $\hat{U}$ and $\hat{K}$ respectively, and using again the identity

operator $\hat{I} = \int \mathrm{d}\mathbf{p}\, |\mathbf{p}\rangle\langle\mathbf{p}|$, the generic matrix element in Eq. (6.5) becomes

$$\begin{aligned}
\langle \mathbf{r}_{k+1}|\hat{\Omega}|\mathbf{r}_k\rangle &= \mathrm{e}^{-\frac{\beta}{2P}[U(\mathbf{r}_{k+1})+U(\mathbf{r}_k)]}\langle \mathbf{r}_{k+1}|\mathrm{e}^{-\beta\hat{K}/P}|\mathbf{r}_k\rangle \\
&= \mathrm{e}^{-\frac{\beta}{2P}[U(\mathbf{r}_{k+1})+U(\mathbf{r}_k)]}\int \mathrm{d}\mathbf{p}\, \langle \mathbf{r}_{k+1}|\mathrm{e}^{-\beta\hat{K}/P}|\mathbf{p}\rangle\langle\mathbf{p}|\mathbf{r}_k\rangle \\
&= \mathrm{e}^{-\frac{\beta}{2P}[U(\mathbf{r}_{k+1})+U(\mathbf{r}_k)]}\int \mathrm{d}\mathbf{p}\, \langle \mathbf{r}_{k+1}|\mathbf{p}\rangle\langle\mathbf{p}|\mathbf{r}_k\rangle \mathrm{e}^{-\beta p^2/(2mP)} \\
&= \mathrm{e}^{-\frac{\beta}{2P}[U(\mathbf{r}_{k+1})+U(\mathbf{r}_k)]}\frac{1}{(2\pi\hbar)^3}\int \mathrm{d}\mathbf{p}\, \mathrm{e}^{-\beta p^2/(2mP)}\mathrm{e}^{i\mathbf{p}\cdot(\mathbf{r}_{k+1}-\mathbf{r}_k)/\hbar}
\end{aligned} \tag{6.6}$$

where the coordinate representation of the state $|\mathbf{p}\rangle$, $\langle\mathbf{r}|\mathbf{p}\rangle = \dfrac{1}{(2\pi\hbar)^{3/2}}\mathrm{e}^{i\mathbf{p}\cdot(\mathbf{r}_{k+1}-\mathbf{r}_k)/\hbar}$, has been adopted. The integral in the last line of Eq. (6.6) is a typical Gaussian integral that can be calculated to give

$$\langle \mathbf{r}_{k+1}|\mathrm{e}^{-\beta\hat{K}/P}|\mathbf{r}_k\rangle = \left(\frac{mP}{2\pi\beta\hbar^2}\right)^{3/2}\exp\left[-\frac{mP}{2\beta\hbar^2}(\mathbf{r}_{k+1}-\mathbf{r}_k)^2\right]. \tag{6.7}$$

Finally, exploiting the results of Eqs. (6.7) and (6.6), one arrives at the following discretized path integral representation of the trace of the density operator $\hat{\rho}$:

$$\begin{aligned}
\hat{\rho}(\mathbf{r},\mathbf{r};\beta) = \lim_{P\to\infty}\left(\frac{mP}{2\pi\beta\hbar^2}\right)^{3P/2}\int \mathrm{d}\mathbf{r}_2\cdots\mathrm{d}\mathbf{r}_P \\
\exp\left\{-\frac{1}{\hbar}\sum_{k=1}^{P}\left[\frac{mP}{2\beta\hbar}(\mathbf{r}_{k+1}-\mathbf{r}_k)^2+\frac{\beta\hbar}{P}U(\mathbf{r}_k)\right]\right\}
\end{aligned} \tag{6.8}$$

with the condition that $\mathbf{r}_{P+1} = \mathbf{r}_1$. As a consequence, the one-particle canonical partition function $Z_{1VT}(\beta)$ in Eq. (6.1) reads

$$\begin{aligned}
Z_{1VT}(\beta) = \lim_{P\to\infty}\left(\frac{mP}{2\pi\beta\hbar^2}\right)^{3P/2}\int \mathrm{d}\mathbf{r}_1\mathrm{d}\mathbf{r}_2\cdots\mathrm{d}\mathbf{r}_P \\
\left.\exp\left\{-\frac{1}{\hbar}\sum_{k=1}^{P}\left[\frac{mP}{2\beta\hbar}(\mathbf{r}_{k+1}-\mathbf{r}_k)^2+\frac{\beta\hbar}{P}U(\mathbf{r}_k)\right]\right\}\right|_{\mathbf{r}_{P+1}=\mathbf{r}_1}.
\end{aligned} \tag{6.9}$$

Generalizing the previous equation to a system of N quantum Boltzmann particles, and defining the frequency $\omega_P \equiv \sqrt{P}/(\beta\hbar)$, one obtains the following result:

$$\begin{aligned}
Z_{NVT}(\beta) = \lim_{P\to\infty}\frac{1}{N!}\left(\frac{mP}{2\pi\beta\hbar^2}\right)^{3NP/2}\int \mathrm{d}\mathbf{r}_1^{(1)}\cdots\mathrm{d}\mathbf{r}_j^{(k)}\cdots\mathrm{d}\mathbf{r}_N^{(P)} \\
\left.\exp\left\{-\beta\sum_{k=1}^{P}\left[\sum_{j=1}^{N}\left(\frac{1}{2}m\omega_P^2(\mathbf{r}_j^{(k+1)}-\mathbf{r}_j^{(k)})^2\right)+\frac{1}{P}U(\mathbf{r}_1^{(k)},\ldots,\mathbf{r}_N^{(k)})\right]\right\}\right|_{\mathbf{r}_j^{(P+1)}=\mathbf{r}_j^{(1)}} \\
\equiv \lim_{P\to\infty}\frac{1}{N!}\left(\frac{mP}{2\pi\beta\hbar^2}\right)^{3NP/2}\int \mathrm{d}\mathbf{r}_1^{(1)}\cdots\mathrm{d}\mathbf{r}_j^{(k)}\cdots\mathrm{d}\mathbf{r}_N^{(P)}\exp[-\beta(U^{cl}+U^{qu})]
\end{aligned} \tag{6.10}$$

where the argument of the exponential has been expressed as a sum of a classical potential term

$$U^{cl} = \frac{1}{P}\sum_{k=1}^{P} U(\mathbf{r}_1^{(k)}, \ldots, \mathbf{r}_N^{(k)}) \tag{6.11}$$

and a quantum potential term

$$U^{qu} = \sum_{j=1}^{N}\sum_{k=1}^{P} \frac{1}{2} m\omega_P^2 (\mathbf{r}_j^{(k+1)} - \mathbf{r}_j^{(k)})^2 \quad \text{with} \quad \mathbf{r}_j^{(P+1)} = \mathbf{r}_j^{(1)}. \tag{6.12}$$

Fixing the Trotter number P, the partition function in Eq. (6.10) clearly resembles that of a classical system consisting of N cyclic polymer chains, each made up of P particles. Thus, Eq. (6.10) evidences how it is possible to map the original quantum system into an approximated (since P is finite) classical one. This property, called *classical isomorphism* [75], is the basis of all path integral algorithms used to simulate equilibrium properties of quantum many-body systems.

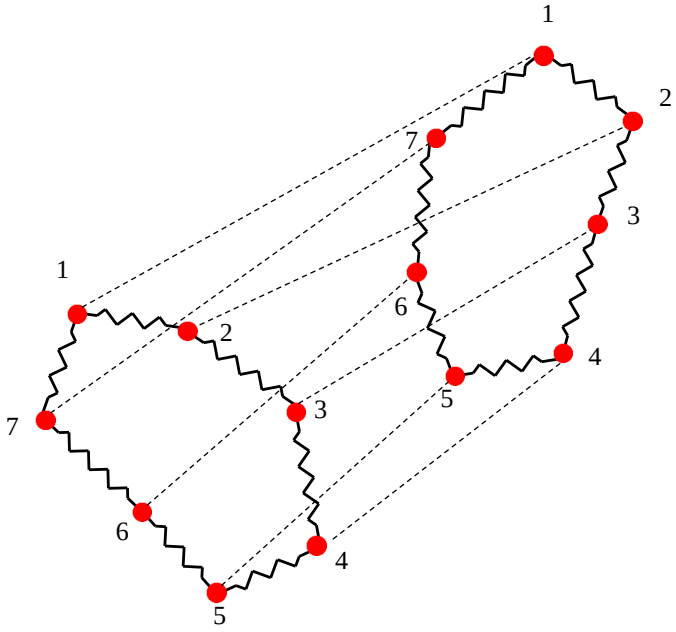

Figure 6.1: Interaction pattern between two quantum particles represented as ring-polymers. The dashed lines are the intermolecular potential interactions, while the zigzag line indicate the intramolecular spring potential.

As shown in Fig. 6.1, each quantum particle in a path integral simulation is actually represented by an ensemble of P identical particles in the form of a ring-polymer "molecule". Since the polymer resembles the form of a necklace, its P particles are often referred to as "beads".

Each bead is coupled with its nearest-neighbors through a harmonic spring potential having a characteristic frequency given by ω_P and an equilibrium length equal to zero. According to the definition of ω_P, the stiffness of the springs is proportional to the temperature T so that, as T increases, all the beads tend to concentrate in a progressively smaller region. In particular, if $T \to \infty$ the polymer reduces to a point as appropriate for a classical system. As this fact suggests, what the ring polymer actually stands for is the delocalization of the quantum particle. Indeed, when P is set to one, the classical expression of the partition function is restored. Moreover, as depicted in Fig. 6.1, the interactions between different molecules only involve correspondingly numbered beads, that is, bead 1 of a given molecule only sees bead 1 of the other molecules, and so on.

Once the classical isomorphism has been established, a standard Monte Carlo (MC) simulation applied to the classical ring-polymer system, with a potential energy given by $U^{cl} + U^{qu}$, can be used to explore the configurational space of the quantum system. This is exactly the idea at the basis of the PIMC method. Although, in principle, the canonical ensemble could be sampled using just a simple Metropolis algorithm [76] applied to the entire NP-particles system, in practice, this approach turns out to be quite inefficient [35]. Indeed, more reliable PIMC calculations are performed by treating separately the intra- and the inter-polymer sampling. In particular, standard Metropolis moves are applied only to the center of masse (CM) of the polymers, while the internal canonical distribution is obtained directly by taking advantage of a normal modes transformation of the polymer cyclic chain. Indeed, if one expresses the double sum $\sum_{k,j} \frac{1}{2} m\omega_P^2 (\mathbf{r}_j^{(k+1)} - \mathbf{r}_j^{(k)})^2$ as a single sum over uncoupled, independent harmonic oscillators, then the quantum term $\exp(-\beta U^{qu})$ in Eq. (6.10) can be written as a product of $P-1$ Gaussian functions [35]

$$\prod_{k=2}^{P} \exp(-u_k^2/(2\sigma_k^2)), \tag{6.13}$$

where u_k are normal-modes coordinates and

$$\sigma_k^2 = \frac{\hbar^2 \beta}{2m\rho} \frac{1}{\left(1 - \cos\frac{2\pi(k-1)}{P}\right)}. \tag{6.14}$$

Therefore, using, for example, the Box-Muller method [36] to generate Gaussian-distributed random numbers and making the transformation from u_k coordinates to chain coordinates [35], one can easily sample the polymer configurations.

The expression of the energy of a quantum system is obtained via the calculation of the derivative of Eq. (6.10) with respect to β as stated by the following thermodynamic relation:

$$\langle E \rangle = -\frac{\partial}{\partial \beta} \ln Z_{NVT}(\beta) = -\frac{1}{Z_{NVT}} \frac{\partial Z_{NVT}(\beta)}{\partial \beta}. \tag{6.15}$$

and the result is

$$\langle E \rangle = \lim_{P \to \infty} \left[\langle K \rangle_{cl} - \langle U^{qu} \rangle + \langle U^{cl} \rangle \right] \tag{6.16}$$

which allows to define a quantum kinetic energy $\langle K \rangle$ as the difference of a classical term $\langle K \rangle_{cl} = \frac{3}{2} N P k_{\mathrm{B}} T$, consequence of the equipartition theorem, and a purely quantum term $\langle U^{qu} \rangle$, i.e.

$$\langle K \rangle = \lim_{P \to \infty} \left[\langle K \rangle_{cl} - \langle U^{qu} \rangle \right]. \tag{6.17}$$

In a similar way, the expression of the pressure is obtained via the relation

$$\langle P \rangle = k_B T \frac{\partial}{\partial V} \ln Z_{NVT}(V) = \frac{k_B T}{Z_{NVT}} \frac{\partial Z_{NVT}(V)}{\partial V}, \tag{6.18}$$

with the result

$$\langle P \rangle = \lim_{P \to \infty} \left\{ \frac{2}{3} \frac{N}{V} \frac{\langle K \rangle}{N} - \frac{1}{3V} \left\langle \frac{1}{P} \sum_{j=1}^{N} \sum_{k=1}^{P} \mathbf{r}_j^{(k)} \cdot \frac{\partial U}{\partial \mathbf{r}_j^{(k)}} \right\rangle \right\}, \tag{6.19}$$

that is just the quantum analogue of the virial theorem already reported in Eq. (3.5).

In a PIMC simulation, thermal averages of various thermodynamic functions, like the aforementioned energy and pressure, are readily computed by making an average of the values these functions assume in each sampled microscopic configuration. Structural distribution functions can be computed as well. The pair correlation function $g(r)$, for example, only requires to calculate the mean fraction of particles that are a given distance r apart, with the important specification that only distances between correspondingly numbered beads have to be taken into account.

The path integral formulation of quantum mechanics has proved very useful and effective also to approximate quantum time correlation functions [77, 78, 79, 80, 81]. In particular, the CMD and RPMD approximation schemes, having the advantage of being relatively inexpensive to implement, have been largely employed in the field of condensed-phase systems. However, in the following, only the RPMD simulation technique will be discussed.

It is possible to demonstrate that if one recasts the prefactor in Eq. (6.10) as a set of Gaussian integrals over momentum $\mathbf{p}_j^{(k)}$ variables [35], and if the physical mass m is attributed to each

bead of the polymer [79], then the partition function (for finite P) can be written as

$$Z_P = \frac{1}{(2\pi\hbar)^{3NP}} \int\int \prod_{k=1}^{P}\prod_{j=1}^{N} \mathrm{d}\mathbf{p}_j^{(k)}\,\mathrm{d}\mathbf{r}_j^{(k)}\, \exp\left[-\frac{\beta}{P} H_P(\{\mathbf{p}_j^{(k)}\},\{\mathbf{r}_j^{(k)}\})\right] \tag{6.20}$$

where

$$H_P = \sum_{k=1}^{P}\sum_{j=1}^{N}\left[\frac{(\mathbf{p}_j^{(k)})^2}{2m} + \frac{1}{2}mP\omega_P^2(\mathbf{r}_j^{(k+1)} - \mathbf{r}_j^{(k)})^2 + U(\mathbf{r}_1^{(k)},\ldots,\mathbf{r}_N^{(k)})\right] \tag{6.21}$$

is the Hamiltonian of the system of P harmonic ring polymers that interact through the physical potential $U(\mathbf{r}_1^{(k)},\ldots,\mathbf{r}_N^{(k)})$. The basic assumption of the RPMD method is that the classical Newtonian equations of motion generated by this Hamiltonian can be used to make the system evolve in time:

$$\begin{aligned} \frac{\mathrm{d}\mathbf{p}_j^{(k)}}{\mathrm{d}t} &= -mP\omega_P^2(2\,\mathbf{r}_j^{(k)} - \mathbf{r}_j^{(k-1)} - \mathbf{r}_j^{(k+1)}) - \frac{\partial U(\mathbf{r}_1^{(k)},\ldots,\mathbf{r}_N^{(k)})}{\partial \mathbf{r}_j^{(k)}} \\ \frac{\mathrm{d}\mathbf{r}_j^{(k)}}{\mathrm{d}t} &= \frac{\mathbf{p}_j^{(k)}}{m} \end{aligned} \tag{6.22}$$

Given a trajectory of the system in the phase space, the time autocorrelation function of a position-dependent observable A is obtained as

$$\langle A_P(0)A_P(t)\rangle = \left\langle \left(\frac{1}{P}\sum_{k=1}^{P} A(\mathbf{r}_1^{(k)}(0),\ldots,\mathbf{r}_N^{(k)}(0))\right)\left(\frac{1}{P}\sum_{k=1}^{P} A(\mathbf{r}_1^{(k)}(t),\ldots,\mathbf{r}_N^{(k)}(t))\right)\right\rangle, \tag{6.23}$$

where the average is intended over different time origins as already stated in Eq. (3.13).

Equation (6.23) does not constitute an approximation of the standard quantum time autocorrelation function defined by

$$C_{AA}(t) = \langle \hat{A}(0)\hat{A}(t)\rangle = \frac{1}{Z}\mathrm{Tr}\left[\mathrm{e}^{-\beta\hat{H}}\,\hat{A}\,\mathrm{e}^{i\hat{H}t/\hbar}\,\hat{A}\,\mathrm{e}^{-i\hat{H}t/\hbar}\right], \tag{6.24}$$

where the Heisenberg representation is used to express $\hat{A}(t)$, but rather of the Kubo-transformed autocorrelation function [82]

$$K_{AA}(t) = \frac{1}{\beta Z}\int_0^\beta \mathrm{d}\lambda\,\mathrm{Tr}\left[\mathrm{e}^{-(\beta-\lambda)\hat{H}}\,\hat{A}\,\mathrm{e}^{-\lambda\hat{H}}\,\mathrm{e}^{i\hat{H}t/\hbar}\,\hat{A}\,\mathrm{e}^{-i\hat{H}t/\hbar}\right]. \tag{6.25}$$

Although this fact cannot be proved on a theoretical basis, there are some arguments that evidence how it can be considered a reasonable assumption [79]. First, Eq. (6.25) is a real and even function of time as happens for the correlation in Eq. (6.23). Second, the $t = 0$ value of Eq.

(6.23) does not approximate the quantum average $C_{AA}(0) = \langle \hat{A}^2 \rangle$, but rather the $t = 0$ value of the Kubo correlation $K_{AA}(0)$ [82]. Third, Eq. (6.23) gives the exact quantum mechanical result $K_{AA}(t)$ for all t in the limit of a harmonic potential, at least in the special case of operators $\hat{A}$ that are linear functions of the position operator.

Denoting by $\hat{C}_{AA}(\omega)$ and $\hat{K}_{AA}(\omega)$ the Fourier transform of Eqs. (6.24) and (6.25) respectively, it is easy to derive the following relation:

$$\hat{C}_{AA}(\omega) = \frac{\beta\hbar\omega}{1 - \mathrm{e}^{-\beta\hbar\omega}} \hat{K}_{AA}(\omega), \tag{6.26}$$

which is just a generalization of Eq. (2.6) to any time autocorrelation function. Equation (6.26) is remarkable since it evidences a possible way to obtain, via a double Fourier transformation (direct and inverse), an approximation of the standard quantum correlation $C_{AA}(t)$ starting from an RPMD approximation of $K_{AA}(t)$. For example, taking the particle velocity $\mathbf{v}$ as the dynamical variable $\hat{A}$ and making an average over the N particles, Eq. (6.24) reads

$$C_{\mathbf{vv}}(t) = \frac{1}{ZN} \sum_{j=1}^{N} \mathrm{Tr} \left[\mathrm{e}^{-\beta\hat{H}}\, \hat{\mathbf{v}}_j\, \mathrm{e}^{i\hat{H}t/\hbar}\, \hat{\mathbf{v}}_j\, \mathrm{e}^{-i\hat{H}t/\hbar} \right], \tag{6.27}$$

with a $t = 0$ value that is proportional to the mean quantum kinetic energy:

$$C_{\mathbf{vv}}(0) = \frac{2}{m} \langle K \rangle. \tag{6.28}$$

The $t = 0$ value of the Kubo autocorrelation, Eq. (6.25), is instead give by [82]

$$K_{\mathbf{vv}}(0) = \frac{2}{m} \langle K \rangle_{cl} = \frac{3k_{\mathrm{B}}T}{m}. \tag{6.29}$$

We will see in par. 6.3 that the real kinetic energy of a system, i.e. its quantum value $\langle K \rangle$, is always greater than the corresponding classical value $\langle K \rangle_{cl}$.

An RPMD approximation of $\langle K \rangle$ can be established via Eq. (6.26) in the following way:

$$\langle K \rangle = \frac{m}{2} C_{\mathbf{vv}}(0) = \frac{m}{4\pi} \int_{-\infty}^{\infty} \mathrm{d}\omega \int_{-\infty}^{\infty} \mathrm{d}t\, \frac{\beta\hbar\omega}{(1 - e^{-\beta\hbar\omega})} e^{-i\omega t} \langle \mathbf{v}_P(0) \cdot \mathbf{v}_P(t) \rangle\,. \tag{6.30}$$

Equation (6.30) evidences that $\langle K \rangle$ depends on the behavior of $\langle \mathbf{v}_P(0) \cdot \mathbf{v}_P(t) \rangle$ at all times, suggesting that it can be used as an important consistency check of the RPMD method. Indeed, the value of $\langle K \rangle$ obtained from Eq. (6.30) can be compared with the exact value obtained from a PIMC calculation.

As a final remark, it is worth stressing that the RPMD method, as well as any other method that neglects quantum mechanical interference effects in real-time dynamics, is not guaranteed to give accurate results for times greater than $\beta\hbar$ [83]. However, the situation is less dramatic than it may seem, because quantum phase effects in condensed matter systems are often suppressed due to pronounced decoherence effects [35]. So, when applying the RPMD method to fluid-state studies, also results that involve time lags greater than $\beta\hbar$ can be considered trustworthy.

6.2 Simulations of a supercritical p-H_2 fluid

Obtaining RPMD simulation results of reasonable accuracy is a rather time demanding task. The main reason is simply the fact that the interactions between all N particles have to be computed P times, that is for each bead of the polymer, and this makes the computational cost to scale approximately as the product NP, which can be very large indeed. Fortunately, Alessandro Torcini (ISC-CNR, Florence) kindly offered us the possibility of exploiting part of his PC farm in order to speed up our calculations.

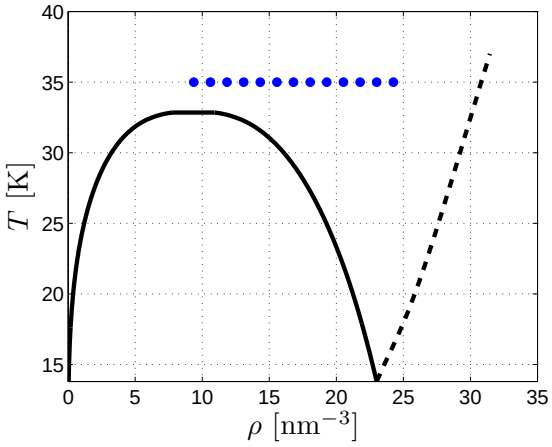

Figure 6.2: Simulated p-H_2 states (blue dots) in the (ρ,T) plane. The liquid-vapor coexistence boundary (solid line from Ref. [86]) is reported along with the melting line (dashed line from Ref. [84]).

The simulations have been carried out for states belonging to the $T = 35$ K isotherm, just above the critical isotherm $T = 32.94$ K, as reported in Fig. 6.2. The densities were chosen equally spaced between the critical density $\rho_c = 9.37$ nm^{-3} and a value, $\rho = 24.05$ nm^{-3}, just

above the density of the triple point $\rho_t = 23.01$ nm^{-3}. For all states, a box containing 864 ring-polymers, each of 32 beads, was used. To model the interactions between particles, we adopted

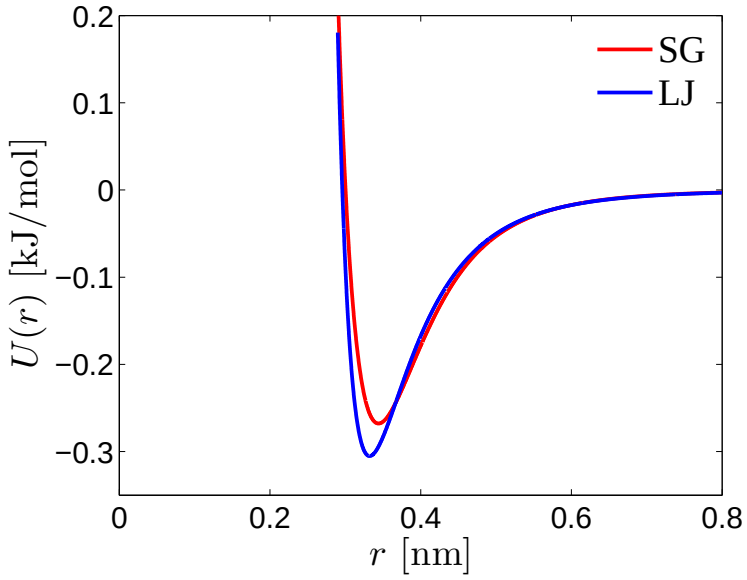

Figure 6.3: Silvera-Goldman (SG) pair potential from Eq. (6.31) and Lennard-Jones pair potential from Eq. (3.3), with ϵ and σ p-H_2 parameters obtained from Tab. 2.3 of Ref. [8].

the Silvera-Goldman (SG) pair potential [85]

$$U(r) = \mathrm{e}^{\alpha-\beta r-\gamma r^2} - \left(\frac{C_6}{r^6} + \frac{C_8}{r^8} - \frac{C_9}{r^9} + \frac{C_{10}}{r^{10}}\right) f_0(r) \tag{6.31}$$

with

$$f_0(r) = \begin{cases} \mathrm{e}^{-(r_0/r-1)^2} & \text{if } r \leq r_0 \\ 1 & \text{otherwise} \end{cases} \tag{6.32}$$

which gives a good description of p-H_2 in its spherically symmetric $J = 0$ ground state. All parameters in Eqs. (6.31) and (6.32) are reported in Ref. [85]. The shape of the SG potential is shown in Fig. 6.3 together with the LJ potential for comparison.

As in LJ simulations, the Gaussian thermostat described in Ch. 3 has been employed to maintain the system at the required temperature T. In particular, N thermostats, one for each polymer, were set at the temperature PT required by the polymer internal dynamics, as shown by the term β/P in Eq. (6.20), while a different global thermostat at temperature T was used to constrain the translational dynamics of the entire system. The equations of motion (6.22) have

been integrated through the two-step leapfrog algorithm reported in Eq. (3.6) with a time-step $\Delta t = 0.001$ ps, and the tabulation of forces method described in Ch. 3 was used to speed up the calculation. At each thermodynamic state, the velocity autocorrelation function (VAF)

$$Z_K(t) = \frac{1}{N}\sum_{j=1}^{N}\left\langle\left(\frac{1}{P}\sum_{k=1}^{P}\mathbf{v}_j^{(k)}(0)\right)\cdot\left(\frac{1}{P}\sum_{k=1}^{P}\mathbf{v}_j^{(k)}(t)\right)\right\rangle \tag{6.33}$$

was computed on a grid with spacing $5\Delta t$ from zero up to a maximum time lag of $t = 20$ ps, averaging over 10 independent runs of 10^6 time-steps each. The subscript K in Eq. (6.33) stands for Kubo, for the reasons given in the previous paragraph.

Since RPMD simulations are surely not a routine technique in the field of fluids dynamics, it was necessary to make some preliminary tests in order to become familiar with the method and so, finally, to generate simulations appropriate for our purposes. For example, we started making some short simulations with the aim of understanding which was the more appropriate time-step to be used. Firstly, we tried a value of 0.005 ps as in Ref. [83], but we noticed that, with this choice of dt, the integration algorithm was clearly unstable, maybe because of the higher temperature of our states with respect to those of Ref. [83]. On the other hand, we found that a time-step of 0.001 ps was perfectly suited, while a lower value had only the disadvantage of lengthening the duration of the simulation.

Another fundamental issue regarded the choice of the Trotter number P, having in mind that, as explained in par. 6.1, a value of P equal to 1 corresponds to a classical simulation, while, in the limit $P \to \infty$, a quantum mechanical picture is achieved. For this purpose, we carried out a series of PIMC simulations of a system at one of our thermodynamic states ($T = 35$ K, $\rho = 19.29$ nm^{-3}) with 864 polymers and with Trotter numbers ranging from 1 to 64 as powers of 2. For each P, we performed a run of $2 \cdot 10^4$ steps with a polymer displacement parameter of 0.15 nm, so that an average moves-acceptance-ratio of about 0.39 was produced. From the configurations so obtained, we calculated mean values of: i) the kinetic energy K, calculated as in Eq. (6.17), ii) the potential energy U, and iii) the radius of gyration of the polymer, defined as

$$\sqrt{r^2} = \frac{1}{NP}\sum_{j=1}^{N}\sum_{k=1}^{P}|\mathbf{r}_j^{(k)} - \mathbf{r}_j^c|^2, \tag{6.34}$$

with $\mathbf{r}_j^c$ the position of the centroid of polymer j. All these averages are displayed in Fig. 6.4 as a function of the inverse of P. This is a quite useful representation, because the quantum limit

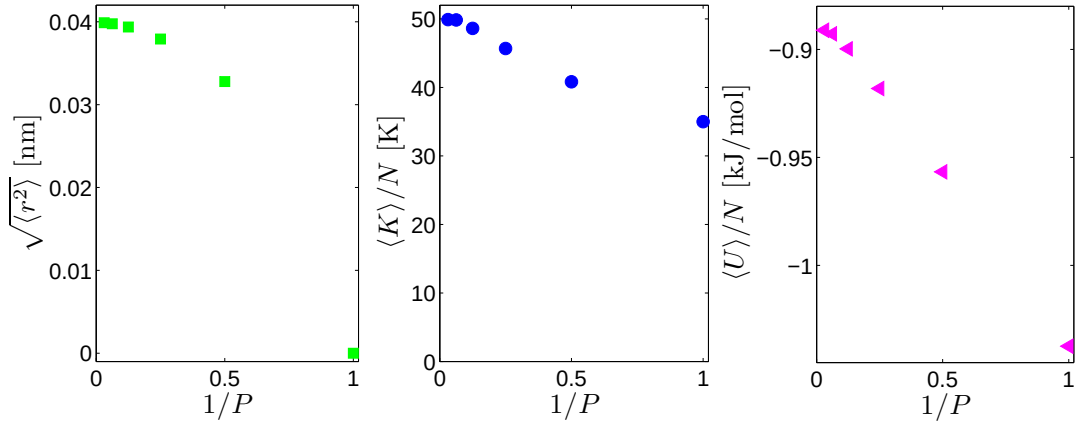

Figure 6.4: PIMC calculation of the p-H_2 averages of: radius of gyration of the polymer $\sqrt{r^2}$, kinetic energy K and potential energy U. All parameters are plotted as functions of $1/P$. The simulated state is the one at $T = 35$ K and $\rho = 19.29$ nm^{-3}. The system consists of $N = 864$ polymers, each of 32 beads.

can be easily visualized as the intercept of each curve with the vertical axis. For all parameters, Fig. 6.4 clearly shows that, when $P = 32$, the lines tangent to the curves are almost horizontal. This means that, for such a value of P, the quantum limit is already almost reached.

A deeper insight on the modification the system undergoes with varying the Trotter number can be achieved also by looking at Fig. 6.5, where the pair distribution function $g(r)$ is reported for each value of P. Moving from the classical system ($P = 1$) to the quantum limit one can observe that: i) the peaks of the function become less pronounced and ii) the main peak shifts towards higher distances. The picture that emerges from such a behavior is that of a system whose particles, going towards the quantum limit, increase their mean separation and, in a sense, become softer. For P values greater than 8, all curves appear to be stack one over the other, so that, again, we can affirm that a value of 32 is largely sufficient to represent the true quantum situation.

From a dynamical point of view, a quite similar picture is accomplished by looking at Fig. 6.6, where RPMD calculations of the normalized VAF of just 108 polymers are displayed for some values of P. It is evident from the figure that changing the value of P above $P = 2$ does not affect the shape of the VAF very much. Indeed, the curves corresponding to $P = 16$ and $P = 32$ are practically coincident on the scale of the figure.

As already observed in pars. 4.2 and 5.2, the recurrence time $t_R = (N/\rho)^{1/3}/c_s$ that occurs

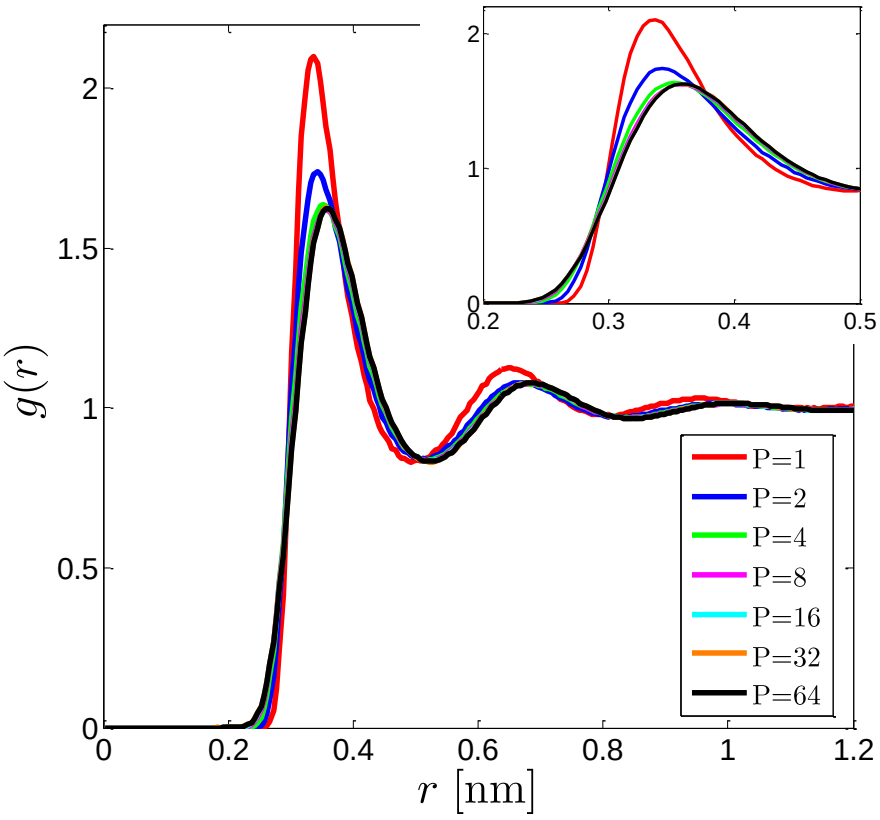

Figure 6.5: PIMC calculation of the p-H_2 pair distribution function $g(r)$ at the P values reported in the legend. The simulated state is the one at $T = 35$ K and $\rho = 19.29$ nm^{-3}, with a system made of 864 particles. The inset shows a zoom of the main peak, to better appreciate its modification varying P.

in a simulation box must be carefully considered if one focuses in the study of the long-time behavior of a time correlation function, as the VAF in our case. It is actually a main purpose of this part of the thesis to find differences and analogies between the VAF of a classical LJ fluid and the VAF of a quantum fluid like p-H_2, with reference also to its long-time behavior. Therefore, since t_R scales as $N^{1/3}$, the choice of the number of particles to be used in the simulation is of crucial importance to obtain recurrence times large enough to permit a reliable detection of a (possibly present) long-time tail. Some preliminary simulations were indeed necessary to observe the effects brought about by an increasing number of particles in the box on the shape of the VAF. As an example, Fig. 6.7 reports the normalized VAF corresponding to $T = 35$ K and $\rho = \rho_c$ for five different values of N and with $P = 32$. Supposing that a $t^{-3/2}$ power-law dependence is indeed an effective way to represent the behavior of the VAF at large times, Fig.

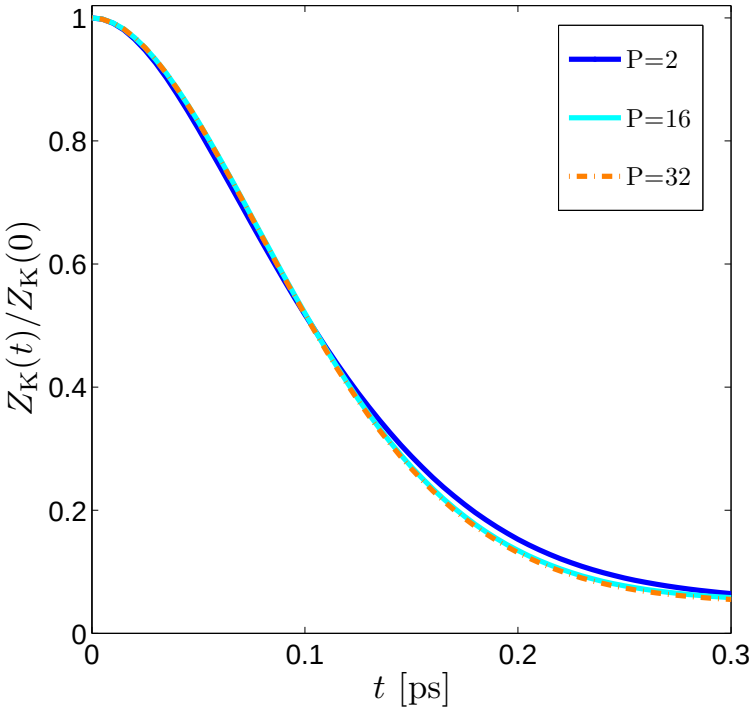

Figure 6.6: RPMD calculation of the p-H_2 normalized VAF at the P values reported in the legend. The system consists of 108 particles and is in the thermodynamic state (T = 35 K, ρ = 19.29 nm^{-3}).

6.7 shows that the recurrence effects produce distortions in the VAF quite before the LTT has set on. Actually, the situation improves as N increases, so that, when $N = 864$, the recurrence time t_R, equal to 10.5 ps, seems to be big enough to permit the detection of, at least, the initial part of the LTT. Thus, we concluded that a possible long-time tail could be observed, and analyzed, only taking $N = 864$. Obviously, simulating a bigger system would be even better, but we didn't have a sufficient computing power to do that in a reasonable time.

Another important issue has been the determination of the time necessary to the system to equilibrate. A possible method to establish how long to perform the equilibration run of a simulation is that of calculating running averages of some dynamical variables that characterize the system and monitoring their trend over time. The equilibration period should be extended at least until these quantities have ceased to show a systematic drift and have started to fluctuate around steady values [36]. Figure 6.8 reports the running averages of kinetic energy, potential energy, pressure and radius of gyration of the polymer. The thermodynamic state used for this test is the one with the lowest density, that is ρ_c = 9.37 nm^{-3}, which, requiring a longer time

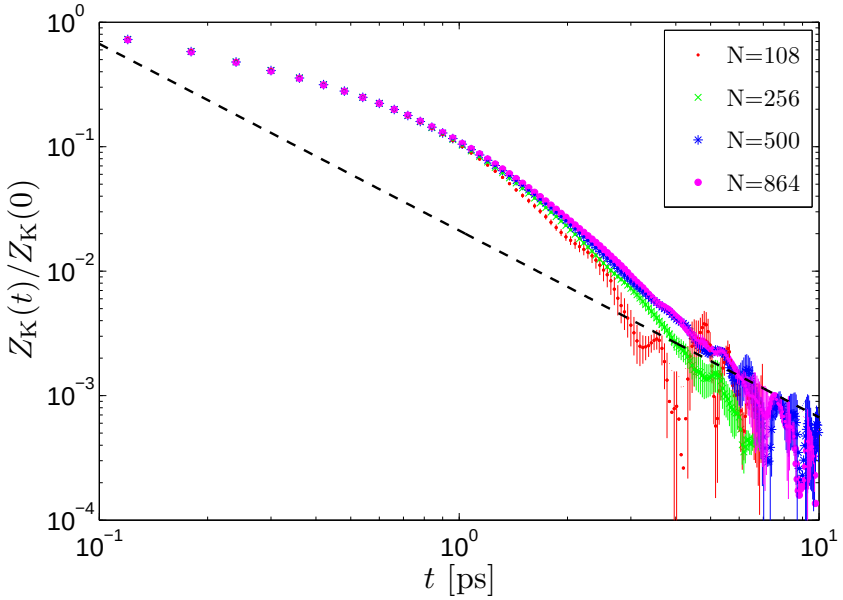

Figure 6.7: RPMD calculation of the p-H_2 normalized VAF at the N values reported in the legend. The simulated state is the one at $T = 35$ K and $\rho = 19.29$ nm^{-3}, and the polymers consists of 32 beads. Each curve is the result of an average over just three runs of $5 \cdot 10^5$ time-steps each. The black dashed line represents a power-law of the form $At^{-3/2}$, with A calculated from Eq. (4.2) using the viscosity coefficient reported in Ref. [86] and the diffusion coefficient obtained from the VAF through Eq. (2.23).

to equilibrate with respect to the other higher-density ones, fixes an upper limit to the duration of the equilibration phase. Fig. 6.8 clearly suggests that this phase takes a time of about 1 ns to come to completion. This is quite a long time if compared to the value of 0.1 ns reported in Ref. [83] for p-H_2 at $T = 25$ K and $\rho = 23.5$ nm^{-3}, because we are considering here a state at a much lower density.

6.3 Discussion of the results

By means of Eq. (6.30), the value of the average quantum kinetic energy $\langle K \rangle$ of the system has been calculated for each density, and the result is reported in Fig. 6.9 in Kelvin units (after division by 3/2 k_B). One can immediately observe that $\langle K \rangle$ is higher than the correspondent classical value, given by 35 K in this units, because of the polymer springs contribution of Eq. (6.12). Moreover, $\langle K \rangle$ monotonically increases with density, reaching a value which is approximately 1.7 times bigger than the classical value. This behavior indicates that, moving towards

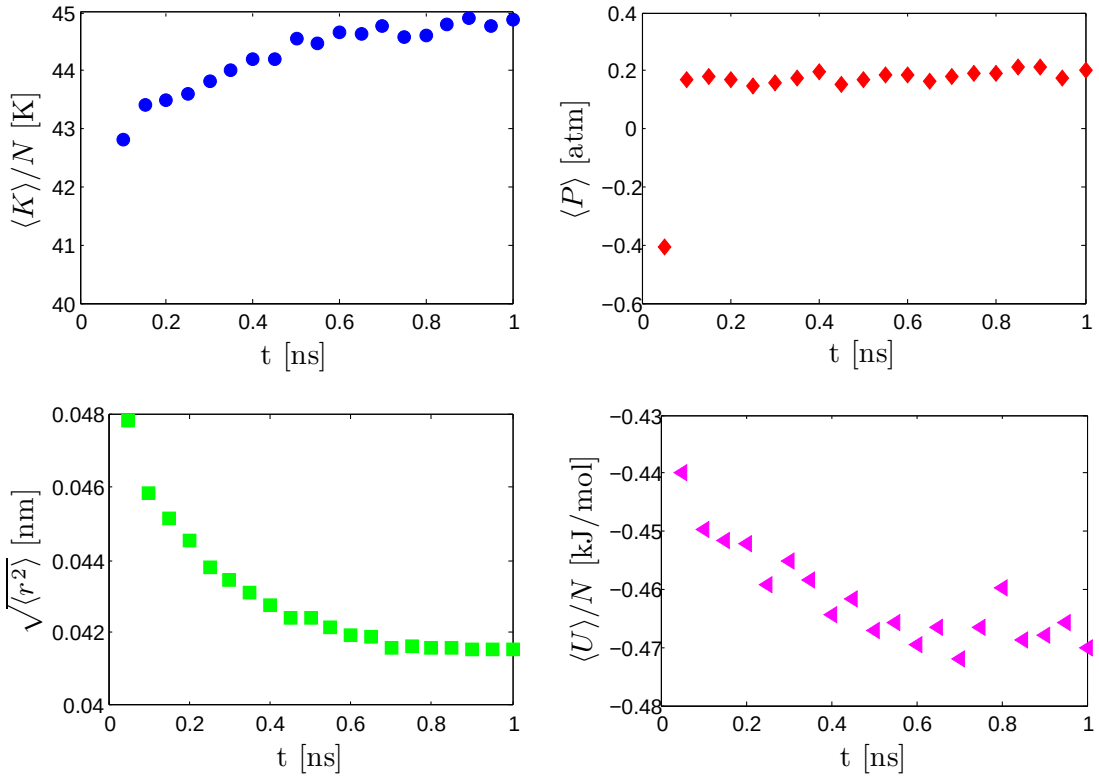

Figure 6.8: Running averages over time intervals of 50 ps of: kinetic energy, potential energy, pressure and radius of gyration of the polymer, calculated during a simulation of p-H_2 at $T = 35$ K and $\rho = \rho_c$. The system consists of 864 polymers each of 32 beads. In their initial configuration the polymers were placed at the vertices of a face-centered-cubic lattice.

higher density, quantum effects play an increasingly important role in the characterization of the system. This is in agreement with the Heisenberg uncertainty principle: as the density grows the volume available for the spatial wave function decreases and this gives rise to significant fluctuations in momentum space, reflected by an increase of the mean kinetic energy. In the right panel of Fig. 6.9, the average extension of the polymers, given by Eq. (6.34), is also displayed as a function of density. In particular we observe that $\langle r^2\rangle^{1/2}$ slightly decreases with density, ranging from a value of about 0.041 nm, at the lowest density, to a value which is 4% smaller at the highest density. So, density variations do not alter $\langle r^2\rangle^{1/2}$ in such a significant way as the temperature does. Indeed, in Ref. [83] the authors found that, passing from $T = 25$ K to $T = 14$ K at $\rho = 20$ nm^{-3}, the radius of gyration of the polymer changed from 0.047 nm to a value 19% bigger.

As already noticed in the previous paragraph, the mean extension of the polymer gives a

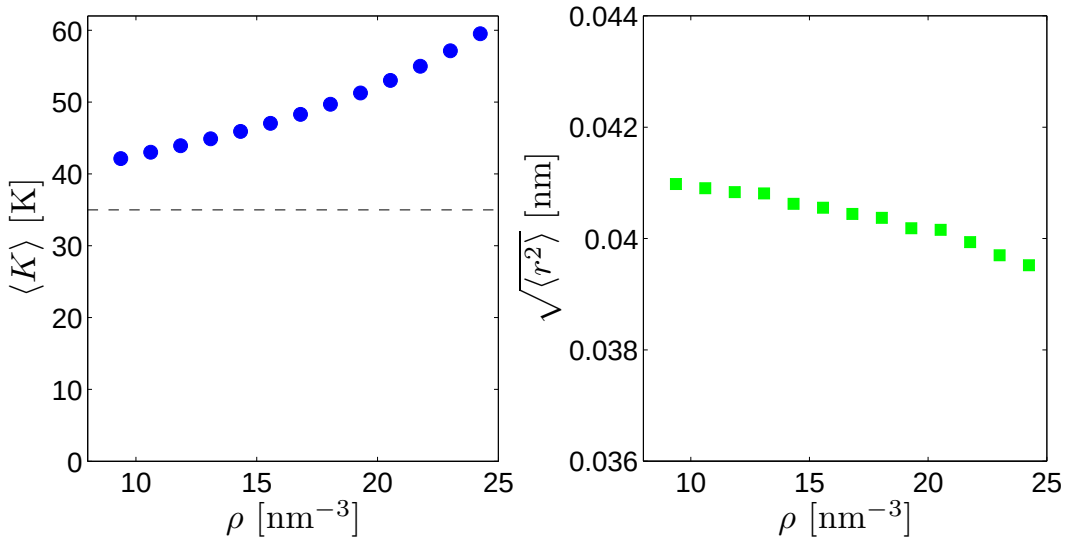

Figure 6.9: (Left panel) Quantum kinetic energy of p-H_2 from Eq. (6.30), in Kelvin units, as a function of ρ. The dashed line at 35 K indicates the classical value of the reduced kinetic energy. (Right panel) Radius of gyration of the polymer calculated from Eq. (6.34) as a function of ρ.

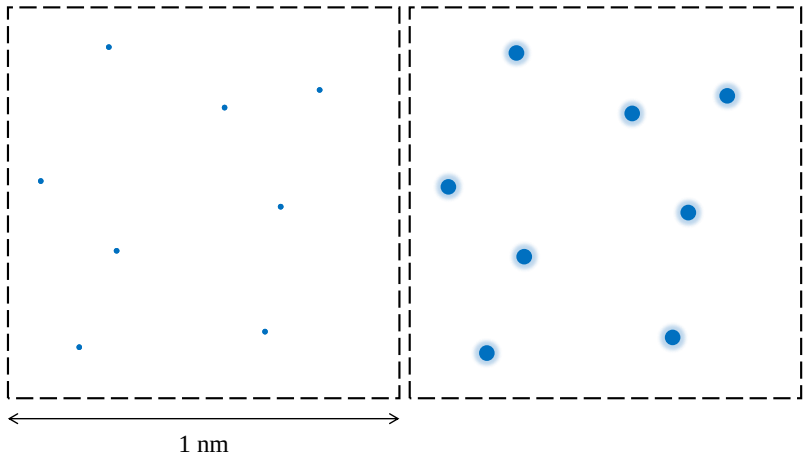

Figure 6.10: Two-dimensional sketch of the delocalization effect. (Left panel) Classical situation: positions are known exactly. (Right panel) Quantum situation: the finite dimension of the ring polymers reflects on an uncertainty of particle positions. The dimension of the circles is of 0.040 nm if the box edge is taken to be 1 nm.

measure of the quantum delocalization effect on a particle of the system. In the classical limit all beads in the polymer contract to a single point ($\langle r^2 \rangle^{1/2} = 0$) so that the position of the real particle represented by the polymer is known exactly. In the quantum case, instead, the finite extension of the polymer plays the role of an uncertainty in the position of the real particle.

This fact is pictorially reported in Fig. 6.10, where the left panel refers to the classical situation while the right panel to the quantum one. The picture is on scale, in the sense that the diameter of the circles in the right panel is indeed 0.040 nm (a mean value from Fig. 6.9) if the box edge is taken to be 1 nm in length.

The long-time behavior of the VAF $Z_K(t)$ is displayed, for all densities, in Fig. 6.11, where the log-log scale is used for an easy comparison with the power-law $At^{-3/2}$ time dependence. To calculate A, Eq. (4.2) was applied, with viscosity coefficients η taken from Ref. [86] and self diffusion coefficients calculated from our $Z_K(t)$ data using the Kubo relation of Eq. (2.23). The values of D_s and η are also reported in Tab. 6.1. Figure 6.11 also shows, with vertical bars, the recurrence time t_R calculated using sound speed data reported in Tab. 6.1 and taken from Ref. [86] as well. For time lags greater than $\sim t_R$, the recurrence problems show up in the VAF with a spurious overall reduction of its intensity and the appearance of a rapidly increasing noisy behavior.

ρ [nm^{-3}]	9.37	10.61	11.85	13.09	14.33	15.57	16.81	18.05	19.29	20.53	21.77	23.01	24.25
T [K]	35	35	35	35	35	35	35	35	35	35	35	35	35
c_s [nm/ps]	0.43	0.45	0.49	0.56	0.64	0.75	0.87	1.00	1.14	1.28	1.41	1.55	1.69
t_R [ps]	10.5	9.6	8.5	7.3	6.1	5.1	4.3	3.6	3.1	2.7	2.4	2.2	1.9
D_s [nm^2/ps]	0.064	0.055	0.048	0.042	0.037	0.033	0.029	0.025	0.022	0.019	0.017	0.014	0.012
$10^5\eta$ [Pa·s]	0.36	0.40	0.44	0.49	0.55	0.61	0.70	0.80	0.92	1.07	1.27	1.52	1.83
10^2A [ps$^{3/2}$]	2.12	2.06	2.00	1.90	1.78	1.65	1.50	1.34	1.17	0.99	0.82	0.67	0.53

Table 6.1: Recurrence time for the simulations and properties of the p-H_2 states on the $T = 35$ isotherm. The adiabatic sound velocity c_s and the viscosity η are taken from Ref. [86]. The diffusion coefficient is calculated through Eq. (2.23) by integrating our Kubo-transformed VAF $Z_K(t)$. The coefficient of the $At^{-3/2}$ power law is obtained through Eq. (4.2).

The picture that emerges from Fig. 6.11 is a rather interesting one and, at the same time, a complex one, with respect to the corresponding Figs. 4.2, 5.3 and 5.4. In particular, for the low-density states a $t^{-3/2}$ tail can never be assessed because the VAF seems to intersect, rather than approaching, the straight line representing the power law. Moving towards higher densities, approximately between $\rho = 16.81$ nm^{-3} and $\rho = 21.77$ nm^{-3}, the power law is indeed an effective representation of the mean trend of the VAF tail in a reasonably extended time range,

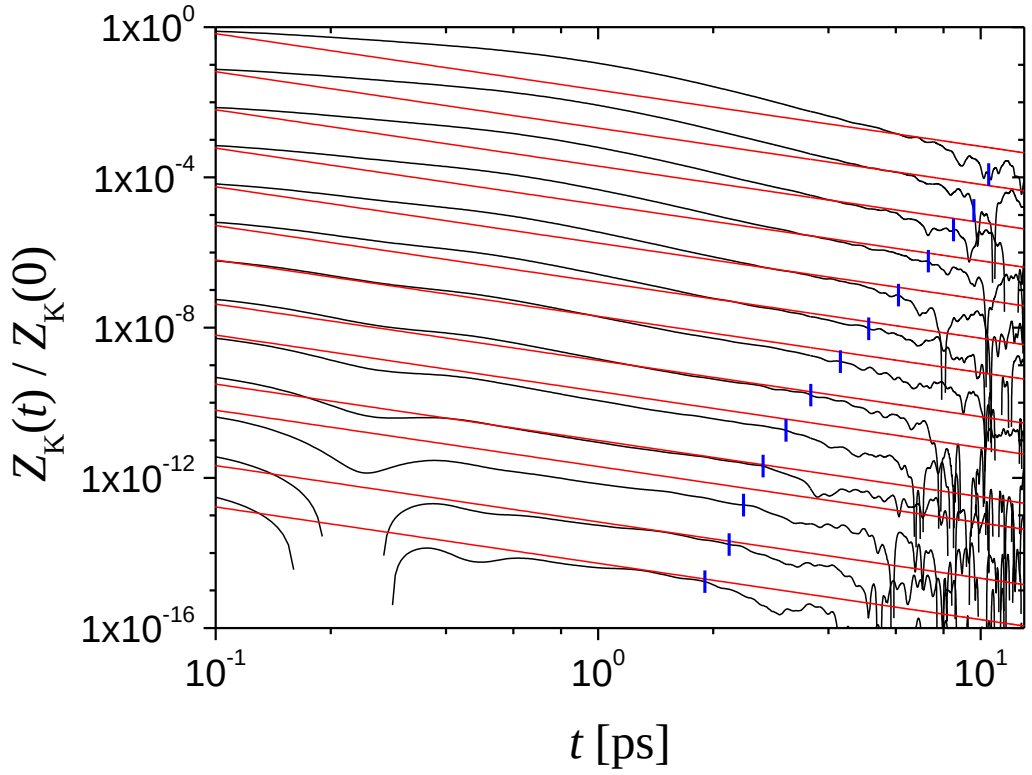

Figure 6.11: Log-log plots of the normalized $Z_K(t)$ from simulation (black solid line) at $t \geq 0.1$ ps for the states along the $T = 35$ K isotherm. The $t^{-3/2}$ behavior (red straight lines) is calculated with the theoretical values of the coefficient A reported in Tab. 6.1. Curves are plotted in order of increasing density from top ($\rho = 9.37$ nm^{-3}) to bottom ($\rho = 24.25$ nm^{-3}) with intermediate values reported in Tab. 6.1, and for clarity each curve is shifted downwards by a factor of 10 with respect to the preceding one. The vertical blue bars mark the values of t_R reported in Tab. 6.1.

even if at some densities, $\rho = 19.29$ nm^{-3} and $\rho = 21.77$ nm^{-3}, the calculated amplitude A is such that the power law never overlaps the VAF. For the higher density states the value of t_R is too small and spurious effects come in well before a long-time tail has set on. Thus, we can affirm that, at least for our low density states, the power-law $At^{-3/2}$ functionality fails to reproduce the long-time behavior of the VAF of this system.

For all thermodynamic states considered here, the left panel of Fig. 6.12 shows the $Z_K(t)$ for times smaller than 1 ps. Having in mind the results of the classical LJ fluid (see par. 5.2), the picture is rather familiar. Starting from a monotonous decay of $Z_K(t)$, the increase of density leads to the appearance of a plateau which rapidly evolves into a relative minimum. This already happens when $Z_K(t)$ still remains everywhere positive, but with a further density increase this

minimum deepens, shifts to smaller times and finally crosses the time axis to become negative. The spectra of $Z_K(t)$ are reported in the right panel of Fig. 6.12. As in the classical LJ case, the little tip around $\omega = 0$, still present at high density, is the sign of the presence of a long-time tail. However, a clear difference with respect to the LJ case is that, even at the highest density, $\hat{Z}_K(\omega)$ doesn't have a dip around $\omega = 0$ which instead appears, for example, in the spectrum of Fig. 5.5(f). However, at the highest density the spectrum flattens considerably around $\omega = 0$.

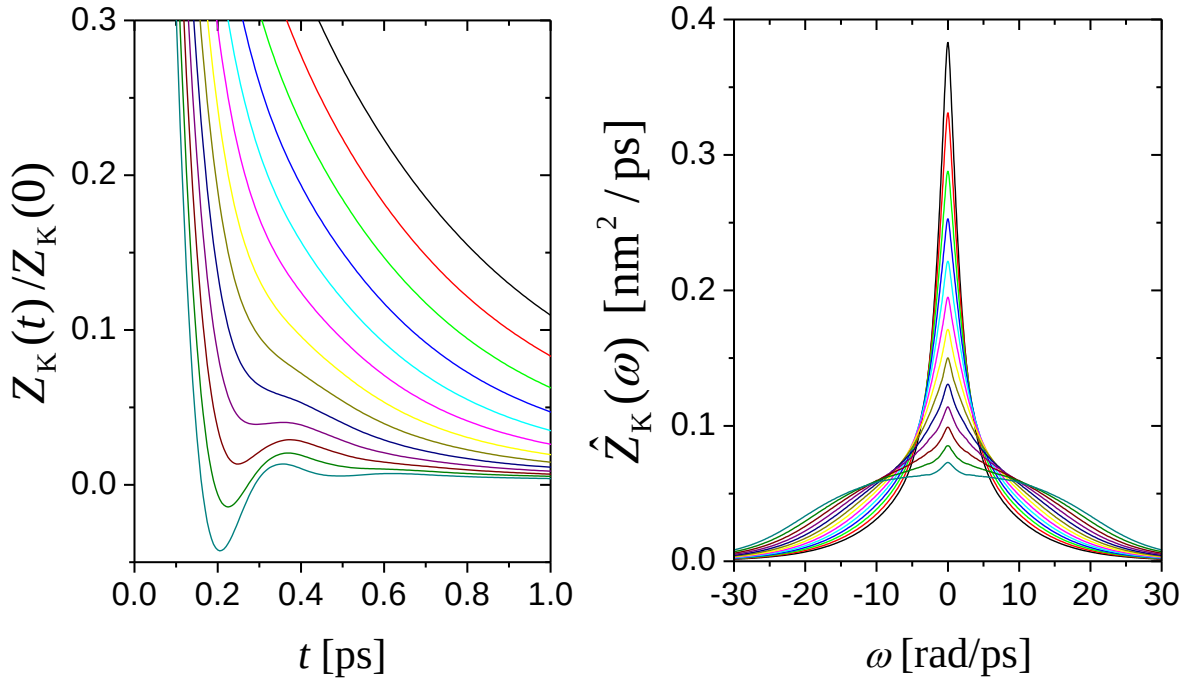

Figure 6.12: (Left panel) Plot of the normalized $Z_K(t)$ from simulation at $t \leq 0.1$ ps for the states along the $T = 35$ K isotherm. Curves are plotted in order of increasing density from top ($\rho = 9.37$ nm^{-3}) to bottom ($\rho = 24.25$ nm^{-3}) with intermediate values reported in Tab. 6.1. (Right panel) Spectra of the non-normalized $Z_K(t)$.

More insight can be gained by looking at Fig. 6.13, where the normalized VAF's of quantum p-H_2 and classical LJ are compared. For such a comparison, the time axis of the p-H_2 VAF have been made dimensionless with a proper combination of the p-H_2 LJ-parameters reported in Tab. 2.3 of Ref. [8]. Figure 6.13 shows the interesting fact that the density trend of the quantum system (left panel) somehow "lags behind" the density trend of the classical LJ system (right panel). For example, at the triple point density ($\rho^* = 0.85$ for LJ and $\rho = 23$ nm^{-3} for p-H_2) the VAF of the classical LJ system exhibits a rather deep and pronounced negative minimum, while the VAF of the quantum p-H_2 system has just become negative and has an overall trend which

is much more similar to the VAF of the LJ at lower density, somewhere between $\rho^* = 0.75$ and $\rho^* = 0.80$. This behavior can be seen as the dynamical counterpart of a structural property previously commented by looking at the pair distribution function of Fig. 6.5. Indeed, when passing from a classical description to a quantum one, the system behaves as if it were less structured and so, in some sense, softer. So, it is reasonable to expect that this characteristic also influences the dynamics in such a way that the quantum system resembles a classical system at some lower density. Moreover, it can be noted that the position of the minimum in the VAF is shifted towards higher times in the case of the quantum p-H_2. This fact is explained by Fig. 6.3, which shows that the LJ potential well is slightly deeper than the Silvera-Goldman one, a fact that again indicates that particles are "looser" than in the LJ case where cohesion is greater. As a consequence, the value of the second derivative in the minimum of the potential is higher in the LJ case, thus giving rise to a bigger second frequency moment Ω_0^2 of the VAF according to Eq. (2.14). However, Ω_0^2 is the opposite of the second time derivative of the VAF in the origin (see Eq. (2.19)) so that higher values of Ω_0^2 correspond to a faster initial decay of the function and, consequently, to an early appearance of the first minimum of the VAF in the LJ case.

Summarizing these observations with those of Ch. 5 all seems to suggest that in p-H_2 close to the triple point density, shear wave propagation only feebly starts to set on, as witnessed by Figs. 6.12 and 6.13, as it happens for the classical LJ fluid farther from its triple point density.

Through Eq. (6.26) it is possible to obtain an approximation of the true quantum VAF $Z_{qu}(t)$ of the system defined in Eq. (6.24). Figure 6.14 reports, as an example, the results obtained for the real part of $Z_{qu}(t)$ at four different densities, and compare them with the corresponding Kubo-transformed VAF $Z_K(t)$. In the left panels, where the short-time behavior is displayed, we note that $Z_{qu}(t)$ is systematically higher than $Z_K(t)$ in $t = 0$. This happens because, as stated by Eq. (6.28), the $t = 0$ value of $Z_{qu}(t)$ approximates the true quantum mean squared velocity of the system (the imaginary part of $Z_{qu}(t)$ in $t = 0$ is zero), while the $t = 0$ value of $Z_K(t)$ gives just its classical result $\langle v^2 \rangle = 3k_B T/m$, independently from the density. In fact, the values of $Z_{qu}(0)$ are the ones used to calculate the quantum kinetic energy reported in Fig. 6.9 for the various densities. For the state at $\rho = 19.29\ \mathrm{nm}^{-3}$ we also performed a PIMC calculation of the quantum kinetic energy as a consistency check of the RPMD method. The result, shown with a dot at $t = 0$ in Fig. 6.14(e), is found to perfectly agree with the zero value of $Z_{qu}(t)$, thus confirming

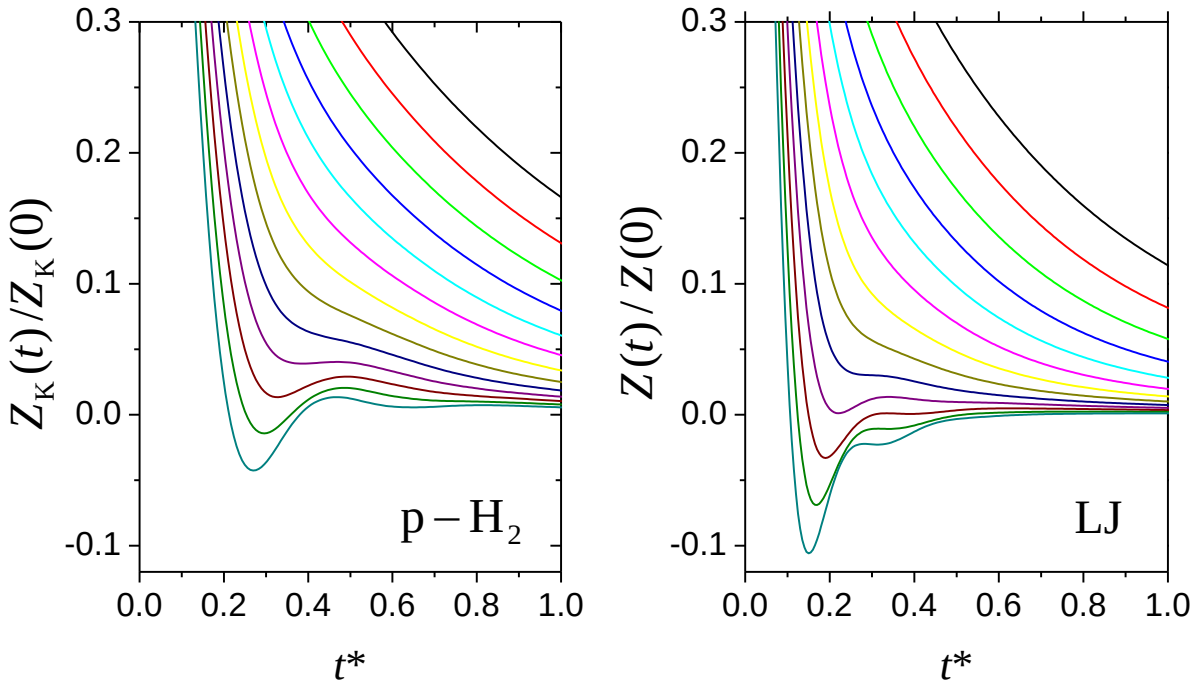

Figure 6.13: (Left panel) Plot of the normalized $Z_K(t)$ at $t^* \leq 0.1$ for the states along the $T = 35$ K isotherm as in Fig. 6.12. Time values are made dimensionless by means of p-H_2 LJ parameters reported in Tab. 2.3 of Ref. [8]. (Right panel) Plot of the normalized $Z(t)$ at $t^* \leq 0.1$ of the LJ fluid at $T^* = 1.35$ discussed in Chs. 4 and 5. Curves are plotted in order of increasing density from top ($\rho^* = 0.30$) to bottom ($\rho^* = 0.90$) at steps of 0.05.

the reliability of our RPMD calculations.

Moreover, looking at the right panels of Fig. 6.14, where the long-time trend of $\mathrm{Re}(Z_{qu}(t))$ and $Z_K(t)$ is shown, we observe that the two functions have the same $t \to \infty$ behavior. Although this is a mere consequence of the fact that the factor which relates $\hat{C}_{AA}(\omega)$ to $\hat{K}_{AA}(\omega)$ in Eq. (6.26) tends to one when $\omega \to 0$, the implications are quite interesting. That is, all the considerations about the LTT in the Kubo-transformed VAF can be extended perfectly to the case of the true quantum VAF of the system.

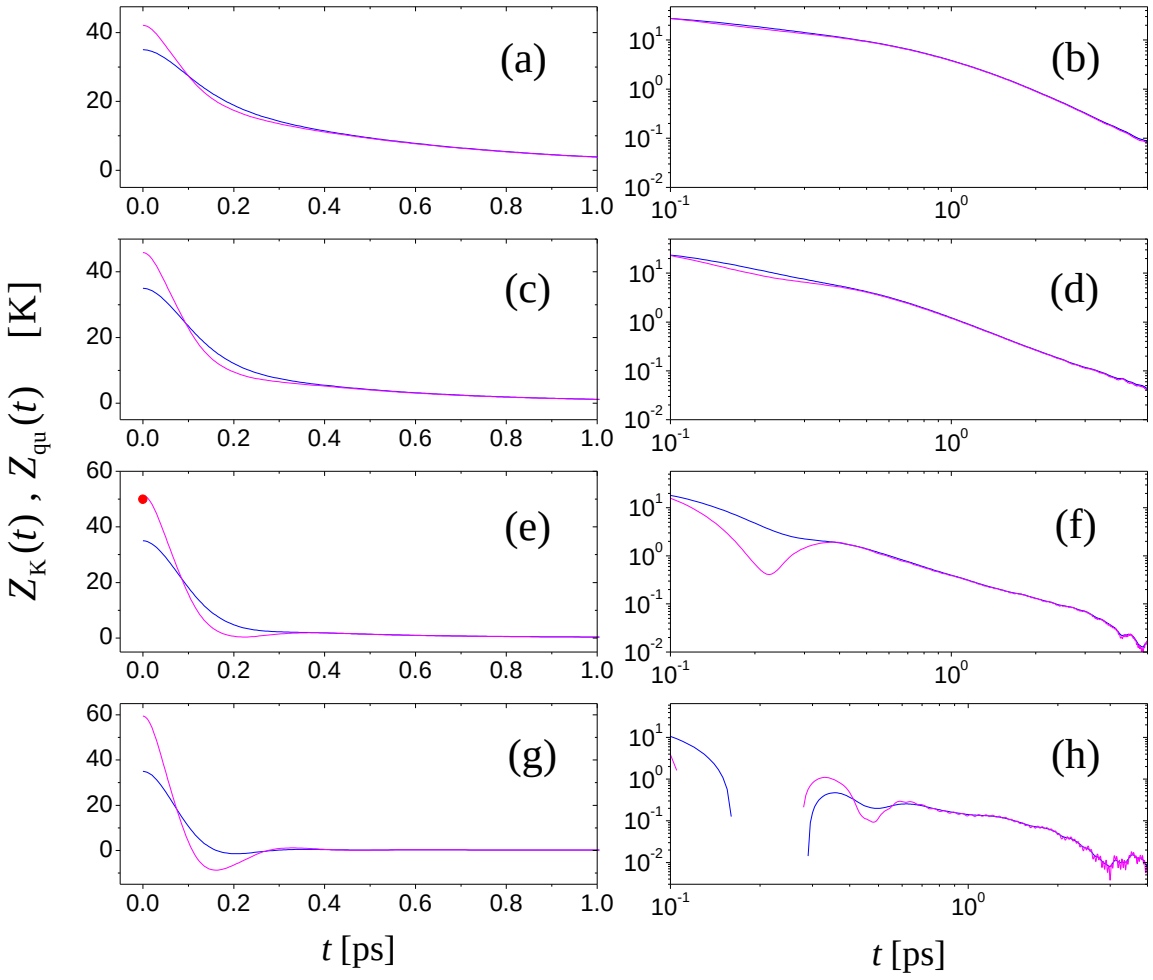

Figure 6.14: Comparison between the Kubo-transformed VAF $Z_K(t)$ obtained from the simulation (blue line) and the real part of the quantum VAF $Z_{qu}(t)$ calculated through Eq. (6.26) (magenta line). (Left panels) Short-time behavior ($t \leq 1$ ps). The red point indicates the value obtained from a PIMC calculation. From top to bottom, the panels refer to densities $\rho = 9.79$ nm^{-3}, $\rho = 14.33$ nm^{-3}, $\rho = 19.29$ nm^{-3} and $\rho = 24.25$ nm^{-3}. (Right panels) Long-time behavior ($t \geq 1$ ps), same densities as above.

Chapter 7

Self dynamic structure factor and velocity autocorrelation function

In the previous chapters, the study of single-particle dynamics has been carried out with reference only to the velocity autocorrelation function $Z(t)$ and its frequency spectrum $\hat{Z}(\omega)$. However, from the experimental side, the quantity that neutrons are able to probe, through incoherent scattering, is not the VAF, but the single-particle dynamic structure factor $S_{\mathrm{self}}(Q,\omega)$ defined in Eq. (2.4), with $j = j'$. The achievement of a complete description of self dynamics requires that both $S_{\mathrm{self}}(Q,\omega)$ and $\hat{Z}(\omega)$ spectra are properly taken into account and analyzed in detail. Nonetheless, Eq. (2.17) shows that these spectra are closely related. Thus, in-depth analysis and implications of such a relationship have been the object of the last part of this thesis work. In particular, we took advantage of the multi-Lorentzian expansion method to describe $S_{\mathrm{self}}(Q,\omega)$ results of an ab initio simulation of liquid gold near the triple point state ($\rho = 53$ nm^{-3}, $T = 1350$ K). The information about the Lorentzian modes contributing to $S_{\mathrm{self}}(Q,\omega)$ can be used to derive the VAF frequency spectrum along with its mode decomposition.

Besides the interest in studying the dynamics of such a liquid metal, the choice of this particular system was also suggested by the availability of its $S_{\mathrm{self}}(Q,\omega)$ spectra in a wide range of wave vectors Q. Indeed, gold was one of the many conducting liquids that the Computing for Science group of ILL simulated in recent years by means of the Vienna Ab Initio Simulation Package. Results for the dynamic structure factor $S(Q,\omega)$ were already exploited by Guarini et al. [4], in combination with neutron Brillouin scattering data collected with the BRISP spec-

trometer (Institute Laue Langevin, Grenoble), to unveil the collective dynamics of this system. Self dynamic structure factor $S_{\mathrm{self}}(Q,\omega)$ data, instead, have been analyzed for the first time in this thesis.

The work of Ref. [4] is of particular importance for our case, not only because it has demonstrated the reliability of such simulations for gold, thus reassuring about their reliable use for additional studies, but also because it has allowed to exploit the results there reported to investigate the relationship between self and collective dynamics, already shown in Ch. 5 for a supercritical LJ fluid, also in a real liquid at the triple point state.

It is important to stress however that the case of gold is taken here as a mere, though significant, example, and that the method of analysis we propose has an absolute general validity. In principle, the method may be applied also to experimental data, although, in this case, some difficulties are surely posed by the presence of noise in the far wings of spectra.

7.1 Introduction

We have shown in Ch. 5 that the way collective modes produce their signature on the $\hat{Z}(\omega)$ of a Lennard-Jones (LJ) fluid indeed permits to interpret the VAF spectrum as the global DoS of a liquid, generalizing a well-known concept of solid-state physics. Thus, it is clear why the analysis of this quantity in condensed systems becomes of invaluable help for the investigation of collective properties as, for example, the transverse wave propagation.

In recent years, the discussion about the transverse dynamics of liquids strongly came into foreground due to experiments revealing the existence of a second low-frequency branch in the dispersion curve not only of associated liquids [70, 87], but also of several liquid metals, as probed by X-rays [88, 89, 90, 91, 92] and neutron [69] spectroscopy. The latter systems, in particular, were also extensively studied by means of ab initio simulations [93, 94, 95]. In one case [69], the nature of the modes was more confidently assigned by comparison of the dispersion curve of the liquid with the DoS of the system in the solid phase, which indeed showed maxima related to transverse and longitudinal modes in agreement with the features and frequencies of the two branches measured in the molten metal. The existence and detectability of shear modes in these systems have sometimes been attributed to anisotropic interactions

giving rise to particular structural properties, like the presence of dimers and/or instantaneous cage formation [88, 91]. It is also believed that the specific structural features of a metal in the crystalline phase, i.e. the more or less pronounced anisotropy of the structure in which a system tends to crystallize, might provide an indication about the greater or lower visibility of a richer dynamical behavior in the $S(Q,\omega)$ of liquids. In this respect, liquid gold (fcc in the solid phase) might be expected to show a simpler dynamics than liquid zinc (hcp in the solid phase and with an anomalous c/a ratio) [69], although there is the counter example of the liquid sodium case [89, 90] (cubic in the solid phase).

Indeed, the study of liquid gold dynamics in Ref. [4] shows a beautiful but rather familiar behavior, with a single acoustic mode perfectly accounting for the inelastic part of the spectrum, and with a dispersion curve clearly longitudinal in nature. The viscoelastic analysis (see Ref. [28] for a review) of the simulated $S(Q,\omega)$ provided excellent fits, and later attempts to include a second possible inelastic mode in the fit function turned out into a worse description of the spectra. Also, a deeper Bayesian statistical analysis of the experimental data set recently confirmed that the presence of a second inelastic mode is not justified on a statistical basis within the accuracy of the available $S(Q,\omega)$ data [96]. These findings are however not conclusive about the absence of transverse modes in liquid gold because several effects, like for instance a too low intensity, might hinder their direct detection.

Access to the DoS of the liquid would therefore be extremely useful to better probe the vibrational dynamics in cases like the one of liquid gold, and could become a powerful method to establish if the presence of shear modes is a more general feature of liquids. However, $\hat{Z}(\omega)$ determinations from measurements of $S_{\mathrm{self}}(Q,\omega)$ require some way to get rid of resolution effects, as recognized in the experimental papers devoted to such an attempt [97, 66, 98]. Indeed, the $Q \to 0$ extrapolation, requiring an ω by ω study of the spectra measured at finite-Q, becomes critical in the presence of a resolution broadening that grows in importance as Q is decreased. On the other hand, it is very difficult to perform a deconvolution. Moreover, another problem discussed in Refs. [97, 66, 99, 98] concerned the appropriate Q-functionality to be used for extrapolation. So, on one side, accurate extraction of the VAF spectrum from $S_{\mathrm{self}}(Q,\omega)$ determinations revealed to be not at all a simple task. On the other side, the interest in this function was, at that time, focused on the detection of the long-time tail (LTT) phenomenon (see Ch. 4),

so that the great potential of $\hat{Z}(\omega)$ determinations for more general dynamical considerations remained partly obscure and was not pursued further.

Here we show that this is indeed possible by taking advantage of the multi-exponential theory reported in Refs. [1, 2, 3] and used throughout this thesis.

7.2 Theoretical considerations

As already recalled in par. 2.4, given a normalized autocorrelation function $b(t)$ of a classical system, its representation at $t \geq 0$ is

$$b(t) = \frac{\langle B(0)B(t)\rangle}{\langle B^2\rangle} = \sum_{k=1}^{\infty} I_k \mathrm{e}^{z_k t}, \tag{7.1}$$

where I_k and z_k are amplitude and complex-frequency, respectively, of the k-th mode. The spectrum of $b(t)$, defined as its Fourier transform (FT) $b(\omega) = \frac{1}{2\pi}\int_{-\infty}^{+\infty} \mathrm{d}t\, b(t)\mathrm{e}^{-i\omega t}$ is given by

$$b(\omega) = \sum_{k=1}^{\infty} b_k(\omega) = \sum_{k=1}^{\infty} \frac{1}{\pi}\mathrm{Re}\frac{I_k}{i\omega - z_k}, \tag{7.2}$$

where $b_k(\omega)$ is a generalized Lorentzian line. If I_k and z_k are real then $b_k(\omega)$ is a true Lorentzian (see Eq. (2.42)). If I_k and z_k are complex, then the corresponding mode (k) and its conjugate ($k+1$) sum together to give a pair of distorted inelastic Lorentzians (see Eq. (2.43)). We have adopted here the following convention: if a mode has $z_k = -|z_k^{'}| + i|z_k^{''}|$ then its amplitude is written as $I_k = I_k^{'} + iI_k^{''}$ where $I_k^{'}$ and $I_k^{''}$ have no restriction in sign. Correspondingly, $z_k = -|z_k^{'}| - i|z_k^{''}|$ and $I_k = I_k^{'} - iI_k^{''}$. Exploiting the relation between the p-th time derivative of $b(t)$ in $t = 0$ and the p-th frequency moment $\langle\omega^p\rangle$ of the spectrum $b(\omega)$, a set of sum rules can be defined as:

$$\sum_{k=1}^{\infty} I_k z_k^p = i^p\langle\omega^p\rangle. \tag{7.3}$$

An extremely simple result, but of great importance for the next determination of the liquid DoS, is the one regarding the correlation function related to the second time derivative of $b(t)$, that is the correlation

$$c(t) = \frac{\langle \dot{B}(0)\dot{B}(t)\rangle}{\langle B^2\rangle} = -\ddot{b}(t), \tag{7.4}$$

whose spectrum is $c(\omega) = \omega^2 b(\omega)$. However, direct differentiation of $b(t)$ gives, for $t \to 0$, and according to Eq. (7.1):

$$c(t) = \sum_{k=1}^{\infty}(-I_k z_k^2)\mathrm{e}^{z_k t}, \tag{7.5}$$

so that its spectrum can also be written as

$$c(\omega) = \sum_{k=1}^{\infty}\frac{1}{\pi}\mathrm{Re}\frac{(-I_k z_k^2)}{i\omega - z_k}. \tag{7.6}$$

Therefore, from Eqs. (7.2) and (7.6), it is seen that

$$c(\omega) = \omega^2\sum_{k=1}^{\infty}\frac{1}{\pi}\mathrm{Re}\frac{I_k}{i\omega - z_k} = \sum_{k=1}^{\infty}\frac{1}{\pi}\mathrm{Re}\frac{(-I_k z_k^2)}{i\omega - z_k}. \tag{7.7}$$

Note that the last equality in Eq. (7.7) is a straightforward algebraic identity if the sum rule $\sum_{k=1}^{\infty} I_k z_k = 0$ (Eq. (7.3) with $p = 1$) is used. Despite its simplicity, such a relation carries the important meaning that the autocorrelation function of a dynamical variable $B(t)$ and that of its derivatives are characterized by the same time decays or complex frequencies, therefore describe essentially the same dynamics. The same generalized Lorentzians describe the spectra $b(\omega)$ and $c(\omega)$, with only different amplitudes, where those of $c(\omega)$ are readily obtained by multiplying the amplitudes $b_k(\omega)$ by the negative of the squared "generalized half-width" z_k (either real or complex).

While the multi-exponential expansion (Eq. (7.1)) applies to any autocorrelation function, and the corresponding multi-Lorentzian representation (Eq. (7.2)) describes the respective spectrum, the result expressed by Eq. (7.6) is of particular importance in those cases in which two meaningful autocorrelation functions are linked by a double time differentiation. A well-known example is the case of the intermediate scattering function $F(Q,t)$, and the longitudinal current autocorrelation $C_{\mathrm{L}}(Q,t)$ [9]. Here, however, we are concerned with the self intermediate scattering function $F_{\mathrm{self}}(Q,t)$ and the VAF:

$$Z(t) = \langle \mathbf{v}(0)\cdot\mathbf{v}(t)\rangle \tag{7.8}$$

Note that, hereafter, $Z(t)$ will indicate the VAF instead of its normalized version as Eq. (2.19). In the next paragraph we will exploit the fact that $Z(t)$ can be obtained from $F_{\mathrm{self}}(Q,t)$ in a way which also includes a double differentiation, and that Eq. (7.6) establishes therefore a direct connection between the multi-Lorentzian expansion of their respective Fourier transforms, namely the spectrum $Z(\omega)$ of the VAF and $S_{\mathrm{self}}(Q,\omega)$.

The exponential mode expansion method is to be applied by a suitable truncation of the infinite series depending on the extension and accuracy of available data, as discussed in par. 2.4. As shown in Chs. 4 and 5, this was successfully done in the time domain to interpret the dynamical behavior of a Lennard-Jones fluid at various densities and temperatures. In all analyzed cases it was shown that a limited number of modes was required to achieve an excellent description of the simulated VAF, with a suitable number of obeyed moment sum rules. Here we show that an identical situation is found in the frequency domain, and by considering the spectrum ($S_{\mathrm{self}}(Q,\omega)$) of a different autocorrelation function ($F_{\mathrm{self}}(Q,t)$).

7.3 Methodology and results

Being interested here in the determination of the DoS of a liquid starting from self spectra, are shown in Fig. 7.1 the gold self-spectra as obtained from the ab initio simulations of Ref. [4] at some example Q values. The use of a semilogarithmic scale immediately highlights the presence of at least one shoulder located at $\omega \simeq 30$ ps^{-1}, which is also found at all investigated Q values.

Despite this rather surprising result for the shape of $S_{\mathrm{self}}(Q,\omega)$, usually not investigated in such a wide ω range, it will be clear in the following that these shoulders are genuine features of the spectra which are approximately positioned at the same frequency where maxima in the longitudinal dispersion curve take place (see Fig. 7 in Ref. [4]). This preliminary observation will find an explanation in the next discussion of the DoS, however it is useful to anticipate that the spectral features of $S_{\mathrm{self}}(Q,\omega)$ at large ω are strictly linked to those of the DoS.

In order to illustrate the relation between the DoS and $S_{\mathrm{self}}(Q,\omega)$, it is useful to introduce $Z_{\mathrm{E}}(Q,\omega)$, defined as (see Eqs. (2.16) and (2.17))

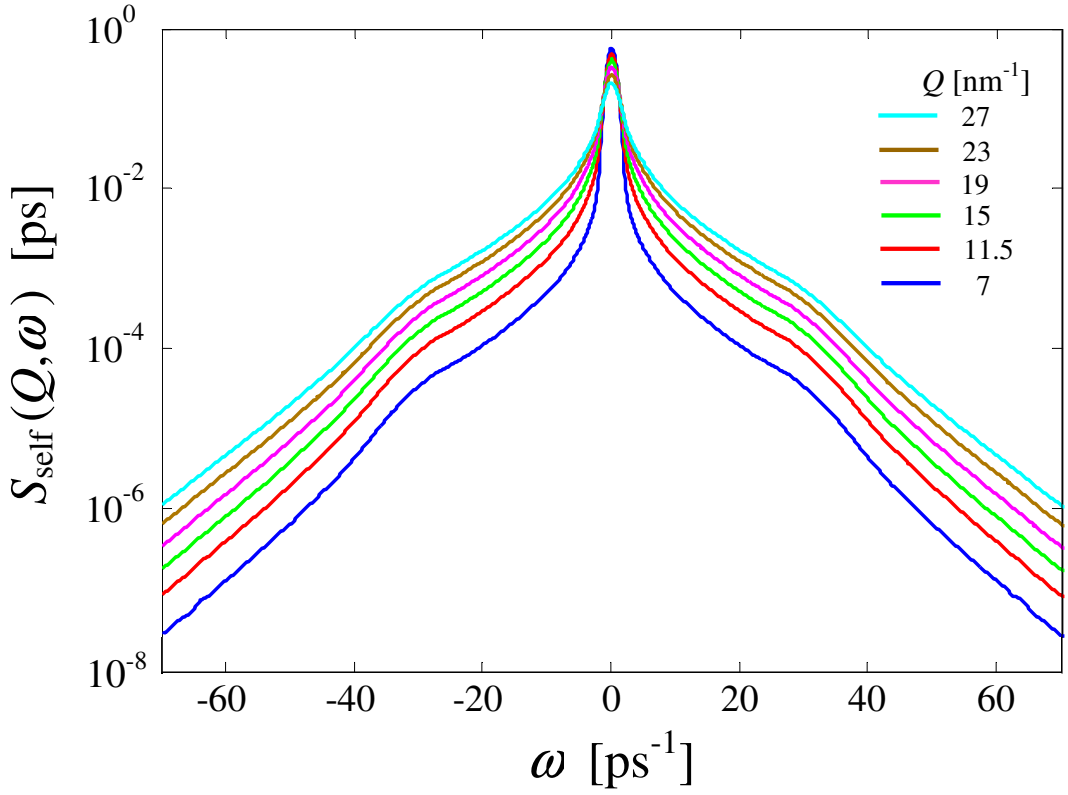

Figure 7.1: Self dynamic structure factor of liquid Au at the Q values reported in the legend.

$$Z_{\mathrm{E}}(Q,\omega) = \frac{3\omega^2}{Q^2} S_{\mathrm{self}}(Q,\omega) \tag{7.9}$$

the $Q \to 0$ limit of which is the DoS according to the Egelstaff formula (indicated by the subscript E) [100]:

$$Z_{\mathrm{E}}(\omega) = \lim_{Q\to 0} Z_{\mathrm{E}}(Q,\omega) = \lim_{Q\to 0} \frac{3\omega^2}{Q^2} S_{\mathrm{self}}(Q,\omega) \tag{7.10}$$

However, the above definition of $Z_{\mathrm{E}}(\omega)$ hides a discontinuity in $\omega = 0$, since different results are obtained for $Z_{\mathrm{E}}(\omega = 0)$ depending on the order used to perform the $Q \to 0$ and $\omega \to 0$ limits in Eq. (7.10) [66]. In particular, only by performing the $Q \to 0$ limit before the $\omega \to 0$ one Eq. (7.10) provides the correct zero-frequency value $Z(0) = 3D_s/\pi$, with D_s the self diffusion coefficient. This value is obtained straightforwardly from the Green-Kubo relation (2.23) and considering that $\int_0^\infty \mathrm{d}t\, Z(t) = \pi Z(\omega = 0)$. By recalling that in the hydrodynamic, $Q \to 0$, regime $S_{\mathrm{self}}(Q,\omega)$ reduces to the one-Lorentzian spectrum predicted by Fick's law of simple diffusion

[9]:

$$S_{\text{self}}(Q \to 0, \omega) = \frac{1}{\pi} \frac{D_s Q^2}{\omega^2 + D_s^2 Q^4} \tag{7.11}$$

it is seen that by performing the limits in the reverse order one obtains the wrong result $Z_{\text{E}}(\omega = 0) = 0$.

Morkel and Gronemeyer [66] have shown that the pathological behavior of $Z_{\text{E}}(\omega)$ in $\omega = 0$ can be corrected and the quoted discontinuity removed, by replacing $Z_{\text{E}}(Q, \omega)$ with

$$Z(Q, \omega) = \frac{3}{Q^2} S_{\text{self}}(Q, \omega)(\omega^2 + D_s^2 Q^4) \tag{7.12}$$

which is continuous also in the origin ($Q = 0$ and $\omega = 0$) and provides $Z(\omega)$ as

$$Z(\omega) = \lim_{Q \to 0} Z(Q, \omega) \tag{7.13}$$

Combination of Eqs. (7.12) and (7.13) and analysis of the $S_{\text{self}}(Q, \omega)$ spectra thus allows to determine the DoS as described in the next subsections.

7.3.1 Q behavior of the spectral components of $S_{\text{self}}(Q, \omega)$

We used the multi-Lorentzian expansion (Eq. (7.2)) of $S_{\text{self}}(Q, \omega)$, i.e.

$$S_{\text{self}}(Q, \omega) = \sum_{k=1}^{\infty} \frac{1}{\pi} \text{Re} \frac{I_k(Q)}{i\omega - z_k(Q)} \tag{7.14}$$

in order to find, through a fit procedure, the amplitudes $I_k(Q)$ and complex frequencies $z_k(Q)$ of the modes contributing to the spectra.

Both experimental and simulation $S_{\text{self}}(Q, \omega)$ data are affected by a resolution broadening, although its origin is different in the two cases. In experiments the broadening depends on the characteristics of the spectrometer setup while, in simulations, it arises from the application of a tapering windowing in the time domain, i.e. to $F_{\text{self}}(Q, t)$, with the purpose of making the function to be Fourier-transformed sufficiently decayed to zero at large times. In particular, in the present case we applied a Gaussian window with a full width at half maximum equal to 1.52 ps^{-1}. In both cases the convolution of the fit model with the resolution function is a very effective way to get rid of any broadening and to obtain resolution-free results. An excellent

representation of the Au self spectra was actually obtained by considering six modes: two real modes (labeled as R1 and R2) and four complex modes (indicated as C1 pair and C2 pair), the sum of which was forced to obey the zero-th, first, third and fifth frequency moment sum rules. These constraints ensure finite even moments of $S_{\mathrm{self}}(Q,\omega)$ up to the sixth one, with the resulting second moment checked a posteriori to perfectly agree with the theoretical value $k_{\mathrm{B}}TQ^2/M$ [9], with k_{B} the Boltzmann constant, T the temperature, and M the atomic mass of gold.

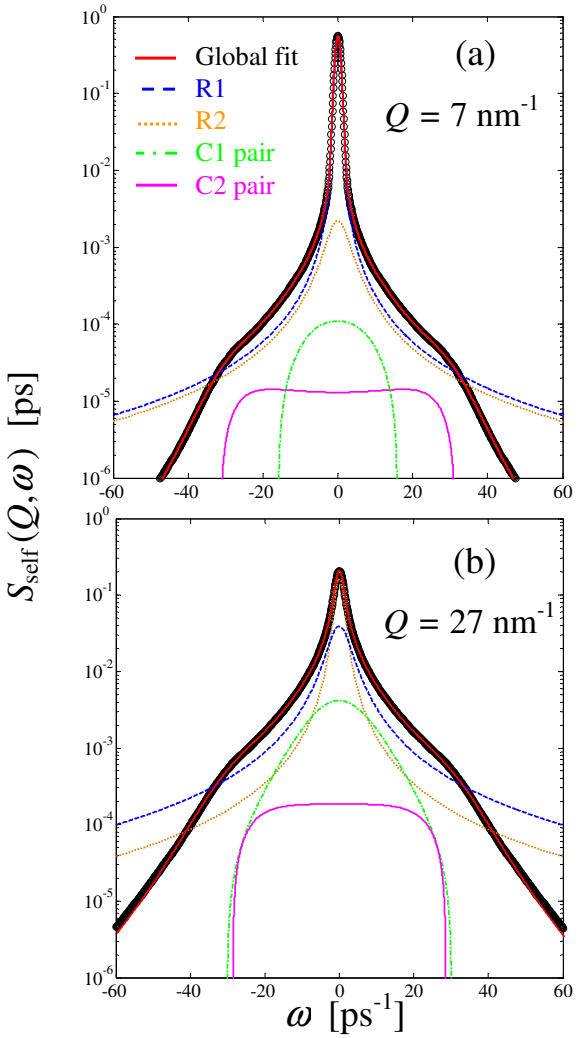

Figure 7.2: Self dynamic structure factor of liquid Au (black circles) at two Q values. The real (dashed blue and dotted orange curves) and complex (solid magenta and dash-dotted green curves) components that give rise to the overall fit curve (red solid curve) are shown along with the simulation data on a semi-logarithmic scale.

Figure 7.2 shows the very good performance of the fit model at two Q values (the second

close to Q_p, the position of the main maximum in the static structure factor $S(Q)$). The various components of the global fit function are also plotted to evidence the impossibility to reproduce the shape of the self spectrum with real modes only. In order to construct $Z(\omega)$ via Eqs. (7.12) and (7.13), an analysis of the Q-dependence of the various parameters and a final $Q \to 0$ extrapolation of all of them is required.

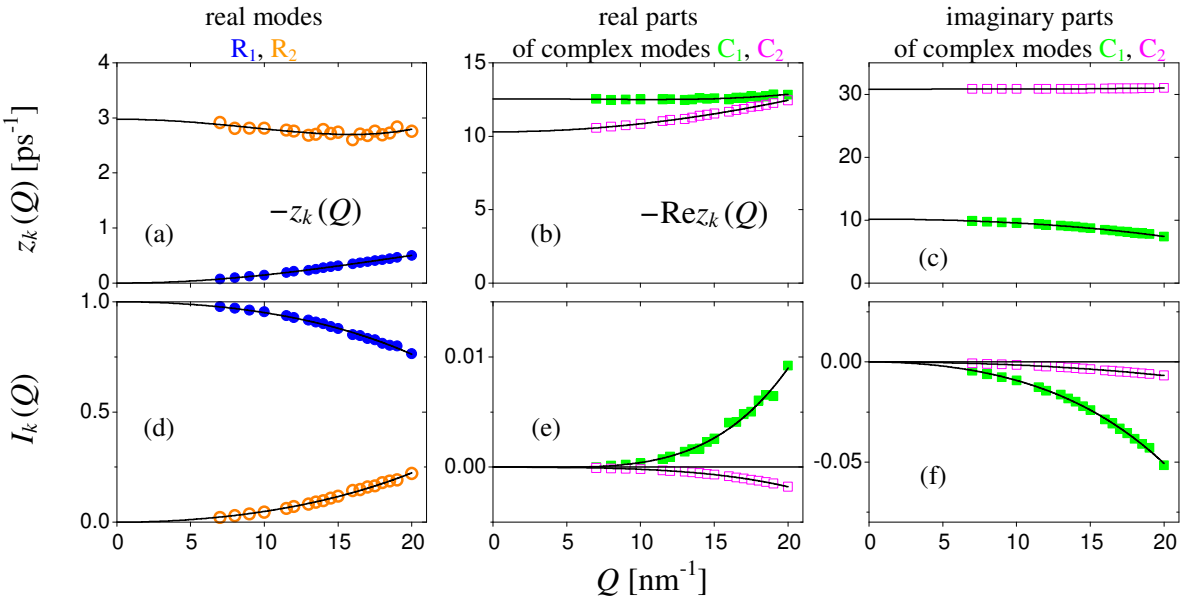

Figure 7.3: Dependence of the parameters z_k (top frames) and I_k (bottom frames), fitted to $S_{\mathrm{self}}(Q,\omega)$ data. In each row, the left panel refers to the two real exponential modes (labeled R1 and R2, and displayed as dots and open circles respectively), the center and right panels display the real and imaginary parts of the parameters of the two pairs of complex modes (labeled C1 and C2, and displayed as filled and empty squares respectively). In all frames, the colors are those indicated in the top labels. Black solid lines represent the best fitting polynomials in powers of Q^2 up to the Q^4 term. In (a) and (b) the absolute values of the negative quantities z_k and $\mathrm{Re}z_k$ are plotted. For each complex pair we chose to plot the amplitude (with its own sign) of the mode in the pair having $\mathrm{Im}z_k > 0$.

As Fig. 7.3 shows, the real and complex eigenfrequencies $z_k(Q)$ and amplitudes $I_k(Q)$ have all very smooth trends that enable a reliable $Q \to 0$ extrapolation by means of polynomials. However, several useful observations are worth anticipating by looking at Fig. 7.3. In particular, in compliance with the exact hydrodynamic limit, only one mode (R1) is seen from Fig. 7.3 (d) to survive in $S_{\mathrm{self}}(Q,\omega)$ as $Q \to 0$, since the amplitudes $I_k(Q)$ of all other modes in Fig. 7.3 (d)-(f) vanish. Consistently, also the damping $-z_{\mathrm{R1}}$ can be recognized at glance to follow the parabolic behavior typical of Fick's simple diffusion, which we find to hold up to the rather high

value $Q = 18\ \mathrm{nm}^{-1}$. Thus, in Fig. 7.2, R1 can be confidently identified with the pure Lorentzian line predicted by Fick's law.

The other real component (R2), necessary, together with R1 to properly describe the central peak of $S_{\mathrm{self}}(Q,\omega)$, displays a non-hydrodynamic behavior witnessed by the almost constant width and by an amplitude that grows with Q to the detriment of the R1 one. It is useful to compare the decay time constant $\tau_{\mathrm{R2}} = -1/z_{\mathrm{R2}}$ with the Enskog mean collision time τ_{E} (see Eq. (4.4)) of liquid gold at the number density of melting $\rho = 53.03\ \mathrm{nm}^{-3}$ (the hard sphere diameter σ of gold at melting is taken from Ref. [101]). The result for τ_{E} turns out to be 0.03 ps, that is approximately ten times smaller than τ_{R2}. This classifies R2 as a rather slow relaxation process that involves quite a number of collisions, but which is anyway much faster than the hydrodynamic mode R1, for which $\tau_{\mathrm{R1}} = -1/z_{\mathrm{R1}} \approx 2$ ps at our highest Q.

The complex contribution C2 is seen to account for the previously commented inelastic feature in $S_{\mathrm{self}}(Q,\omega)$ (see Fig. 7.1), with a frequency in very close agreement with the maximum of the observed dispersion [4] of purely longitudinal propagating sound waves. A similar identification was done in Ch. 5 by applying the multiexponential analysis to the VAF of a LJ high density fluid. This means that self correlation functions clearly carry the fingerprints of the underlying collective dynamics, and that these are reflected by the need of including at least one complex mode in the model if a proper description of self spectra wants to be obtained. However, the physical origin of the other complex component (C1) will be clarified after the next determination of $Z(\omega)$ (see par. 7.4).

The self intermediate scattering function $F_{\mathrm{self}}(Q,t)$ of classical systems is known [15] to be a function of Q^2, and Fourier transformation to $S_{\mathrm{self}}(Q,\omega)$ does not alter this property. This suggests that the low-Q dependence of $I_k(Q)$ and $z_k(Q)$ is properly described by Q^2 polynomials of the general form $a + bQ^2 + cQ^4 + \cdots$ (where the first term may be missing for some of the parameters) and that the $Q \to 0$ behavior can be determined by fitting such polynomials. In the used fit range ($7\ \mathrm{nm}^{-1} < Q < 20\ \mathrm{nm}^{-1}$) it turns out to be sufficient to limit oneself to Q^4 terms for all parameters $I_k(Q)$ and $z_k(Q)$. More in detail, and recalling that R1 can be identified with Fick's mode, it is seen from Fig. 7.3 that the Q behavior of the parameters is very well

accounted for by the following expansions, without the need to include odd powers of Q:

$$\begin{cases} I_{\mathrm{R1}}(Q) = 1 + O(Q^2) \\ z_{\mathrm{R1}}(Q) = -D_s Q^2 + O(Q^4) \end{cases} \tag{7.15}$$

for the first real mode R1 ($k = 1$), and

$$\begin{cases} I_k(Q) = p_k Q^2 + O(Q^4) \\ z_k(Q) = z_k(0) + O(Q^2) \end{cases} \tag{7.16}$$

for all the other modes ($k \geq 2$), with the parameters p_k independent of Q.

We stress that the Q^2 coefficient in the fit function of $z_{\mathrm{R1}}(Q)$, i.e. $-D_s$, was left as a free parameter. In fact, no experimental determination of D_s for liquid gold appears to be available, and calculated or simulated estimates often disagree, with a range of variability between 0.6 and $3.5 \cdot 10^{-3}$ nm^{2}ps^{-1} [102, 103, 104]. Our fit provides $D_s = 1.5 \cdot 10^{-3}$ nm^{2}ps^{-1}, in good agreement with the calculation of Ref. [102] and with one of the values of Ref. [104].

7.3.2 Mode expansion of $Z(Q, \omega)$ and determination of $Z(\omega)$

The previous analysis of $S_{\mathrm{self}}(Q, \omega)$ allows, through the general relations of Eqs. (7.2), (7.7), (7.12) and (7.14), to derive $Z(Q, \omega)$ as

$$Z(Q, \omega) = \sum_{k=1}^{\infty} \frac{1}{\pi} \mathrm{Re} \frac{A_k(Q)}{i\omega - z_k(Q)} \tag{7.17}$$

with amplitudes of the modes given by

$$A_k(Q) = -\frac{3}{Q^2} z_k^2(Q) I_k(Q) + 3 D_s^2 Q^2 I_k(Q) \tag{7.18}$$

Using Eqs. (7.13) and (7.17), the DoS is therefore obtained as:

$$Z(\omega) = \lim_{Q \to 0} Z(Q, \omega) = \sum_{k=1}^{\infty} \frac{1}{\pi} \mathrm{Re} \frac{A_k(Q \to 0)}{i\omega - z_k(Q \to 0)} \tag{7.19}$$

which requires the determination of the $Q \to 0$ limit of the various $A_k(Q)$. Before discussing the extrapolation, important insight is provided by the analysis of Fig. 7.4 where we report, for all real and complex modes, the amplitudes of Eq. (7.18) as a function of Q.

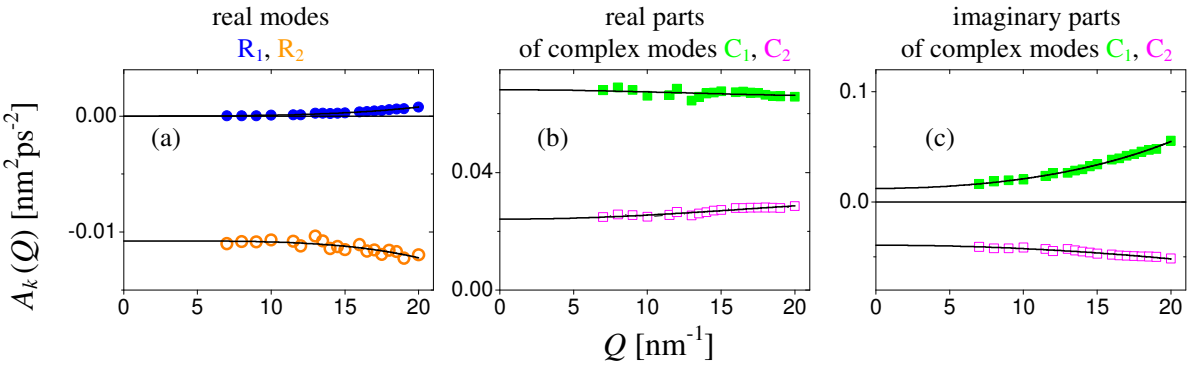

Figure 7.4: As in Fig. 7.3 for the amplitudes A_k of the modes contributing to $Z(Q,\omega)$.

From Fig. 7.4 it is immediately evident that only one component (R1, panel (a)) has a vanishing amplitude at low Q. This actually means that the Fick's mode R1, which is so important in the description of $S_{\text{self}}(Q,\omega)$ at small Q and is the only surviving Lorentzian in $S_{\text{self}}(Q,\omega)$ as $Q \to 0$, actually does not contribute to the DoS (Eq. (7.19)) at any frequencies. Thus, the presence of mass diffusion, witnessed by one of the modes of $S_{\text{self}}(Q,\omega)$, is accounted for in $Z(\omega)$ by all modes but R1. It is straightforward to show that it is the combination of the other three modes that provides the correct non-zero $Z(0)$ starting value of the DoS. To this aim we insert Eq. (7.19) into the Green-Kubo relation (2.23) that yields D_s and perform the time integration, obtaining

$$D_s = \frac{1}{3}\sum_k \lim_{Q\to 0}\left(-\frac{A_k}{z_k}\right) \tag{7.20}$$

and using Eqs. (7.15) and (7.16) it is easy to find that the R1 mode gives a null contribution to the sum. The other terms together provide the value $\sum_{k\geq 2} p_k z_k(0)$, which can be evaluated using the $p = 1$ sum rule, as follows:

$$\begin{aligned} 0 = \sum_k I_k(Q) z_k(Q) &= -D_s Q^2 + \sum_{k\geq 2} p_k z_k(0) Q^2 + O(Q^4) \\ &= Q^2\left(-D_s + \sum_{k\geq 2} p_k z_k(0)\right) + O(Q^4) \end{aligned} \tag{7.21}$$

which shows that

$$\sum_{k\geq 2} p_k z_k(0) = D_s \tag{7.22}$$

Therefore, the contribution of the various modes of $S_{\text{self}}(Q,\omega)$ to the diffusion coefficient undergoes a null sum rule, which in the $Q \to 0$ limit entrusts the value of the Green-Kubo integral to the remaining microscopic (non-Fick) modes R2, C1 and C2, which together yield the expected macroscopic transport coefficient related to the $\omega = 0$ value of the DoS.

We now turn to the final evaluation of Eq. (7.19). Given the quality of the Q-fits to the various $I_k(Q)$ and $z_k(Q)$ of Fig. 7.3 and recalling Eq. (7.18), also $A_k(Q)$ is of course well described by the same polynomials of the form $a + bQ^2 + cQ^4$, as shown in Fig. 7.4. In order to reach a better numerical accuracy we preferred to fit them to $A_k(Q)$ themselves, rather than deriving their extrapolated values from Eq. (7.18) with $I_k(Q \to 0)$ and $z_k(Q \to 0)$. By extrapolation of the polynomial fits we derived the asymptotic values $A_k(Q \to 0)$ that appear as amplitudes of the various terms of Eq. (7.19) and we finally calculated the DoS reported in Fig. 7.5, along with its components.

In order to better validate such method to access the $Z(\omega)$ of a liquid via possible incoherent neutron scattering experiments, we also directly computed the liquid gold VAF from the available ab initio simulations. Figure 6 shows the comparison of the just described DoS determination with the one obtained by direct Fourier transformation of the simulated VAF. It is evident from Fig. 7.6 that the agreement is remarkable, suggesting that the multi-Lorentzian fit to $S_{\text{self}}(Q,\omega)$ and subsequent extrapolation of the related parameters provides indeed the true limit $Z(\omega)$ curve.

This strong consistency between very different ways of determining the DoS (the second only possible if simulation data are available) has a great significance *per se* and represents an important result of the proposed method. Obviously the two routes also provide the same D_s value.

We note from Figs. 7.4(a) and 7.5 that the real mode R2 has a negative amplitude A_{R2} in agreement with Eq. (7.18) where the first term is negative and the second becomes negligible for small Q values. This can be understood by recalling the behavior of the amplitude I_{R2} and damping $-z_{\text{R2}}$ in Fig. 7.3(a) and (d), which induces to relate this mode to a trapping mechanism that tends to confine the particle, hindering diffusion in high density liquids. In this picture,

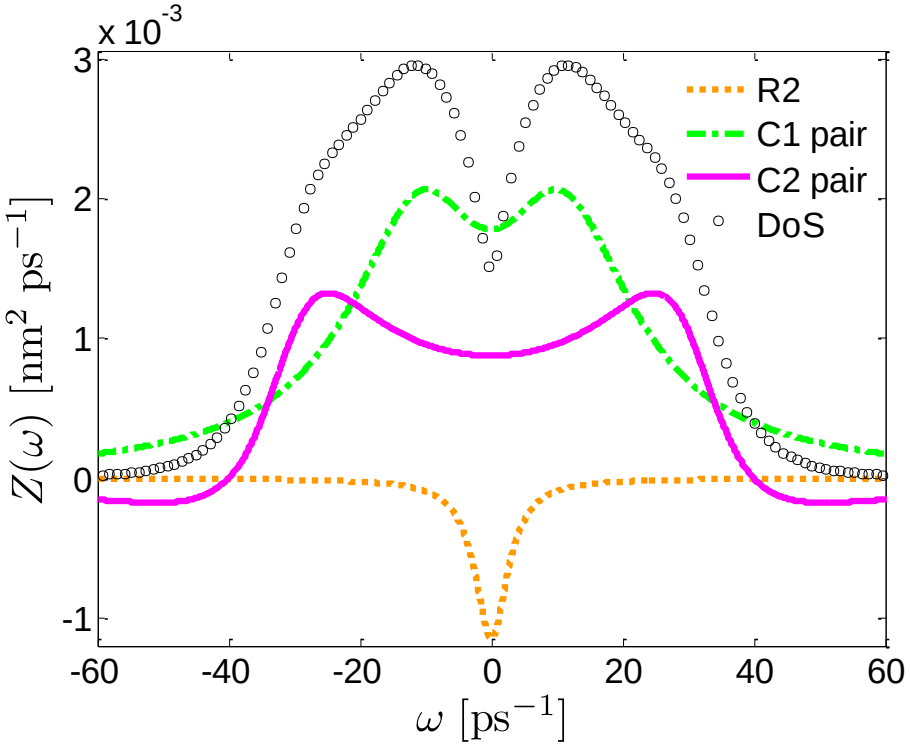

Figure 7.5: Density of states $Z(\omega)$ of liquid Au as obtained from the analysis of $S_{\text{self}}(Q,\omega)$ spectra with the method described in par. 7.3. The DoS (black circles) is shown along with its Lorentzian components specified in the legend.

$\tau_{\text{R2}} = -1/z_{\text{R2}}$, which is almost constant with Q, assumes the meaning of a residence time, after which the particle is able to diffuse again under the global effect of shear and acoustic waves traveling in the medium. Diffusion hindering phenomena can only show up as negative Lorentzians in the spectrum of the VAF, not only because of the mathematical relation of Eq. (7.18), but also because confinement physically corresponds to mechanisms that reduce the diffusion coefficient and the low frequency part of $Z(\omega)$.

7.4 $Z(\omega)$ and collective dynamics

These overall results indicate that, notwithstanding its fully single-particle character, $Z(\omega)$ is a very fruitful quantity also for the understanding of the collective dynamics. As mentioned, the C2 component can be ascribed to the collective longitudinal excitations present in the liquid. As regards the C1 pair, we are induced to identify it as due to transverse acoustic modes contribut-

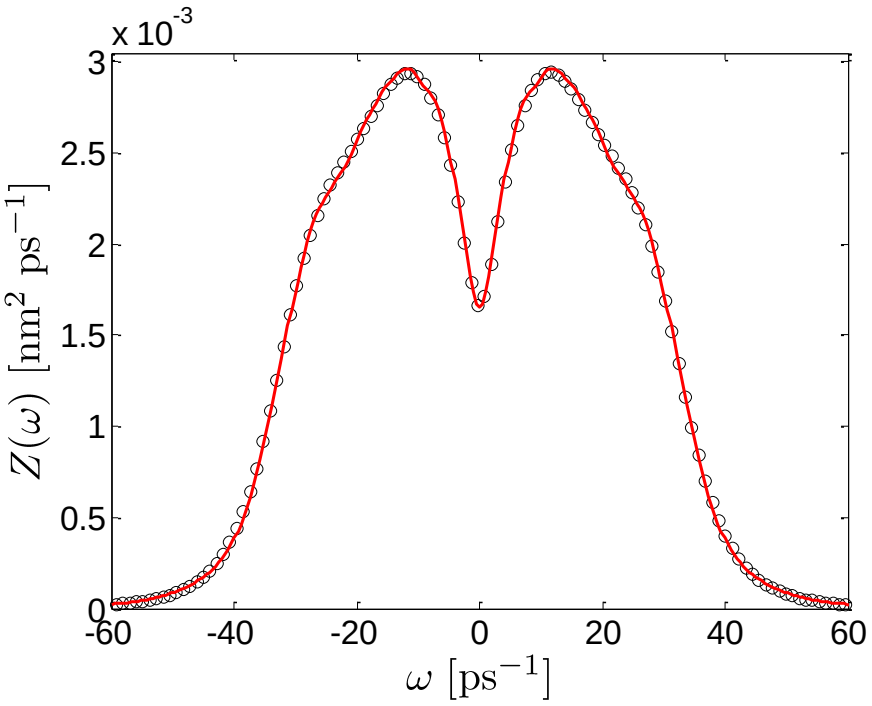

Figure 7.6: $Z(\omega)$ as obtained with the procedure leading to Fig. 7.5 (black circles) and by direct time FT of the simulation-derived VAF (red solid curve).

ing to the overall cooperative motions that the single particle behavior cannot avoid to mirror. Such a preliminary identification of C1 with the collective transverse contribution to the DoS is also in agreement with the typical behavior in the solid state case, where dispersion curves of transverse phonons involve typically lower frequencies and have a flatter Q dependence than longitudinal ones (giving rise to a pronounced peak in $Z(\omega)$ at low frequency).

The direct connection between the shape of $Z(\omega)$ and the presence of longitudinal and transverse modes in a dense liquid, is clarified in Figs. 7.7 and 7.8. Figure 7.7 shows how maxima in the dispersion curve, derived by determinations of the $S(Q,\omega)$ of liquid Au [4], find their evidence in the $Z(\omega)$ considered in the present work. We recall that the analysis of neutron and simulation data of $S(Q,\omega)$ for this specific liquid did not justify (even on a statistical basis [96]) the inclusion of more than one (longitudinal) excitation in the model fit function. However, as Fig. 7.7 shows, investigation of the overall dynamics requires more than considering $S(Q,\omega)$ only.

In the case of liquid gold, transverse low-frequency modes, though likely weak in intensity

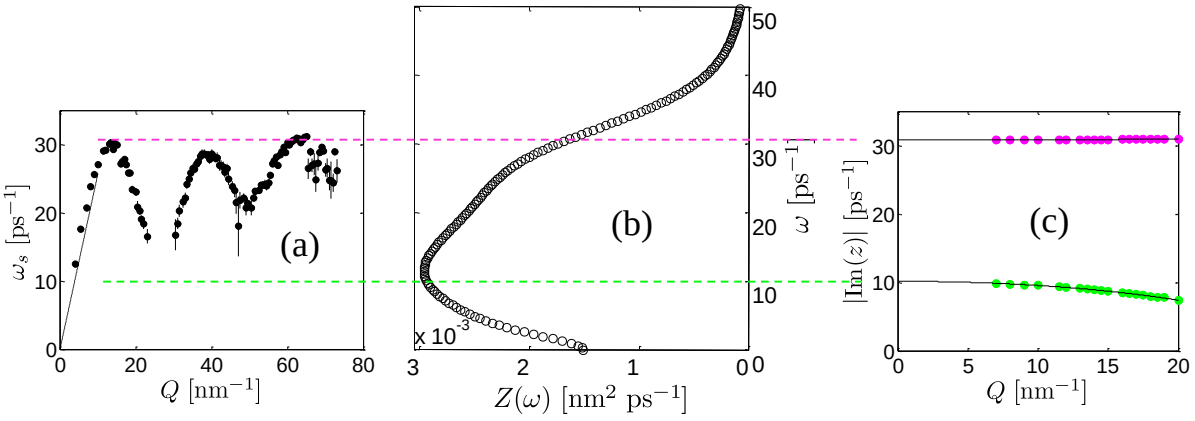

Figure 7.7: Dispersion curve of longitudinal modes of liquid gold as obtained in Ref. [4], compared with the shape of $Z(\omega)$. The maxima in the dispersion curve occur at frequencies in agreement with the shoulder in the DoS (the dashed pink line is a guide to the eye). Conversely, $S(Q,\omega)$ determinations miss the second branch accounting for the maximum in $Z(\omega)$. The last right panel is the same as that of Fig. 7.3 (c) and shows how the frequency of the C2 modes of $Z(\omega)$ agrees with the features of the longitudinal dispersion curve.

and undetectable from $S(Q,\omega)$ data, emerge neatly at the level of the VAF spectrum and of the spectrum $C_T(Q,\omega)$ of the transverse current autocorrelation function defined in Ref. [9]. The peak around 10 ps^{-1} in $Z(\omega)$ is indeed consistent with the behavior of the transverse current correlation spectra shown in Fig. 7.8. The maximum developing at nonzero frequency above $Q \simeq 6$ nm^{-1} in $C_T(Q,\omega)$ indicates the onset of transverse modes propagation in liquid gold at our thermodynamic conditions. The frequency of the maximum increases with Q but, after about 17 nm^{-1}, it stabilizes around 10 ps^{-1}. This means that, correspondingly, the transverse dispersion curve tends to flatten above this Q value, producing a maximum in $Z(\omega)$. Finally, as observed in other cases, the first of which represented to our knowledge by the paper of Sampoli et al. [70], the $C_T(Q,\omega)$ of liquid Au also shows evidence of a longitudinal contribution (an increasing bump around 25-30 ps^{-1}).

Some comments are also worth about another, implicit but significant, result of this work. In Ch. 5 the multi-exponential analysis was applied directly in the time domain to the simulated VAF of a LJ fluid in various thermodynamical states. For one of them, the nearest to the triple point (at least in density), the mode expansion was found to include three complex pairs and two real modes. One of the complex modes, of negligible intensity, represents a very fast oscillation

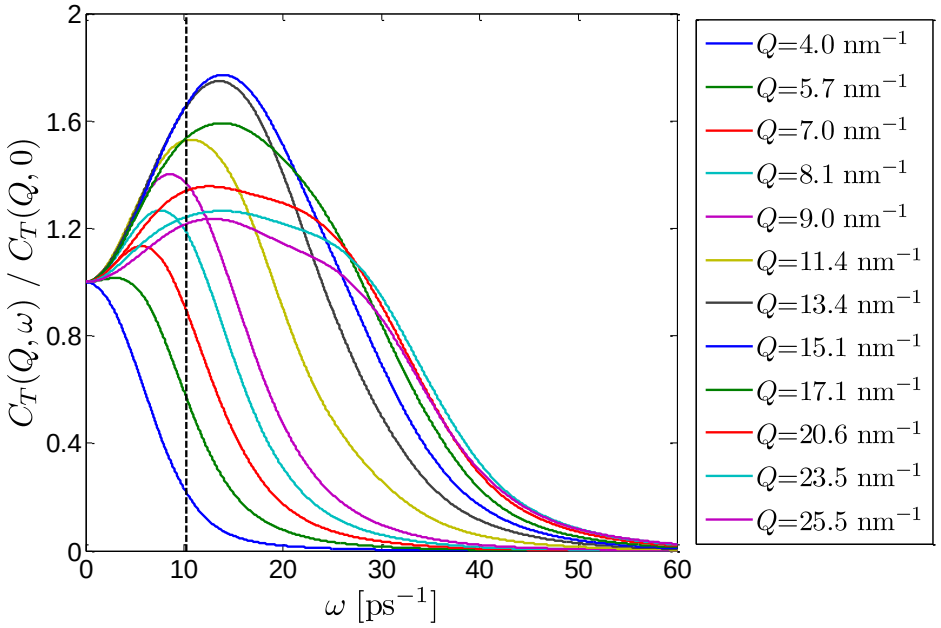

Figure 7.8: Transverse current correlation spectra calculated from the ab initio simulations and normalized to their $\omega = 0$ values. Several Q values are displayed in order to follow the onset of visible shear modes propagation above 6 nm^{-1}. The shapeless curves correspond to the lower Q values, while those developing a shoulder around 25 ps^{-1} correspond to the highest Q. The vertical dashed black line gives the frequency position of the main maximum in $Z(\omega)$, either from Fig. 7.5 or from Fig. 7.6.

of $Z(t)$ which, in the present case, is not detected in $S_{\mathrm{self}}(Q,\omega)$ because it would contribute to the farthest spectral wings. The other two complex modes correspond precisely, and with the same physical origin, to those denoted here as C1 and C2. A very slowly decaying real exponential, found in the LJ case to be the remnant of the long-time tail in the VAF, does not appear in the gold case, in agreement with the absence of a tiny tip at $\omega \simeq 0$ in the spectrum of the liquid gold VAF (Fig. 7.5), which is instead the typical spectral fingerprint of the presence of a very slow process. This indicates that in dense liquids much closer to the triple point (both in density and temperature), as in the present case, such a very slow real mode becomes undetectable due to a too short recurrence time of the simulations (see Ch. 4). The only remaining real mode (R0, see Ch. 5) found in the mentioned LJ high-density state corresponds to R2 here, and in both the LJ and liquid gold case this contributes with a negative central Lorentzian to $Z(\omega)$. As explained, some modes of the LJ fluid cannot be observed in the gold case, however no modes different from those here labeled as R2, C1, and C2 are found. Therefore, considering

the different thermodynamic states, the self dynamics undergoes the same mode-expansion, and with the same physical meaning of each mode, for systems as different as a model LJ fluid and a real liquid metal. Actually, we learn from this work, and the one reported in Ch. 5, different aspects of the nature of the mode R2 (R0), which is still a little controversial. In Ch. 5, thanks to a study at various densities, we recognized this mode as part of a group related to transverse dynamics. Here we do not contradict this fact, but we found more appropriate to keep the R2 mode separate from C1 (C3 in Ch. 5) pair.

7.5 Perspectives: self dynamics in a hydrogen-bonded liquid

The analysis of liquid gold surely opens interesting perspectives of application of the concepts reported in this chapter also to more complex, non-monatomic liquid systems. However, in some cases, when switching from a monatomic to a molecular system, translational dynamics can still be described in a similar way [105, 106, 107, 108], without too much complexity. Nevertheless, there is a particular class of liquids which exhibits a richer dynamical behavior: hydrogen-bonded (HB) liquids, with water the most extensively investigated one among them. In particular, we are mostly interested in the prototypical HB alcohol, methanol, since our recent work [87] has already shed some light on the collective dynamics characterizing this liquid, through a joint use of neutron Brillouin scattering measurements and molecular dynamics simulations.

Similarly to a large variety of liquids (including liquid gold), also the $S(Q,\omega)$ of methanol is shown in Ref. [87] to feature a normal viscoelastic behavior, which accounts for the propagation of longitudinal acoustic waves (orange squares in next Fig. 7.10). Besides this, however, two additional excitations were detected in the center-of-mass dynamic structure factor $S_{\mathrm{CM}}(Q,\omega)$: one at lower frequencies (magenta points in next Fig. 7.10), having a clear transverse origin, and one at higher frequencies (blue triangles in Fig. 7.10), which shows an optic-like behavior and is likely related to the stretching of hydrogen bonds. Here, we mention that the simulated system consisted in 4000 methanol molecules interacting through the OPLS-AA intermolecular potential at a temperature of 298 K and a pressure of 1 bar. More details about simulations will be reported in Ref. [87]

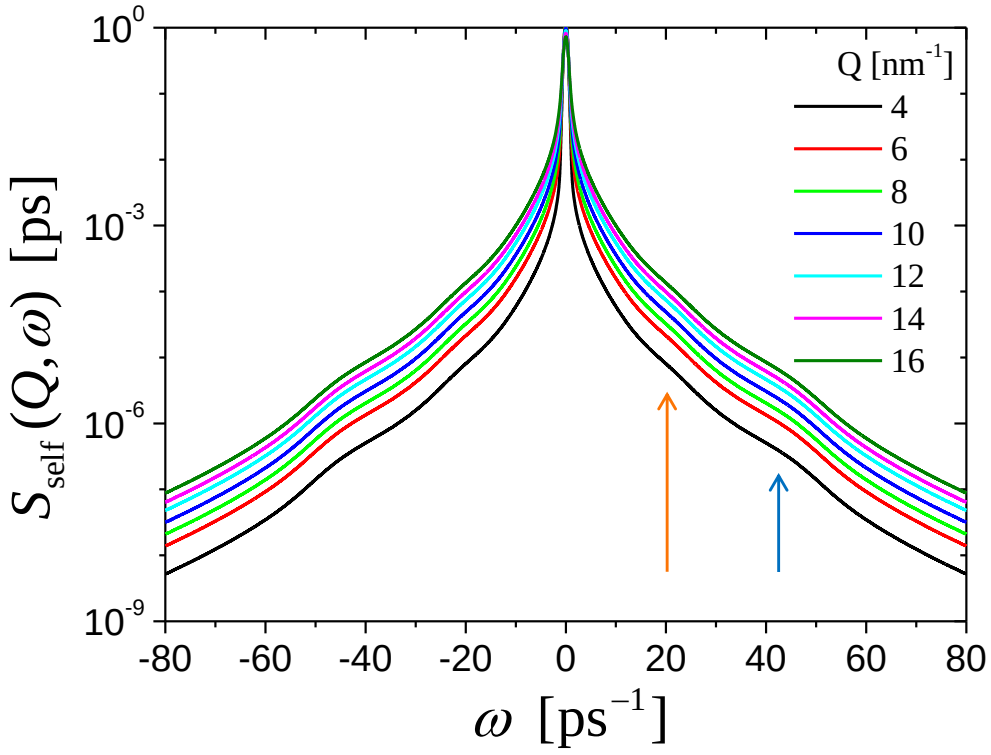

Figure 7.9: Self dynamic structure factor of liquid methanol at the Q values reported in the legend.

Such an exciting scenario convinced us to go further in the study of liquid methanol by looking also at its self dynamics. Thus, the self dynamic structure factor $S_{\text{self}}(Q,\omega)$ was computed from the simulation and the results are displayed in Fig. 7.9 at some example Q values. Similarly to liquid gold in Fig. 7.1, the semilogarithmic scale evidences the presence of shoulders located in the far wings of the spectra. However, Fig. 7.9 differs from Fig. 7.1 because of the presence of (at least) two clearly visible shoulders. As in liquid gold, their frequency position, indicated by arrows in Fig. 7.9, remains substantially unchanged when increasing Q even up to values near Q_{p}, which is around 17 nm^{-1} for this system. It is definitely clear then that these shoulders are significant features of the spectra, approximately positioned at those frequencies where dispersion curves flatten. By looking at Fig. 7.10, we learn that the shoulder around 40 ps^{-1} is related to the high-frequency optic-like modes, while the other one, around 20 ps^{-1}, is due to the longitudinal acoustic modes. Differently from the gold case we did not perform a mode expansion of $S_{\text{self}}(Q,\omega)$.

In the study of liquid gold we noticed an important fact: the shape of $S_{\text{self}}(Q,\omega)$ at large ω

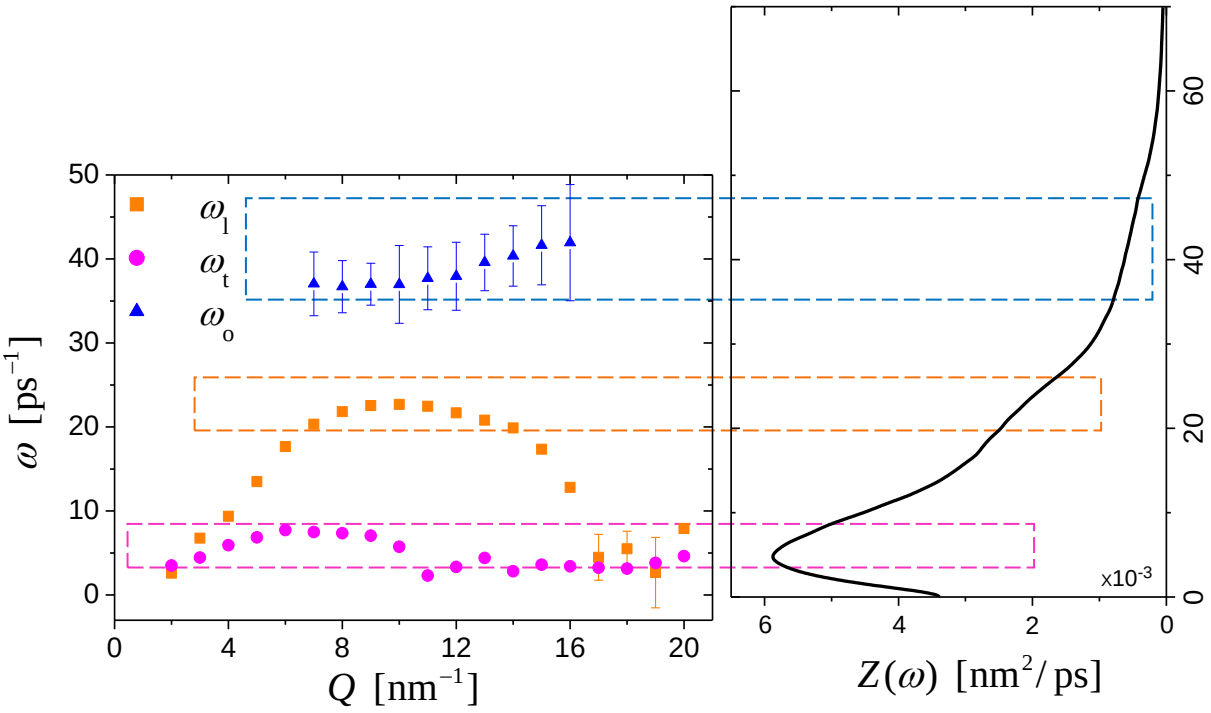

Figure 7.10: Dispersion curve of collective modes of liquid methanol as obtained in Ref. [87], compared with the shape of $Z(\omega)$. The maxima in the dispersion curve occur at frequencies in agreement with the shoulder in the DoS (the dashed rectangles are guides to the eye).

is strictly linked to the spectrum $Z(\omega)$ of the VAF, i.e. the density of states. This is actually the case also for liquid methanol, as it is evident by looking at Fig. 7.10, where the simulated $Z(\omega)$ is compared with the dispersion of collective modes. Figure 7.10 differs from the corresponding Fig. 7.7 of gold not only for the presence of a new excitation at high frequency, but also for the possibility to associate unambiguously the first peak in $Z(\omega)$ to the presence of a low frequency branch in the dispersion curve. The fact that only one type of modes, i.e. the longitudinal acoustic ones, was observed in the $S(Q,\omega)$ of liquid gold strongly suggests the idea that in these liquids hydrogen bonding is mainly responsible for an enhanced visibility of transverse modes also at the level of the $S(Q,\omega)$ spectrum [109], despite its longitudinal nature.

A complete multi-Lorentzian analysis will help to better understand, and to express in quantitative terms, the way all modes build up the $S_{\mathrm{self}}(Q,\omega)$ and $Z(\omega)$ spectra, and to generalize to a more complex liquid, as methanol, the findings about the self dynamics of liquid gold.

Chapter 8

Conclusions

In this thesis we carried out a significant step forward in the comprehension of single particle dynamics thanks to a new method for the interpretation of the autocorrelation functions, and their spectra, that characterize the microscopic dynamics of fluid systems. To perform such a study we exploited molecular-dynamics simulation results of substantially different types of fluids, thus evidencing differences and similarities among them.

In Ch. 4 it was shown that the multi-exponential method of analysis applies perfectly, with only a small number of terms, to the description, up to very large times, of the velocity autocorrelation function (VAF) of a supercritical Lennard-Jones (LJ) fluid. An analysis performed in the time scale set by collisions, together with its density evolution, allowed us to disclose the nature of the mechanisms contributing to diffusion and to the ultimate loss of velocity correlation. The long-discussed concepts of binary (i.e., fast) and non-binary (i.e., slower) processes intervening in the VAF time dependence were thus found to correspond directly to decay channels whose intensities and lifetimes can be measured. Moreover, when these modes possess an oscillatory character, their frequencies are also obtained from the applied analysis in a natural way.

The presence of a very slow process, with a decay time much longer than that of the other modes and measured on the scale of several tens of collision times, shows that our analysis is consistent with the originally proposed interpretation of the long-time tail (LLT), but, at the same time, provides a unified description of all dynamical properties reflected in the time evolution of the single-atom velocity correlation.

The extension of the exponential mode expansion of the VAF to a wider density range allowed to follow in detail the transition between a dilute and a dense LJ fluid at a weakly supercritical temperature, and to study the modifications brought about by a constant-density cooling down to liquid temperatures not far from the triple point. A great step forward with respect to the work illustrated in Ch. 4 is performed in Ch. 5, which consists in the identification of the modes representing the three fundamental dynamical processes typical of a simple monatomic fluid, i.e. the long-time tail, the propagation of longitudinal sound waves, and the transverse dynamics, with its clear transition to the excitation of propagating waves.

This work also confirmed recent results on the existence of a crossover in the supercritical fluid region, evidenced by the density evolution of the VAF time dependence. In particular, the multiexponential analysis allowed us to bring to the foreground the role played by the changing nature of transverse dynamics. Moreover, we stress that we gave in this work a clear demonstration of the fact that the frequency spectrum of the VAF, $Z(\omega)$, can be interpreted as a real density of states (DoS) for the microscopic dynamics of a fluid.

With the aim of applying the multi-exponential method also to a non-classical fluid, we carried out simulations of para-hydrogen in similar supercritical conditions, by means of the ring-polymer molecular dynamics technique. Besides the novelty of VAF calculations of p-H_2 at these thermodynamic states, we performed in Ch. 6 a detailed comparison between the Kubo-transformed VAF of p-H_2 and the VAF of the classical LJ fluid, from which it appears that the former has an overall trend that resembles the latter but at some lower density. We ascribe this fact to the delocalization effect, which ultimately makes a quantum fluid to behave as a less-structured, "softer" system. Moreover, we have clearly evidenced that an LTT is still present in this semi-quantum fluid, although the effectiveness of a $t^{-3/2}$ power-law dependence is questionable at the lower densities.

The analysis of the single-particle dynamics structure factor $S_{\mathrm{self}}(Q,\omega)$ of liquid gold in a wide frequency range (see Ch. 7) has highlighted the close connection between $S_{\mathrm{self}}(Q,\omega)$ and $Z(\omega)$. In particular, we demonstrated that a reliable access to the $Z(\omega)$ of a liquid from $S_{\mathrm{self}}(Q,\omega)$ is possible, at least in its low-frequency part, which is more reliably accessed in an incoherent neutron scattering experiment. The method we propose proves extremely accurate and provides resolution-free results. It is a merit of the multi-Lorentzian expansion to facilitate

the $Q \rightarrow 0$ extrapolation of the data, with a consequently very precise determination of the limit curve $Z(\omega)$ on an absolute scale. In addition, when the directly simulated VAF spectrum is compared to our determination of $Z(\omega)$, the two spectra are found to coincide perfectly. It is also clearly shown in this work how the macroscopic diffusion coefficient related to $Z(\omega = 0)$ originates from the non-hydrodynamic modes in $S_{\text{self}}(Q, \omega)$, and that the Fick's Lorentzian mode does not determine any feature of the DoS of a liquid. A non trivial result is that single-particle diffusion is the macroscopic manifestation of propagating, shear and sound, waves and of confinement effects.

Moreover, the conceptual identification of $Z(\omega)$ with the DoS of a liquid, made in Ch. 5, is reinforced by the analysis of the gold and methanol cases. Indeed, the mode expansion of $Z(\omega)$ brought the important information about the existence of transverse propagating modes in liquid gold and gave an indication of the frequencies characterizing them. This fact is particularly relevant in cases, as the one of liquid gold, where the existence of transverse propagating modes cannot be established by looking at the dynamic structure factor $S(Q, \omega)$, where only the typical longitudinal waves of liquids show up.

Finally, our preliminary study of a molecular HB liquid as methanol has demonstrated that a new spectral feature shows up in the far wings of $S_{\text{self}}(Q, \omega)$ and $Z(\omega)$ spectra, which we relate to the presence of a high-frequency, hydrogen-bond driven, optic-like branch in the dispersion curve. These findings represent a further confirmation of the close relation between single-particle functions and collective properties of liquids.

Bibliography

[1] F. Barocchi, U. Bafile, and M. Sampoli, Phys. Rev. E **85**, 022102 (2012).

[2] F. Barocchi and U. Bafile, Phys. Rev. E **87**, 062133 (2013).

[3] F. Barocchi, E. Guarini, and U. Bafile, Phys. Rev. E **90**, 032106 (2014).

[4] E. Guarini, U. Bafile, F. Barocchi, A. De Francesco, E. Farhi, F. Formisano, A. Laloni, A. Orecchini, A. Polidori, M. Puglini, and F. Sacchetti, Phys. Rev. B **88**, 104201 (2013).

[5] S. Bellissima, M. Neumann, E. Guarini, U. Bafile and F. Barocchi, Phys. Rev. E **92**, 042166 (2015).

[6] S. Bellissima, M. Neumann, E. Guarini, U. Bafile, and F. Barocchi, Phys. Rev. E **95**, 012108 (2017).

[7] E. Guarini, S. Bellissima, U. Bafile, E. Farhi, A. De Francesco, F. Formisano and F. Barocchi, Phys. Rev. E **95**, 012141 (2017).

[8] J. P. Boon and S. Yip, *Molecular Hydrodynamics* (Dover, New York, 1980).

[9] U. Balucani and M. Zoppi, *Dynamics of the Liquid State* (Clarendon, Oxford, 1994).

[10] J. P. Hansen and I. R. McDonald, *Theory of Simple Liquids* (Academic Press, London, 1986).

[11] S. W. Lovesey, *Theory of Neutron Scattering from Condensed Matter* (Clarendon, Oxford, 1984).

[12] N. W. Ashcroft and N. D. Mermin, *Solid State Physics* (Saunders College, Philadelphia, 1976).

[13] K. S. Singwi and A. Sjölander, Phys. Rev. **120**, 1093 (1960).

[14] P. A. Egelstaff and P. Schofield, Nucl. Sci. Eng. **12**, 260 (1962).

[15] B. R. A. Nijober and A. Rahman, Physica **32**, 415 (1966).

[16] H. Mori, Prog. Theor. Phys. **33**, 423 (1965).

[17] R. Zwanzig, in Lectures in Theoretical Physics, edited by W. E. Brittin (Interscience, New York, 1961); Annu. Rev. Phys. Chem. **16**, 67 (1965).

[18] R. Zwanzig, J. Stat. Phys. **13**, 347 (1975).

[19] H. Mori, Prog. Theor. Phys. **34**, 399 (1965).

[20] B. J. Berne, J. P. Boon and S. A. Rice, J. Chem. Phys. **45**, 1086 (1966).

[21] J. R. D. Copley and S. W. Lovesey, Rep. Prog. Phys. **38**, 461 (1975).

[22] K. S. Singwi and M. P. Tosi, Phys. Rev. **157**, 153 (1967).

[23] D. Levesque and L. Verlet, Phys. Rev. A **2**, 2514 (1970).

[24] G. Wahnström and L. Sjögren, J. Phys. C **15**, 401 (1982).

[25] M. H. Lee, Phys. Rev. B **26**, 2547 (1982).

[26] M. H. Lee, Phys. Rev. Lett. **49**, 1072 (1982).

[27] M. H. Lee, Phys. Rev. E **62**, 1769 (2000).

[28] U. Bafile, E. Guarini, and F. Barocchi, Phys. Rev. E **73**, 061203 (2006).

[29] H. C. Andersen, J. Chem. Phys. **72**, 2384 (1980).

[30] S. Nosé and M. L. Klein, Mol. Phys. **50**, 1055 (1983).

[31] H. J. C. Berendsen, J. P. M. Postma, W. F. van Gunsteren, A. DiNola and J. R. Haak, J. Chem. Phys. **81**, 3684 (1984).

[32] S. Nosé, J. Chem. Phys. **81**, 511 (1984).

[33] D. J. Evans and G. P. Morriss, Comput. Phys. Rep. I, 299 (1984).

[34] W. G. Hoover, Phys. Rev. A **31**, 1695 (1985).

[35] M. E. Tuckerman, *Statistical Mechanics: Theory and Molecular Simulation* (Oxford University Press, 2010).

[36] M. P. Allen and D. J. Tildesley, *Computer Simulation of Liquids* (Oxford University Press, 1987).

[37] T. Gaskell and S. Miller, J. Phys. C: Solid State Phys. **11**, 3749 (1978).

[38] T. Gaskell and S. Miller, J. Phys. C: Solid State Phys. **11**, 4839 (1978).

[39] B. Alder and T. R. Wainwright, Phys. Rev. Lett. **18**, 988 (1967).

[40] B. Alder and T. R. Wainwright, Phys. Rev. A **1**, 18 (1970).

[41] K. Kawasaki, Phys. Lett. **32A**, 379 (1970).

[42] M. H. Ernst, E. H. Hauge, and J. M. J. van Leeuwen, Phys. Rev. Lett. **25**, 1254 (1970).

[43] M. H. Ernst, E. H. Hauge and J. M. J. van Leeuwen, Phys. Rev. A **4**, 2055 (1971).

[44] J. R. Dorfman and E. G. D. Cohen, Phys. Rev. A **6**, 776 (1972).

[45] D. Levesque and W. T. Ashurst, Phys. Rev. Lett. 33, 277 (1974).

[46] A. McDonough, S. P. Russo, and I. K. Snook, Phys. Rev. E **63**, 026109 (2001).

[47] R. F. A. Dib, F. Ould-Kaddour, and D. Levesque, Phys. Rev. E **74**, 011202 (2006).

[48] K. Meier, A. Laesecke, and S. Kabelac, J. Chem. Phys. **121**, 3671 (2004).

[49] K. Meier, A. Laesecke, and S. Kabelac, J. Chem. Phys. **121**, 9526 (2004).

[50] S. R.Williams, G. Bryant, I. K. Snook, and W. van Megen, Phys. Rev. Lett. **96**, 087801 (2006).

[51] M. Isobe, Phys. Rev. E **77**, 021201 (2008).

[52] R. E. Ryltsev and N. M. Chtchelkatchev, J. Chem. Phys. **141**, 124509 (2014).

[53] J. J. Erpenbeck and W. W. Wood, Phys. Rev. A **26**, 1648 (1982).

[54] J. K. Johnson, J. A. Zollweg, and K. E. Gubbins, Mol. Phys. **78**, 591 (1993).

[55] K. Meier, PhD thesis, University of the Federal Armed Forces Hamburg, 2002.

[56] We thank Daniele Colognesi (ISC-CNR) for doing the Monte Carlo computations.

[57] F. A. Gorelli, M. Santoro, T. Scopigno, M. Krisch and G. Ruocco, Phys. Rev. Lett. **97**, 245702 (2006).

[58] G. G. Simeoni, T. Bryk, F. A. Gorelli, M. Krisch, G. Ruocco, M. Santoro and T. Scopigno, Nat. Phys. **6**, 503 (2010).

[59] V. V. Brazhkin, Yu. D. Fomin, A. G. Lyapin, V. N. Ryzhov and K. Trachenko, Phys. Rev. E **85**, 031203 (2012).

[60] V. V. Brazhkin, Yu. D. Fomin, A. G. Lyapin, V. N. Ryzhov, E. N. Tsiok and K. Trachenko, Phys. Rev. Lett. **111**, 145901 (2013).

[61] V. V. Brazhkin and K. Trachenko, J. Phys. Chem. B **118**, 11417 (2014), and Refs. therein.

[62] A. Cunsolo, Appl. Sci. **6**, 64 (2016).

[63] H. R. Glyde, J. Low Temp. Phys. **59**, 561 (1985).

[64] A. Rahman, M. J. Mandell and J. P. McTague, J. Chem. Phys. **64**, 1564 (1976).

[65] K. Toukan, M. A. Ricci, S.-H. Chen, C.-K. Loong, D. L. Price, and J. Teixeira, Phys. Rev. A **37**, 2580 (1988).

[66] C. Morkel and C. Gronemeyer, Z. Phys. B - Condensed Matter **72**, 433 (1988).

[67] G. Garberoglio and R. Vallauri, J. Chem Phys. **115**, 395 (2001).

[68] J. Cao and G. A. Voth, J. Chem. Phys. **103**, 4211 (1995).

[69] M. Zanatta, F. Sacchetti, E. Guarini, A. Orecchini, A. Paciaroni, L. Sani and C. Petrillo, Phys. Rev. Lett. **114**, 187801 (2015).

[70] M. Sampoli, G. Ruocco and F. Sette, Phys. Rev. Lett. **79**, 1678 (1997).

[71] A. Cunsolo, C. N. Kodituwakku, F. Bencivenga, M. Frontzek, B. M. Leu and A. H. Said, Phys. Rev. B **85**, 174305 (2012).

[72] Yu. D. Fomin, V. N. Ryzhov, E. N. Tsiok, V. V. Brazhkin and K. Trachenko, J. Phys.: Condens. Matter **28** 43LT01 (2016).

[73] J. Frenkel, *Kinetic Theory of Liquids* (Oxford University Press, London, 1947).

[74] R. P. Feynman and A. R. Hibbs, *Quantum mechanics and path integrals* (McGraw-Hill, New York, 1965).

[75] D. Chandler and P. G. Wolynes, J. Chem. Phys. **74**, 4078 (1981).

[76] N. Metropolis, A. W. Rosenbluth, M. N. Rosenbluth, A. H. Teller and E. Teller, J. Chem. Phys. **21**, 1087 (1953).

[77] J. Cao and G. A. Voth, J. Chem. Phys. **100**, 5106 (1994).

[78] S. Jang and G. A. Voth, J. Chem. Phys. **111**, 2371 (1999).

[79] I. R. Craig and D. E. Manolopoulos, J. Chem. Phys. **121**, 3368 (2004).

[80] B. J. Braams and D. E. Manolopoulos, J. Chem. Phys. **125**, 124105 (2006).

[81] J. A. Poulsen, G. Nyman and P. J. Rossky, Proc. Natl. Acad. Sci. U.S.A. **102**, 6709 (2005).

[82] R. Kubo, J. Phys. Soc. Jpn. **12**, 570 (1957).

[83] T. F. Miller and D. E. Manolopoulos, J. Chem. Phys. **122**, 184503 (2005).

[84] B. A. Younglove, J. Phys. Chem. Ref. Data **11**, Suppl. 1 (1982).

[85] I. F. Silvera and V. V. Goldman, J. Chem. Phys. **69**, 4209 (1978).

[86] P. J. Linstrom and W. G. Mallard, *NIST Chemistry WebBook, NIST Standard Reference Database* No. 69, (NIST, Gaithersburg) 2005.

[87] S. Bellissima, S. De Panfilis, U. Bafile, A. Cunsolo, M. A. González, E. Guarini, and F. Formisano, Sci. Rep. **6**, 39533 (2016).

[88] S. Hosokawa, M. Inui, Y. Kajihara, K. Matsuda, T. Ichitsubo, W.-C. Pilgrim, H. Sinn, L. E. González, D. J. González, S. Tsutsui, and A. Q. R. Baron, Phys. Rev. Lett. **102**, 105502 (2009).

[89] V. M. Giordano and G. Monaco, Proc. Natl. Acad. Sci. U.S.A. **107**, 21985 (2010).

[90] V. M. Giordano and G. Monaco, Phys. Rev. B **84**, 052201 (2011).

[91] S. Hosokawa, S. Munejiri, M. Inui, Y. Kajihara, W.-C. Pilgrim, Y. Ohmasa, S. Tsutsui, A. Q. R. Baron, F. Shimojo, and K. Hoshino, J. Phys.: Condens. Matter **25**, 112101 (2013).

[92] S. Hosokawa, M. Inui, Y. Kajihara, S. Tsutsui, and A. Q. R. Baron, J. Phys.: Condens. Matter **27**, 194104 (2015).

[93] B. G. del Rio, D. J. González and L. E. González, Phys. Fluids **28**, 107105 (2016).

[94] M. Marqués, D. J. González and L. E. González, Phys. Rev. B **94**, 024204 (2016).

[95] M. Marqués, L. E. González and D. J. González, Phys. Rev. B **92**, 134203 (2015).

[96] A. De Francesco, E. Guarini, U. Bafile, F. Formisano, and L. Scaccia, Phys. Rev. E **94**, 023305 (2016).

[97] Chr. Morkel, Chr. Gronemeyer, W. Gläser, and J. Bosse, Phys. Rev. Lett. **58**, 1873 (1987).

[98] P. Verkerk, J. Westerweel, U. Bafile, L. A. de Graaf, W. Montfrooij, and I. M. de Schepper, Phys. Rev. A **40**, 2860 (1989).

[99] W. Montfrooij and I. de Schepper, Phys. Rev. A, **39**, 2731 (1989).

[100] P. A. Egelstaff, *An Introduction to the Liquid State*(Academic, New York, 1967).

[101] P. Protopapas, H. C. Andersen and N. A. D. Parlee, J. Chem. Phys. **59**, 15 (1973).

[102] R. N. Joarder and R. V. Gopala Rao, Phys. Status Solidi (b) **109**, 137 (1982).

[103] A. Bogicevic, L. B. Hansen, and B. I. Lundqvist, Phys. Rev. E **55**, 5535 (1997).

[104] S. Ryu, C. R. Weinberger, M. I. Baskes, and W. Cai, Modelling Simul. Mater. Sci. Eng. **17**, 075008 (2009).

[105] E. Guarini, U. Bafile, F. Barocchi, F. Demmel, F. Formisano, M. Sampoli, and G. Venturi, Europhys. Lett. **72**, 969 (2005).

[106] M. Sampoli, U. Bafile, F. Barocchi, E. Guarini, and G. Venturi, Journal of Physics: Condensed Matter **20**, 104206 (2008).

[107] M. Sampoli, U. Bafile, E. Guarini, and F. Barocchi, Phys. Rev. B **79**, 214203 (2009).

[108] U. Bafile, E. Guarini, M. Sampoli, and F. Barocchi, Phys. Rev. E **80**, 040201 (2009).

[109] A. Cunsolo, Adv. Cond. Matter Phys. **2015**, 137435 (2015), and Refs. therein.

Acknowledgements

First of all, I would like to address a specific acknowledgement to each member of the group in which I've carried out my PhD research. To this aim, I start to express my sincere gratitude to my Tutor Dr. Eleonora Guarini for her passionate support to this study. Her guidance and teaching helped me during all the time of research and writing of this thesis. My gratitude also goes to Dr. Ubaldo Bafile for his constant and enthusiastic participation to all aspects of my PhD work, and for having provided a crucial contribution to its success. My sincere thanks also goes to Prof. Fabrizio Barocchi, whose previous studies made my entire research possible. His long-standing experience has made him a reference point for the progress of the project. Last but not the least, I would like to thank Prof. Martin Neumann, not only for his essential role in providing us simulation data for the work, but mainly for the time he spent in Florence with the purpose of teaching me the fundamentals of liquid simulation techniques.

Moreover, I wish to thank Alessandro Torcini for giving me the opportunity of using his computer cluster to perform my simulations, and Dr. Daniele Colognesi for some extremely clarifying general discussions.